UNIVERSITY OF CALIFORNIA
SANTA CRUZ

PROPERTIES OF DARK MATTER HALOS: ENVIRONMENT DENSITY AND MASS LOSS

A dissertation submitted in partial satisfaction of the
requirements for the degree of

DOCTOR OF PHILOSOPHY

in

PHYSICS

by

Christoph Tenzin Lee

March 2019

The Dissertation of Christoph Tenzin Lee
is approved:

Professor Stefano Profumo, Chair

Professor Joel Primack

Professor Tesla Jeltema

Lori Kletzer
Vice Provost and Dean of Graduate Studies

Table of Contents

List of Figures

List of Tables

Abstract

Properties of Dark Matter Halos:

Environment Density and Mass Loss

by

Christoph Tenzin Lee

We use results from the Bolshoi-Planck cosmological dark matter simulation to (1) study the evolution of dark matter halo properties in regions of different local environment densities, (2) investigate whether dark matter halo spin is a reliable predictor of galaxy size, and (3) determine the causes and consequences of virial mass loss in distinct halos. We find that halos in high density regions typically have higher NFW concentrations ($C = R_{\rm vir}/R_{\rm s}$), lower spin parameters, and much lower mass accretion rates than median halos at z = 0. These trends are a result of strong tidal forces (due to nearby massive halos), which inhibit relatively lower mass halos from accreting material and strip particles from their outer regions. Surprisingly, we find that lower mass halos in the lowest density regions also have higher concentrations and lower spin parameters. We provide possible explanations for these trends: (i) halos in low density regions must form early if they are to form at all, and (ii) less violent accretion histories lead to less increase in $R_{\rm s}$, implying higher concentrations; (iii) these halos have fewer massive neighbors to spin them up, implying lower spin parameters. If halo spin parameter is proportional to galaxy size, this predicts that galaxies in low density regions should have less extended disks. We test this prediction using SDSS data. We additionally identify two primary causes of halo mass loss: tidal stripping by a massive neighboring halo (a dominating effect in high density regions), and virial relaxation after a major merger. Tidal stripping causes halos to become less prolate and have lower

spins and higher NFW concentrations. Tidally stripped halos often lose a large fraction of their peak mass ($> 20\%$) and most never recover (or even reattain a positive accretion rate). Major mergers initially boost Mvir and typically cause the final halo to become more prolate and less relaxed and to have higher spin and lower NFW concentration. As the halo relaxes, high energy material from the recent merger gradually escapes beyond the virial radius, temporarily resulting in a net negative accretion rate that reduces the halo mass by $5 - 15\%$ on average. Halos that experience a major merger around z=0.4 typically reach a minimum mass near z=0.

Acknowledgments

I am grateful to many people that have contributed to my graduate experience. First and foremost, my advisor, Joel Primack, has been endlessly encouraging and supportive. Joel's depth of knowledge is immense and he often recalls details of figures I made years prior more accurately than I do myself. He is always available and eager to meet and discuss research progress, and invests significant time and resources into the success of his students. I thank my committee members, Stefano Profumo and Tesla Jeltema, for providing valuable feedback during my oral qualifying exam and dissertation defense, and for bearing with me as I finalized this thesis. I also thank administrators Ben Miller, Vicki Johnson, and David Sugg for their tireless assistance.

I've had the privilege to collaborate with many fantastic researchers, both at UCSC and around the world. The work presented in this thesis was heavily influenced and supported by Peter Behroozi, Aldo Rodríguez-Puebla, Doug Hellinger, Avishai Dekel, Sandy Faber, and David Koo. For their significant contributions of time and expertise in advising work that is not covered in this thesis, but which has defined the final stage of my graduate work, I thank Marc Huertas-Company and Yicheng Guo. I also thank David Reiman, Fangzhou Jiang, Rachel Somerville, Miguel Aragon-Calvo, Brant Robertson, undergraduate students Elliot Eckholm, Tze Goh, Graham Vanbenthuysen, and Summer Internship Program (SIP) students Jessica Zhu, Austin Tuan, Peter Wu, and Shawn Zhang for their insights and contributions.

Finally, I would not have enjoyed my time in Santa Cruz so thoroughly if not for some awesome friends and family. Fellow doctors-to-be and housemates Joey Schindler, Cameron MacKeen, Webster Rasmussen, Mike Testa, and George the slug defined the Northrop era. My parents, Tony and Jill, and brother Taylor,

have been a constant source of support and vitality. Special shoutout to Cameron and Taylor for surviving the Ionian Basin (and all the rest).

The text of this thesis includes modified reprints of the following previously published material with permission from Oxford University Press: "Properties of Dark Matter Halos as a Function of Local Environment Density," Lee C. T., Primack J. R., Behroozi P., Rodríguez-Puebla A., Hellinger D., Dekel A., 2017, MNRAS, 466, 3834, and "Tidal Stripping and Post-Merger Relaxation of Dark Matter Halos: Causes and Consequences of Mass Loss," Lee C. T., Primack J. R., Behroozi P., Rodríguez-Puebla A., Hellinger D., Dekel A., 2018, MNRAS, 481, 4038. These papers were advised primarily by Joel Primack, with important input from the co-authors. The writing and analysis of these papers were largely a result of my own effort. Peter Behroozi, Aldo Rodrìguez-Puebla, Doug Hellinger, and Avishai Dekel give permission for these papers to be reprinted in this thesis.

Chapter 1

Introduction

This thesis is composed of two main sections, each addressing a fundamental question about dark matter halos. In Chapter 2, I present a detailed investigation of the relationship between dark matter halo properties and local environment density: how are dark matter halos (and by extension, the galaxies that they host) influenced by their local environment? In high density regions, I found that a very high fraction of halos are in a state of negative accretion; that is, they are actively losing mass over time. This prompted a subsequent exploration into the mechanisms that promote negative dark matter mass accretion rates in distinct dark matter halos. Why do some dark matter halos lose mass? What effect does mass loss have on the dark matter density profile, shape, angular momentum distribution, and other properties of the halo? Chapter 3 answers these questions. In addition to the two main analyses detailed in Chapters 2 and 3, I've led or participated in a number of additional research projects that are not discussed in detail in this thesis. In the paragraphs that follow, I provide summaries of several of these peripheral analyses.

In Chapter 2, I determine dark matter density by counting the number of dark matter particles in small cells in the Bolshoi-Planck cosmological dark mat-

ter simulation, and then smoothing these raw particle counts using a Gaussian kernel. Performing this smoothing procedure several times using kernels with different smoothing radii provides a precise local density estimation for all halos in the simulation volume. It is useful to evaluate dark matter density on different scales, both because halo size varies dramatically as a function of halo mass, and because hierarchical structures that compose the cosmic web (e.g. voids, walls, and filaments) are washed out when sampled at large length scales. The subsequent sections compare how halos in low density regions differ from halos in high density regions as a function of halo mass and density smoothing scale. One important finding from this work is that halos in low density regions have lower spin parameters than halos in higher density regions. Furthermore, halos in low density regions at the present day ($z = 0$) evolved from halos that formed in low density regions, and which also had consistently lower spin parameters than halos in higher density regions. This could result due to a relative lack of tidal torque from neighboring halos during halo formation in low density regions. This also raises the question: is there a connection between halo spin parameter and galaxy properties? And if so, are galaxies in low density regions different from those in higher density regions as a result?

I have worked closely with UCSC undergraduate student Graham Vanbenthuysen to recast the results from Ch. 2 in an observational context. Using abundance matching, we have filled halos in the Bolshoi-Planck simulation with galaxies from the Sloan Digital Sky Survey (SDSS), and then computed local dark matter densities using several new methods that are standard in observational astronomy. This includes density estimation based on the N-th nearest neighbor statistic (computing density from the volume enclosing the N nearest galaxies), as well as counting the number of galaxies within fixed apertures of different sizes

(using the same radii as the smoothing kernels used in Ch. 2. Comparison of the density dependence of the same halo properties (e.g. NFW concentration, spin parameter, specific mass accretion rate) for these different density estimation methods shows qualitative agreement, indicating that the relationships between halo properties and local density discussed in Ch. 2 are not strongly dependent on the specific method of density estimation employed. Furthermore, we see that galaxies tend not to decrease in size in very low density regions, suggesting that galaxy size is not closely controlled by halo spin parameter (as was proposed by, e.g. Somerville et al. (2018)). These findings may be more consistent with the halo concentration-based galaxy size estimator proposed in Jiang et al. (2018), since this quantity is more stable between halos in median and low density regions.

While Ch. 2 studies in detail how the density of the local environment relates to halo properties, it does not address the how different cosmic web structure types impact halo properties. In Goh et al. (2019), we approach this subject. In order to evaluate the affect of cosmic web structure type alone, we need to control for the strong local density dependence, otherwise halos in voids would be biased towards much lower densities than halos in filaments. Fortunately, the distributions of local densities in voids, walls, and filaments overlap enough that we can select a population of halos from each structure type with the same local density. Do halos in voids, walls, and filaments have different distributions of properties when selected from a fixed range of local density? We see no statistically significant variation in the distributions of halo properties as a function of cosmic web type for any of the properties we evaluated, which were NFW concentration, spin parameter, specific mass accretion rate, halo shape, scale factor of the last major merger, and scale factor when halos reach half their maximum mass. This doesn't mean that halo properties are fully disconnected from the nature of the

structure in which they reside. Indeed, Aragon-Calvo (2016) finds a correlation between the orientation of the halo angular momentum axis and the orientation of the halo shape with local cosmic web features. However, our work in Goh et al. (2019) does establish that local density is a stronger predictor of many halo properties than cosmic web structure type alone.

Several additional analyses have also added value to our understanding of the processes surrounding halo mass loss and their affects on halo properties. In Tuan & Zhu (2015) and Tuan (2016), we studied the dark matter density profiles of halos, especially those residing in high density regions and which have been stripped by a massive neighboring halo. The NFW fitting function, used by default in many halo finders, does not accurately describe the density profiles of halos that have been stripped of mass. Rather, we found that using a modified, 3-parameter NFW fit where the $(1 + r/r_s)^2$ term in the denominator is replaced by $(1 + r/r_s)^n$ does a much better job at minimizing the fitting error in these halos, albeit at the cost of an additional fitting parameter. In fact, when we allow for this additional degree of freedom in fitting halo density profiles, we find that halos that have been tidally stripped have a goodness-of-fit comparable on average to those that have not been tidally stripped. Interestingly, the class of halos with the poorest goodness-of-fit using the modified NFW profile are those in the lowest density regions, suggesting some kind of systematic difference in how the dark matter is distributed in these halos compared to those in higher density regions. Presumably, this difference may arise from the inner regions of the halos ($r < r_s$), because halos in low density regions tend to be fit with with outer profile slopes similar to the standard NFW profile ($\rho \propto r^{-3}$). As mentioned, halos in high density regions are much better fit by this 3-parameter NFW formula, because the fitting function is able to accommodate the steeper outer profiles resulting from

tidal stripping. We see that on average low mass halos in high density regions increase from an outer profile radial dependence of roughly $\rho \propto r^{-3}$ in median density regions to nearly $\rho \propto r^{-3.5}$ in high density regions, with a much higher dispersion in high density regions.

In 3, we suggest that halos that have lost mass, but which have not had a recent major merger and have not recently experienced strong tidal forces, probably did so as a result of a minor merger. In Wu & Zhang (2017), we test this hypothesis by developing a method to flag possible minor mergers using the evolution of halo mass and maximum circular velocity ($V_{\rm max}$) for individual halos. We find that halos that have lost greater than 5% of their peak mass, but have not had a recent major merger or experienced recent tidal stripping, did have a recent minor merger. The distribution of last minor merger scale factors in this group is strikingly similar to that of last major merger scale factors for halos that lost mass due to major mergers. In both cases, the distribution of last merger scale factors peaks at approximately $a = 0.7$ ($z = 0.4$), and falls off steeply on either side. This is a reflection of the time delay between the incidence of the merger and the subsequent relaxation phase during which material is shed from the halo (see also Figs. A.17 and A.18).

We further compared in Wu & Zhang (2017) the impact of minor mergers and major mergers on halo properties by characterising the resulting variations in halo shape (prolateness), spin parameter, NFW scale radius, asymmetry ($X_{\rm off}$), and virial ratio. We found that both spin parameter and the virial ratio typically reach a peak shortly after the incoming halo crosses the virial radius of the main halo and then gradually subside as the halo relaxes. In contrast, the scale radius, prolateness, and asymmetry measurement all reach a peak almost immediately after the virial radius crossing, and in a majority of cases peak again after a brief

oscillation. We rarely observe a third peak in any halo property following a single merging event. These dramatic oscillations in scale radius, prolateness, and $X_{\rm off}$ manifest in response to the blacksplash of the merging halo core after it punches through the main halo. These behaviors are consistent both for major merger and minor merger induced mass loss scenarios.

The text of this thesis contains modified reprints of material from two published papers. Chapter 2 and Figs. A.1 - A.8 are taken from Lee et al. (2017). Chapter 3 uses material from Lee et al. (2018).

Chapter 2

Environment Density

2.1 Background

In the ΛCDM standard modern theory of structure formation in the universe, galaxies populate dark matter halos and subhalos. The properties of these halos and their distributions in space are therefore important in understanding the properties and distribution of galaxies. The present paper investigates how the properties of the dark matter halos correlate with their environments, in particular with the mass density on various scales around the halos. We also try to understand the origins of these correlations, studying in particular how halo environments affect halo evolution.

The effects on dark matter halos of their environments have been studied in many earlier papers. Since the earliest cold dark matter paper Blumenthal et al. (1984), it has been assumed that the initial conditions were Gaussian, as predicted by the simplest cosmic inflation models, which permitted treatment of halo properties based on analysis of the linearly evolved initial conditions. The early N-body simulations (e.g., Davis et al., 1985) had resolution too low to permit identifying dark matter halos so that galaxies had to be identified with individual

particles in the simulations, which led to some misleading conclusions such as the supposed need for high bias. But improved analysis of the initial conditions, for example by the "peaks" approach (Kaiser, 1984; Peacock & Heavens, 1985; Bardeen et al., 1986), permitted more detailed treatments of dark matter halo clustering (e.g., Dalal et al., 2008; Desjacques & Sheth, 2010). Combination of the peaks approach plus N-body simulations led to further insights, including that halos in dense regions that do not correspond to high peaks in the initial conditions accrete more slowly than halos that do correspond to high peaks (Ludlow & Porciani, 2011).

Faster supercomputers and better codes have led to improved N-body simulations, in which the halos and subhalos that host galaxies, groups, and clusters are resolved. Such simulations have permitted more detailed analyses of the correlations of halo properties with each other and with the halo environments measured in various ways. One of the first papers to do this was Lemson & Kauffmann (1999), which used $\Omega_0 = 1$ τCDM and $\Omega_0 = 0.3$ ΛCDM simulations and concluded that only the halo mass distribution varies as a function of environment, with more high mass halos in denser environments, in reasonable agreement with the analytic calculation by Mo & White (1996) based on extended Press-Schechter theory and the spherical top-hat model. While subsequent N-body calculations confirmed this density effect on the halo mass function, they implied that environmental density also affects halo major merging rates (Gottlöber, Klypin & Kravtsov, 2001) and other halo properties. Bullock et al. (2001) found that halos in dense environments tend to have higher concentrations than isolated halos. Sheth & Tormen (2004), using the same simulations as Lemson & Kauffmann (1999), found evidence that low-mass halos form somewhat earlier in dense environments. Avila-Reese et al. (1999) found that dark matter halos that are isolated or in intermediate density

environments have outer density profiles $r^{-\beta}$ with $\beta \approx 2.8 \pm 0.5$ while halos in denser regions have a wider range of β up to ~ 5. Avila-Reese et al. (2005), again using ΛCDM simulations that were very small by modern standards, nevertheless found that halos in dense regions had lower spin parameters and higher concentrations and were less prolate than halos in lower density environments, with the differences arising mostly at low redshifts $z < 1$ from phenomena such as tidal stripping in dense environments. In the present paper, we confirm and expand on these results. Maulbetsch et al. (2007) used a 512^3 particle ΛCDM simulation in a $(50h^{-1}\mathrm{Mpc})^3$ volume to study the mass accretion history of galaxy-mass halos in different environments, and found that halos of the same final mass accreted their mass earlier in denser environments, and also accreted a significantly higher fraction of their mass in major mergers. They suggested that this could help to explain the galaxy density-morphology relation, that early type galaxies are more common in dense environments. They also found that $\sim 80\%$ of halos in higher density environments are not accreting (i.e., have $\dot{M} \leq 0$), while this fraction is only $\sim 20\%$ in low density environments. They defined the environmental density on a scale of $4h^{-1}$Mpc, with density less than average considered "low" and density greater than 6 times background density considered "high," but they found similar results measuring density on scales from 2 to $8h^{-1}$Mpc. They also found that subtracting the central halo mass in determining the environmental density, as Lemson & Kauffmann (1999) had done, made little difference to the results. In the present paper we do not subtract the central halo mass in determining the environmental density, since we consider densities in volumes much larger than those of their central halos (i.e. for a given halo mass, we only consider environment densities smoothed on scales greater than 4 R_{vir}; see §5.1 for further explanation; cf. Muldrew et al., 2012).

Measuring environmental density in spheres of radii 1, 2, 4, and $8h^{-1}$Mpc in a set of relatively small ΛCDM simulations in various volumes, Macciò et al. (2007) found that higher-concentration low-mass halos are found in denser environments, and lower-concentration ones in less dense environments. This is consistent with the higher concentration of early-forming halos (Bullock et al., 2001; Wechsler et al., 2002a); the earlier formation of low-mass halos in dense regions (e.g., Sheth & Tormen, 2004); and the finding that high-concentration low-mass halos are more correlated than average (i.e., more biased: Gao, Springel & White, 2005; Wechsler et al., 2006; Gao & White, 2007), a phenomenon that has become known as "assembly bias." Here, low-mass halos means those less massive than the characteristic mass $M_{\rm C}$ of halos collapsing at the present epoch (see, e.g., Rodriguez-Puebla et al., 2016, Fig. 9).

Faltenbacher & White (2010), analysing the Millennium simulation (Springel et al., 2005), found that near-spherical and high-spin halos show enhanced clustering. Fakhouri & Ma (2010), also analysing the Millennium simulation, showed that mergers are increasingly important for halo mass growth in denser regions while diffuse accretion dominates growth in voids (elaborating on the results of Maulbetsch et al., 2007), with galaxy-mass halos forming somewhat earlier in denser environments, where they accrete less at low redshifts because the dark matter there has higher velocity dispersion (as also argued by Wang, Mo & Jing, 2007; Dalal et al., 2008).

Wang et al. (2011a) studied properties of dark matter halos as a function of their environments, characterized mainly by the tidal field but also by density on a scale of $6h^{-1}$Mpc. They found that high-density environments provide more material for halos to accrete, but the stronger tidal fields there tend to suppress accretion. They found that halos in higher tidal field environments and in higher

density environments have higher spins, with the trends stronger for higher mass halos.

Skibba & Macciò (2011) and Jeeson-Daniel et al. (2011) used principal component analyses to study the correlations of many halo properties including environment. Skibba & Macciò (2011) used the overdensity in spheres of 2, 4 and $8h^{-1}$Mpc to measure the environmental density, and found that at fixed halo mass the environmental density does not significantly determine any of a halo's properties. Jeeson-Daniel et al. (2011) did a more detailed correlation study of halo properties. The strongest correlation they found was between halo concentration and age, with more concentrated halos also being more spherical and having lower spin. But they found that there was little correlation of halo properties with their environment measure. Instead of using overdensity, they measured the environment using a quantity they call $D_{1,0.1}$, equal to the distance to the nearest friends-of-friends halo with a mass greater than 10% of the halo's mass divided by the radius of the neighbour's halo. Unlike overdensity, $D_{1,0.1}$ does not correlate with halo mass (Haas, Schaye & Jeeson-Daniel, 2012).

Some authors (e.g., Bett et al., 2007; Macciò et al., 2007; Skibba & Macciò, 2011; Ludlow et al., 2012a, 2013) have studied mainly dark matter halos that are "relaxed" according to various criteria, such as an upper limit on $D_{\rm off} = |\mathbf{r}_{\rm Peak} - \mathbf{r}_{\rm CM}|/r_{\rm vir}$, the offset of the halo density peak from the center of mass within the halo radius, in units of the halo radius, or on the virial ratio $T/|U|$. In this paper we study all halos, not just "relaxed" ones, because all the halos of mass $\gtrsim 10^{10}{\rm M}_\odot$ will host at least one central galaxy, regardless of whether it is relaxed or not, and our main motivation for studying halo properties as a function of environment is to clarify the implications for galaxies in environments of various densities. In this paper we also restrict attention to discrete halos (i.e.,

those that are not subhalos) since we are interested in using the dark matter halos to understand the properties of their central galaxies.

In the present paper we use the new ΛCDM Bolshoi-Planck simulation (Klypin et al., 2016a; Rodriguez-Puebla et al., 2016) to study the environmental dependence of halo properties and their evolution. The simulation is summarized in §2, and we explain there how we measure the environmental density around every halo. §3 describes how the environmental density depends on the scale on which it is measured, and provides fitting functions using Extreme Value Distributions. §4 describes the environmental dependence of dark matter halo mass functions. In §5.1 we describe correlations between halo properties and environment at the present epoch. In §5.2 we study the redshift evolution of halo properties at different densities, showing the origin at higher redshifts of the trends we found at $z = 0$. In the remaining subsections of §5 we discuss the mass accretion rate (§5.3), halo concentration (§5.4), halo spin (§5.5), and halo prolateness (§5.6). §6 summarizes and discusses our results. The Appendix contains figures that expand upon issues discussed in the text or present alternative plots.

We have found that a large fraction of lower mass halos in dense environments are stripped, that is they have less mass today than their main progenitors did at some earlier epoch. We have found that halo stripping is the main cause of the decrease in spin and the increase in concentration of lower-mass halos in dense regions. We discuss such effects of halo stripping briefly in the present paper, with more detailed results and discussion of the causes of halo stripping in a companion paper (Lee et al. 2016, in preparation).

2.2 Simulations and Method

In this paper we use the ROCKSTAR halo finder (Behroozi, Wechsler & Wu, 2013) and CONSISTENT TREES (Behroozi et al., 2013a) to analyse results for the recent Bolshoi-Planck ΛCDM simulation, with $(2048)^3$ particles in a volume of $(250\ h^{-1}\mathrm{Mpc})^3$, based on the 2013 Planck (Planck Collaboration et al., 2014a) cosmological parameters $\Omega_M = 0.307$, $\Omega_B = 0.048$, $\sigma_8 = 0.823$, and $n_s = 0.96$ and compatible with the Planck 2015 parameters (Planck Collaboration et al., 2015). With a mass per particle of $1.5 \times 10^8\ h^{-1}M_\odot$ and a force resolution of 1 kpc, the Bolshoi-Planck simulation has adequate resolution to identify halos that can host most visible galaxies. This simulation, along with the larger MultiDark-Planck simulations, have been analysed in detail with fitting functions provided for many halo properties (see especially Rodriguez-Puebla et al., 2016) and all of the halo catalogues and merger trees are publicly available.[1]

We implement a Gaussian smoothing procedure to compute the density of the full simulation volume smoothed on many different length scales. We convolve the CIC density cube with a 1-dimensional Gaussian kernel applied sequentially along each axis (x, y, z). We refer to the half-width at half-maximum (HWHM) of the Gaussian kernel as the smoothing radius (σ_s), or smoothing scale. The kernel (k) is truncated at cell t, where $k[t] < k[0]/10^5$, and then renormalized. Since we use a voxel size of 250 $[h^{-1}\mathrm{Mpc}]/1024 \approx 1/4\ h^{-1}\mathrm{Mpc}$, we've chosen to smooth the box on scales of 1/2, 1, 2, 4, 8, and 16 h^{-1}Mpc. We then update each halo in the ROCKSTAR halo catalogues with the CIC and smoothed density values corresponding to their locations in the simulation volume. We prefer using this method to other methods of determining local density (e.g. growing spheres of different

[1] ROCKSTAR catalogues (including local densities around halos) and CONSISTENT TREES merger trees used here are available at `http://hipacc.ucsc.edu/Bolshoi/MergerTrees.html`, and FOF and BDM catalogues are available at `https://www.cosmosim.org/cms/simulations/multidark-project/`.

sizes around halo positions) primarily because it is highly efficient and provides the density field at each point in the simulation volume. In Fig. 2.1 we show the density smoothed on different scales for an example region of the simulation, with a depth of 1/4 h^{-1}Mpc (1 voxel) and a height and width of 62.5 h^{-1}Mpc. Average density regions are distinguished by light blue-green colouring, indicating the transition between underdense (green to black) and overdense (dark blue to yellow) regions.

2.3 Density Distributions

In Fig. 2.2, we present probability distributions of densities smoothed on several length scales for the Boshoi-Planck simulation at redshift $z = 0$. We compute these distributions using the full simulation volume, with black lines indicating different smoothing scales, and coloured lines representing best-fitting analytic functions for each smoothing scale. We report densities with respect to the average density of the simulation to clearly distinguish between underdense and overdense regions. The smallest scales probe the widest range of densities, from the centres of voids to the centres of massive halos. Extreme values in the density field are redistributed over a larger volume when smoothed on larger scales, reflected in the narrower total range of densities observed for larger smoothing scales. The shapes of the distributions indicate the abundance of non-linear structures present at a given length scale. Densities smoothed on scales $\sigma \geq 8$ h^{-1}Mpc have a nearly log-normal distribution peaked around average density. This indicates that density fluctuations on these scales are dominated by large waves in the Gaussian random field, with weak contributions from non-linear structures (voids, etc.) with radii greater than 8 h^{-1}Mpc. On smaller scales ($\sigma \leq 2$ h^{-1}Mpc), underdense regions contain more volume than overdense regions, indicating that these scales are prob-

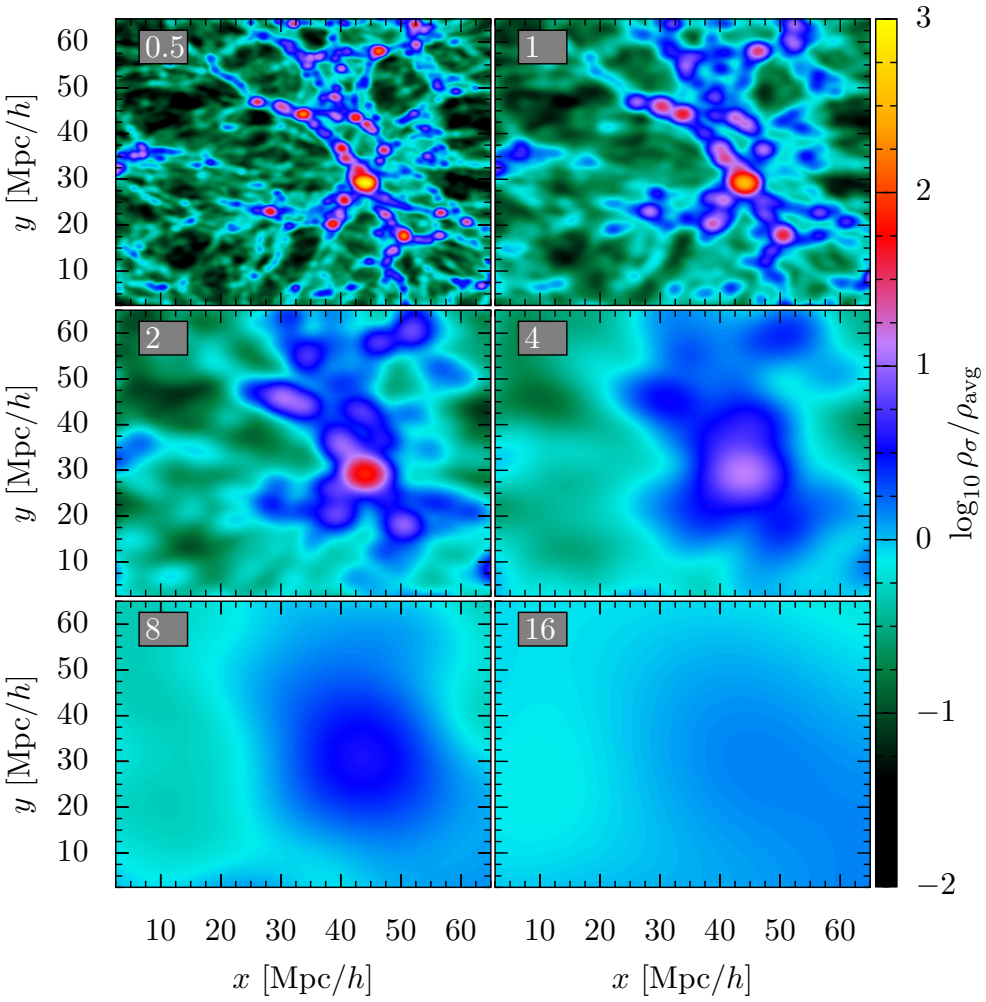

Figure 2.1: An example region of the Bolshoi Planck simulation at z = 0, coloured by local environment density smoothed on scales of σ = 0.5, 1, 2, 4, 8, and 16 h^{-1}Mpc. Densities are reported with respect to the average density of the full volume. The dynamic range of smoothed densities decreases at larger scales, dampening the color contrast between low and high density regions. Average density regions are highlighted by the light-blue to light-green color transition. This example region has a depth of 1/4 h^{-1}Mpc and a side length of 62.5 h^{-1}Mpc.

ing at or below the scales of non-linear structures like cosmic voids and filaments. At very high densities, the distributions become noisy due to poor statistics and sensitive to the voxelization of halo cores, especially for smaller smoothing scales.

2.3.1 Generalized Extreme Value Distribution

We find that the probability distributions of smoothed cosmic densities are well fit by a Generalized Extreme Value (GEV) distribution, as defined in Eq. 2.1, where x is a random variable, β is a scale parameter, k is a shape parameter, and μ is a location parameter. Extreme value theory (see, e.g., Kotz & Nadarajah, 2000; de Haan & Ferreira, 2006) describes the statistics of extrema of samples drawn from random distributions, and has been applied in analysis of 2D and 3D cosmological datasets (Colombi et al., 2011).

$$f(x) = \frac{1}{\beta}\exp\left[-\left(1+kz\right)^{-1/k}\right]\left(1+kz\right)^{-1-1/k}, \tag{2.1}$$

$$z = \frac{x-\mu.}{\beta} \tag{2.2}$$

The GEV distribution encompasses several sub-families known as the Gumbell, Weibull, and Fréchet distributions, distinguished by shape parameter $k = 0$, $k < 0$, and $k > 0$, respectively. In Table 2.1 we provide best fit values of β, k, μ, and the residual sum of squares (RSS) for each density distribution. The RSS is defined as

$$RSS = \sum_{n=0}^{m}\left[f\left(x[n],\beta,k,\mu\right) - P\left(x[n]\right)\right]^2, \tag{2.3}$$

where $f(\cdots)$ is a GEV distribution with parameters β, k, and μ, $x[n]$ are the binned density values and $P(x[n])$ is the real density distribution, as shown by the black lines in Fig. 2.2. We use a simulated annealing fitting algorithm to minimize the RSS between the fit and the data.

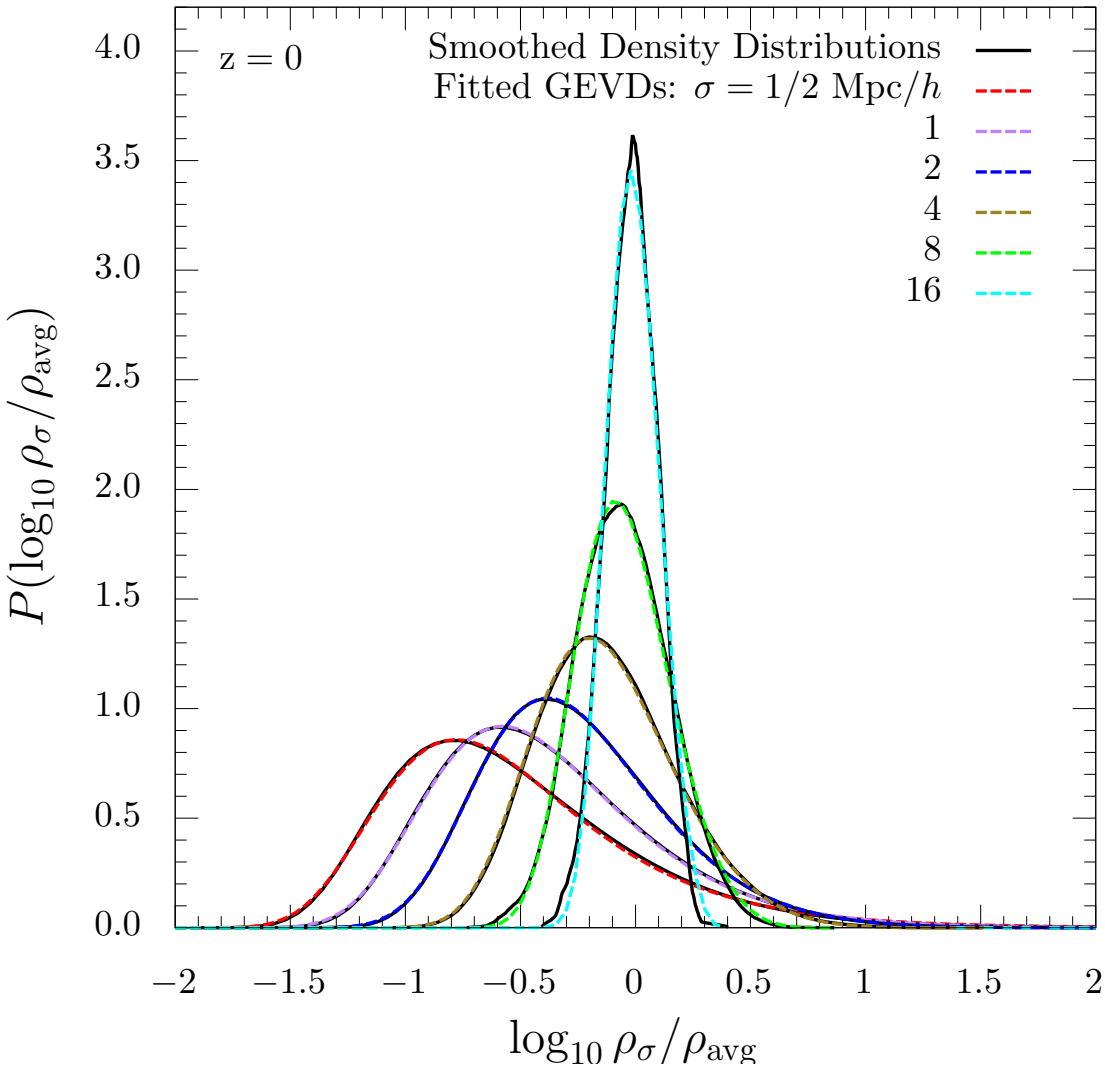
z = 0
Smoothed Density Distributions
Fitted GEVDs: $\sigma = 1/2$ Mpc/h
1
2
4
8
16
$P(\log_{10}\rho_\sigma/\rho_{\rm avg})$
$\log_{10}\rho_\sigma/\rho_{\rm avg}$
4.0
3.5
3.0
2.5
2.0
1.5
1.0
0.5
0.0
−2
−1.5
−1
−0.5
0
0.5
1
1.5
2

(a)

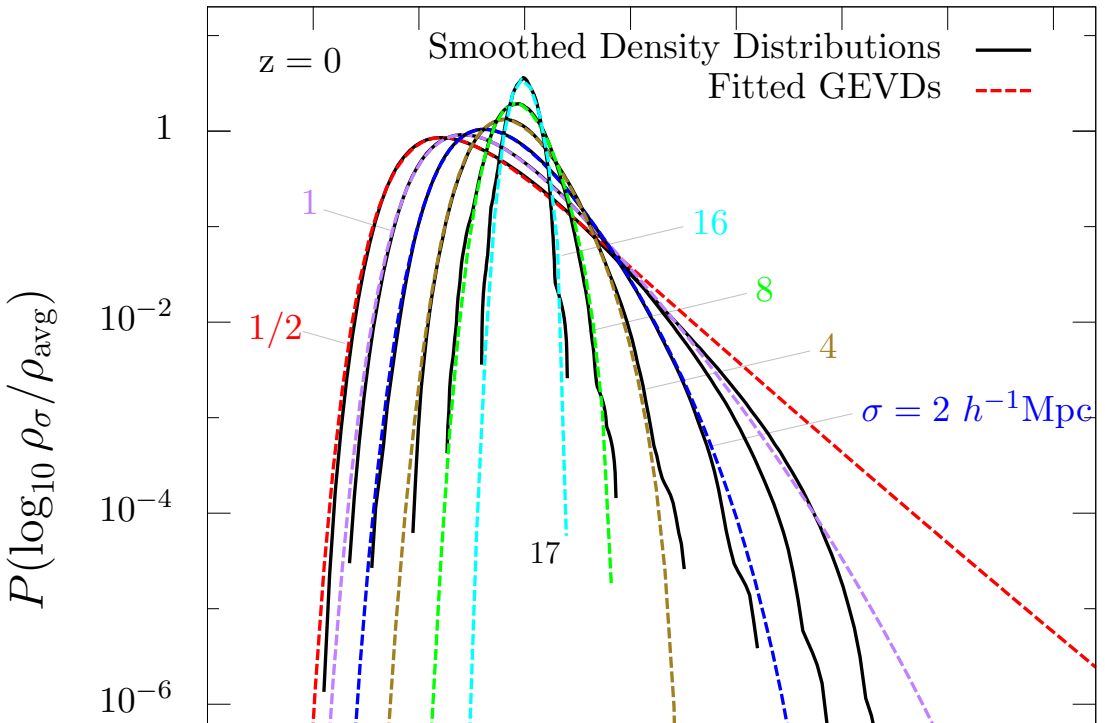
z = 0
Smoothed Density Distributions
Fitted GEVDs
1
16
8
4
1/2
$\sigma = 2\ h^{-1}$Mpc
17
$P(\log_{10}\rho_\sigma/\rho_{\rm avg})$
1
10^{-2}
10^{-4}
10^{-6}

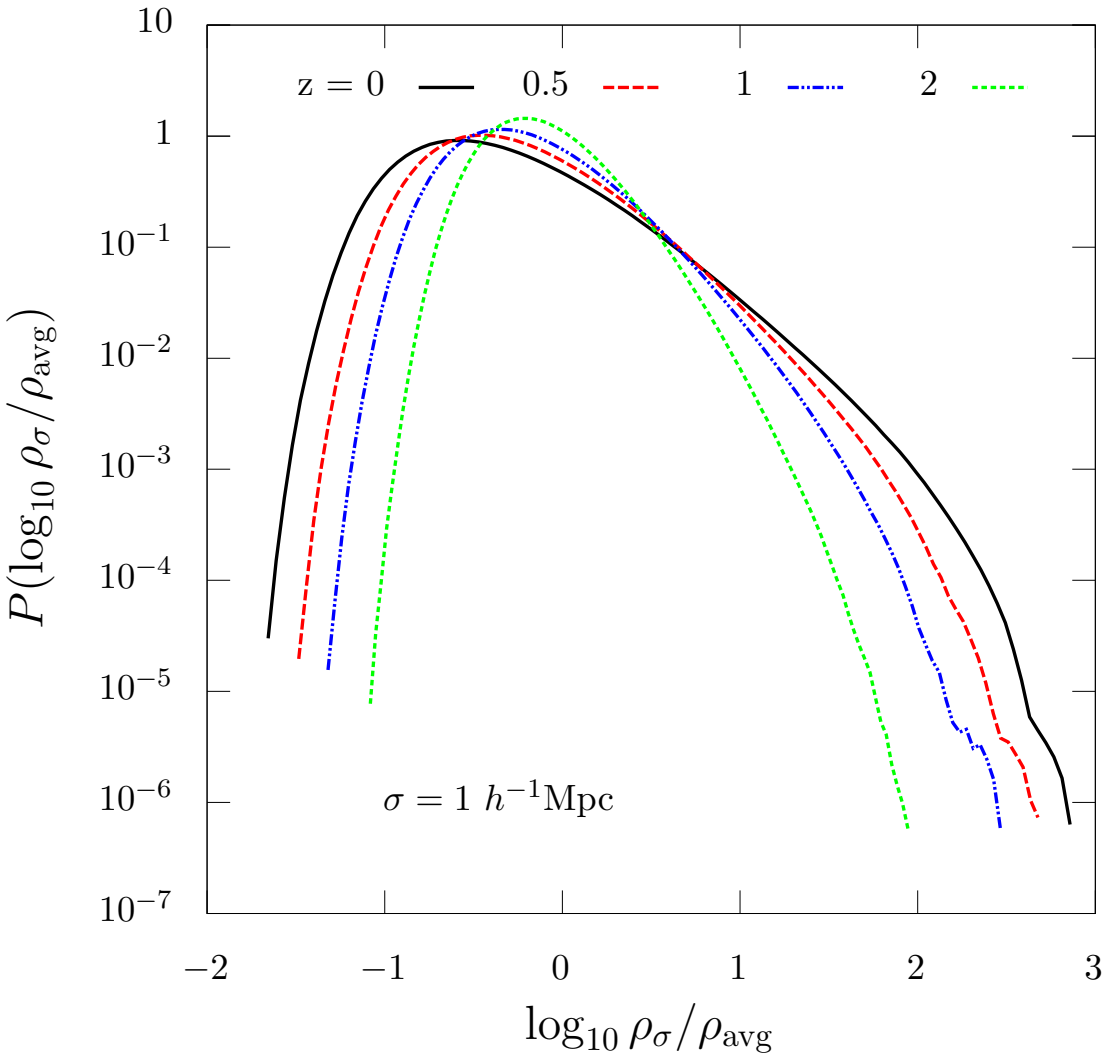

Figure 2.3: Probability distributions of local environment density smoothed using $\sigma_s = 1\ h^{-1}$Mpc for the entire simulation volume, shown with log scaling on the vertical axis. Different coloured lines represent the same smoothing scale, but at different redshifts. Non-linear structure emerges more dramatically at lower redshifts. Voids grow emptier, while filaments and clusters grow denser with time.

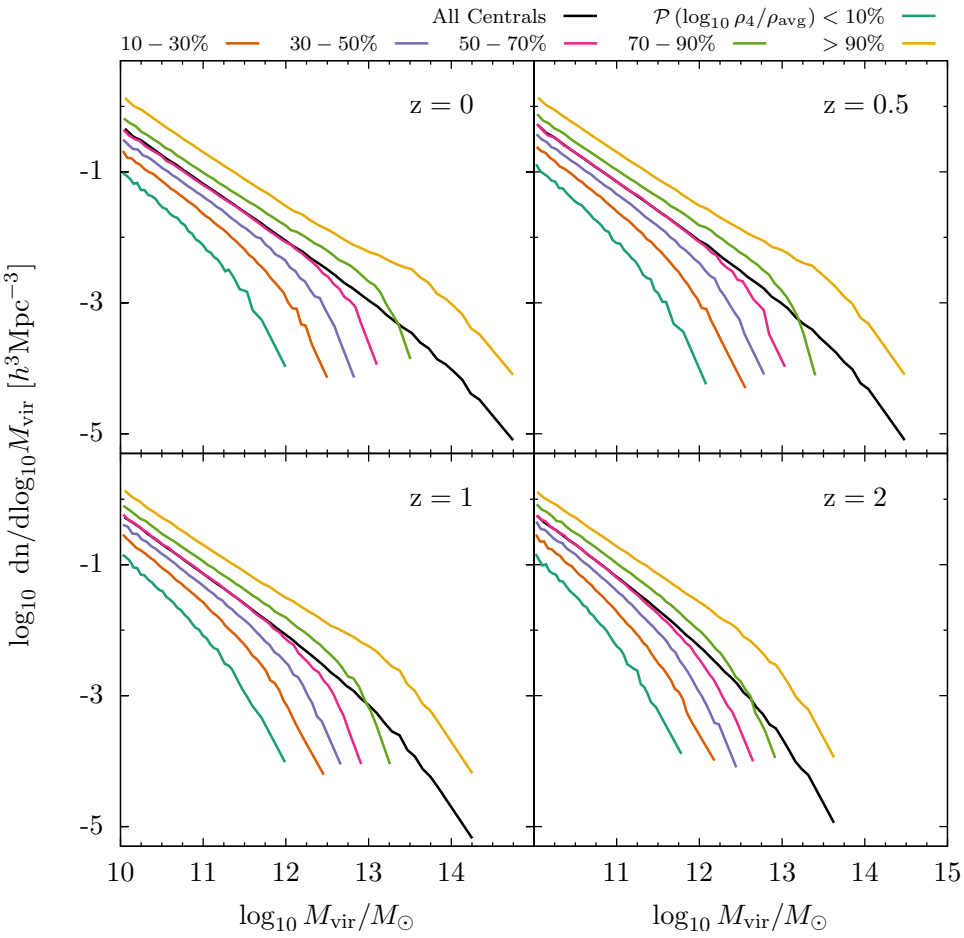

Figure 2.4: Halo mass functions at redshifts 0, 0.5, 1, and 2. Coloured lines represent halo mass functions computed in percentile bins of local environment density smoothed with $\sigma = 4\ h^{-1}$Mpc, while black lines indicate the mass function of all distinct halos. In order to consistently distinguish high from low density regions at different redshifts, we determine density percentiles relative to the whole simulation volume, rather than just the locations of the halos (e.g. $\mathcal{P} < 10\%$ reflects the lowest density voxels in the entire simulation, most of which are probably voxels in voids that contain no halos). We see that each mass function has a characteristic mass, above which the abundance drops off more rapidly. This characteristic mass is lowest in low density regions and highest in high density regions. We find that at $z = 2$, the characteristic masses are lower and cover a narrower range of masses compared to at $z = 0$. Additionally, at $z = 2$ the slopes of the mass functions change more gradually from below to above the characteristic masses compared to at $z = 0$. The mass function of halos in the highest density regions is also somewhat steeper above the characteristic mass compared to at $z = 0$. These differences reflect the flow of dark matter in the simulation: that voids become emptier and clusters become richer with time.

Table 2.1: Best fit values to 3-parameter generalized extreme value distribution (Eqns. 2.1, 2.2). σ is the HWHM smoothing length, β is the scale parameter, k is the shape parameter, μ is the location parameter, and RSS is the residual sum of squares between the fit and the data.

σ [h^{-1}Mpc]	β	k	μ	RSS
0.5	0.43	0.077	-0.78	0.0035
1	0.40	-0.049	-0.60	0.0012
2	0.35	-0.099	-0.42	0.00083
4	0.28	-0.16	-0.25	0.0026
8	0.19	-0.19	-0.13	0.095
16	0.11	-0.24	-0.051	1.47

We find that for small smoothing scales ($\sigma = 0.5$ and 1 h^{-1}Mpc), the distribution functions are well approximated by a Gumbell type distribution ($k \approx 0$), while larger smoothing scales (σ = 2, 4, 8, and 16 h^{-1}Mpc) are better approximated by a Weibull type distribution ($k < 0$). Furthermore, we note that $k \propto \log \sigma$ (i.e. k decreases nearly constantly in log space from $\sigma = 0.5$ to 16 h^{-1}Mpc, with the largest decrease occurring between $\sigma = 0.5$ and 1 h^{-1}Mpc). The location parameter μ, corresponding to the peak in the distributions, changes from $\mu \sim -1$ for small smoothing scales to $\mu \sim 0$ for larger scales, reflecting the shift in the abundances of voids on those scales. The scale parameter, correlating with the width of the distributions, decreases from $\beta \sim 0.5$ when smoothed on 1/2 h^{-1}Mpc scales to $\beta \sim 0.1$ for 16 h^{-1}Mpc scales.

2.3.2 Evolution with Redshift

We additionally calculate probability distributions of smoothed densities at redshifts $z = 0.5$, 1, and 2. In Fig. 2.3 we show the evolution of the distribution of densities smoothed with $\sigma = 1$ h^{-1}Mpc in comoving units (the simulation maintains a comoving volume of [250 h^{-1}Mpc]^3 at each time step). Fig. A.1 shows the distribution of densities smoothed with $\sigma = 4$ h^{-1}Mpc. Non-linear structure

emerges more dramatically at low redshifts, evidenced by the increasingly asymmetric peak at lower densities. Generally, we see that voids become less dense and higher density regions become more dense with time. Material in voids empties into walls, filaments, and nodes, which grow ever denser.

We note that Colombi et al. (1997) found a fitting function for the probability distribution of density using perturbation theory, and Sheth (1998) found that an Inverse Gaussian Distribution provided a good fit to the distribution of densities from simulations with white noise initial conditions. Valageas & Munshi (2004) developed a model for the evolution of the density probability distribution function. However, our GEV fits appear to be more accurate.

2.4 Environmental Dependence of Halo Mass Functions

We present halo mass functions at redshifts $z = 0$, 0.5, 1 and 2 for halos in different density regions in Fig. 2.4. We define consistent density ranges at each redshift by selecting percentile ranges of the smoothed CIC density values for the entire simulation volume, where coloured lines are computed in percentile bins of local environment density smoothed with $\sigma = 4\,h^{-1}$Mpc, while black lines indicate the mass function of all distinct halos. For example, $\mathcal{P} = 45 - 55\%$ selects halos with local densities equal to the median density of the entire simulation volume (including the densities of regions without halos). These selection criteria have the advantage of providing an intuitive and consistent definition for different redshifts, while still sampling a fairly wide range of halo local densities. Nevertheless, due to evolution in the distribution of local densities (Fig. 2.3), the population counts in these density percentile ranges change with redshift. The distribution of halo local

densities does not evolve in the same way that the whole volume does, since the halo distribution is mass-weighted rather than volume-weighted (i.e. we are not following evolution of voxels without halos). In general, the distribution of halo densities is more similar to the full volume density distribution at higher redshifts and for larger smoothing scales, and less similar at lower redshifts and smaller smoothing scales. As redshift decreases, halos tend to move towards higher density percentiles relative to the full volume densities. These trends are illustrated in Fig. A.2. Still, we feel this approach is more consistent than using percentile bins determined from halo densities alone, since it involves no choice of halo mass range. Choosing percentile ranges from halo densities would first require the selection of a halo mass range to use, which would have an arbitrary (user-defined) redshift dependence.

We find that each density range has a characteristic mass, above which the abundance of halos falls more rapidly. This characteristic mass increases monotonically with density, and is highest in the highest density regions. The characteristic mass for a given density range increases with decreasing redshift, and is highest at $z = 0$. However, the characteristic mass range (from the highest to lowest density regions) is narrower at high redshift than at low redshift. The slope of the mass function above the characteristic mass for halos in the highest density regions at $z = 2$ is also steeper than at $z = 0$. These differences reflect differences in the evolution of the mass-weighted halo density distribution relative to the volume-weighted full volume density distribution (Fig. A.2). At $z = 0$, we are probing a more extremal population of halos in the very highest and very lowest density regions compared to at $z = 2$. This effect is more pronounced in the highest density population than the lowest density population.

Naturally, we are interested to know how well these halo mass functions in

different density environments agree with observational data. We have several projects underway to address this topic. Using data from the Galaxy and Mass Assembly (GAMA) survey, McNaught-Roberts et al. (2014) determined galaxy local densities by counting surrounding galaxies within a sphere of 8 h^{-1}Mpc, and used them to compute galaxy luminosity functions in regions of different density. In ongoing work, our group is using abundance matching to compute luminosity functions in regions of different density, and comparing with data from the Sloan Digital Sky Survey (SDSS) and GAMA survey. In a different approach, we are using void density profiles from SDSS cosmic void catalogues (see, e.g. Sutter et al., 2012) to assign local densities to galaxies in low-density regions of the SDSS, which we can then use to test predictions from our simulations.

2.5 Correlations with Local Environment Density

2.5.1 Correlations at the present epoch

We turn our attention now to correlations between halo properties and local density at $z = 0$. In Fig. 2.5, we show medians of correlations between local density parameters and NFW concentration ($C_{\rm NFW}$), Bullock spin parameter ($\lambda_{\rm B}$), and dynamically time-averaged specific mass accretion rate ($\dot{M}/M$). Each column reflects a different halo mass range, while each row reflects a different halo property. We chose mass bins such that we could compare halos below, at, and above the characteristic mass $M_{\rm C}$ of halos that are collapsing at $z = 0$, which is $10^{12.70}{\rm M}_\odot = 5.0 \times 10^{12}{\rm M}_\odot$ for the Planck cosmological parameters used in the Bolshoi-Planck simulation (see Rodriguez-Puebla et al., 2016, Figure 9, for a plot showing $M_{\rm C}$ as a function of redshift). For each panel, different lines represent

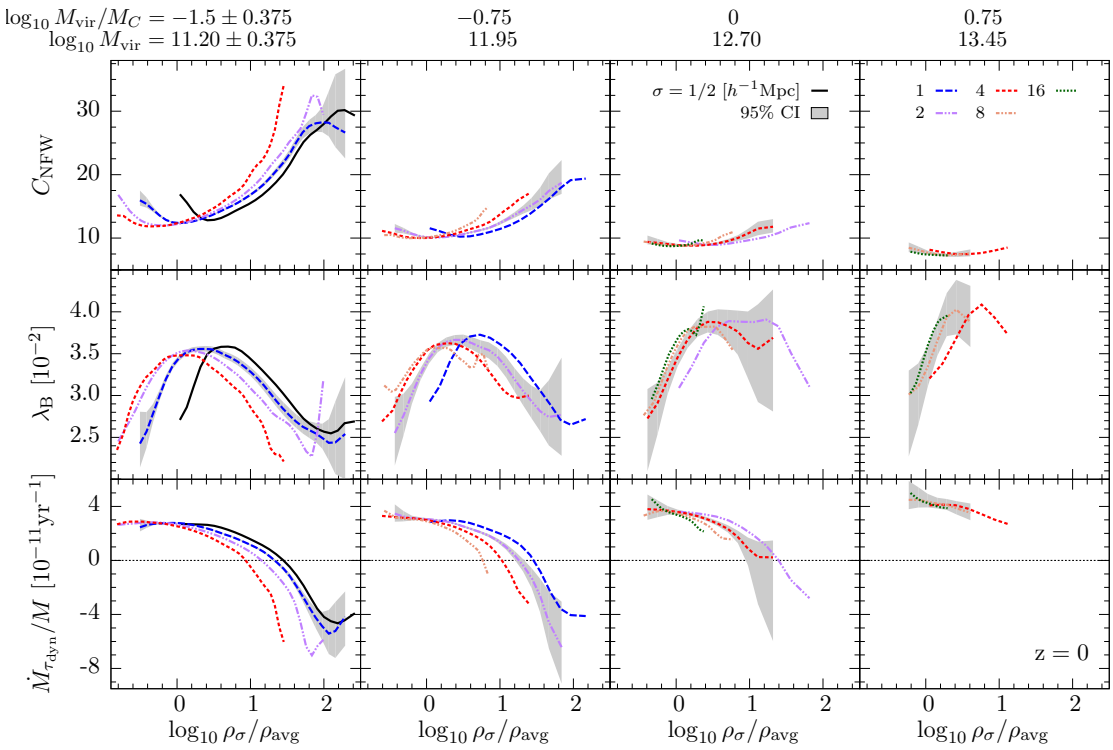

Figure 2.5: Medians of scatter in $\rho - C_{\rm NFW}$, $\rho - \lambda_{\rm B}$, and $\rho - \dot{M}/M$ relationships at $z = 0$, where ρ_σ is the local environment density smoothed on different scales and $\rho_{\rm avg}$ is the average density of the simulation. Different coloured lines represent different smoothing scales. The shaded grey filled curve represents the 95% confidence interval on the median, shown only for the characteristic smoothing length $\sigma_{s,\rm char} = 1, 2, 4$, and $8h^{-1}$Mpc for mass bins from left to right, respectively, and provides an indication of sample size at different densities. Mass bins are selected relative to the non-linear mass ($\log_{10} M_{\rm C} = 10^{12.7}{\rm M}_\odot$ at $z = 0$) to facilitate comparison between halos above, at, or below $M_{\rm C}$. We see that lower mass halos occupy regions with a wide range of local densities, while higher mass halos are restricted to higher density regions. Note also that larger smoothing scales will shift the range of densities towards the average density, so equal smoothing lengths should be used to compare density ranges for halos of different masses. See Fig. 2.6 for a discussion of the trends seen in this plot.

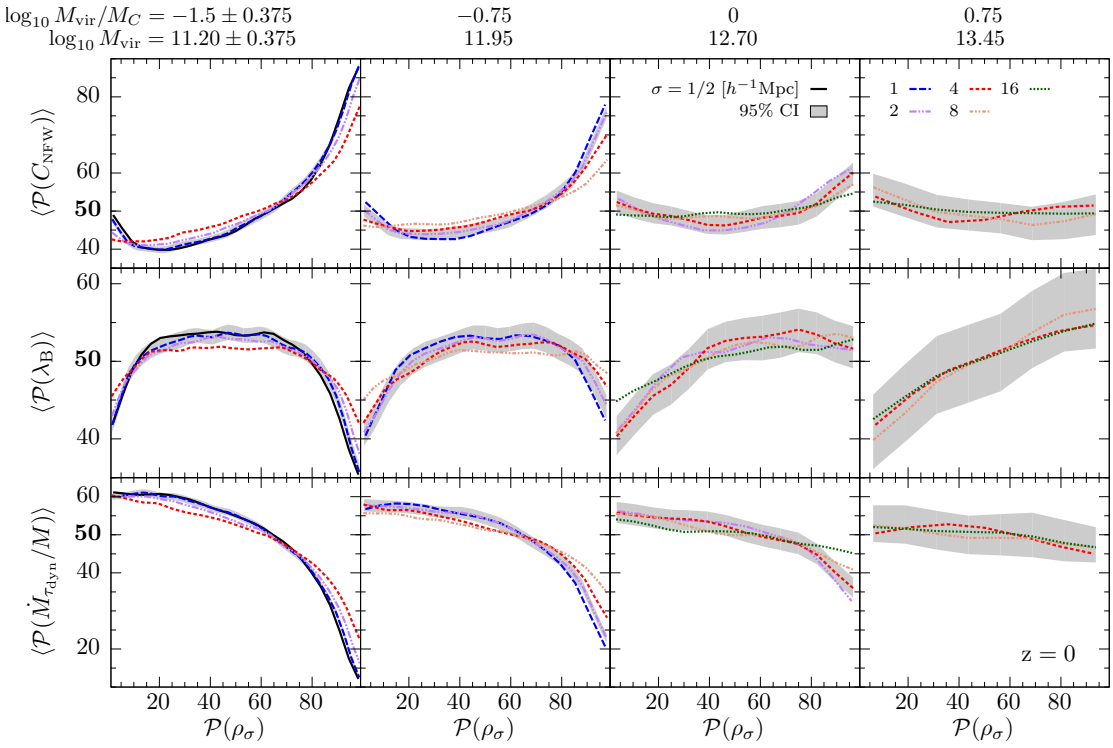

Figure 2.6: Medians of scatter in rank ordered distributions of $\rho - C_{\rm NFW}$, $\rho - \lambda_{\rm B}$, and $\rho - \dot{M}/M$ at $z = 0$. The vertical axes reflect the rank ordered percentile of the medians in each density percentile bin, with respect to all distinct (central) halos in the given mass bin. The shaded grey filled curve represents the 95% confidence interval on the median, shown only for the characteristic smoothing length $\sigma_{s,\rm char} = 1, 2, 4$, and $8h^{-1}$Mpc for mass bins from left to right, respectively. For halos less massive than $M_{\rm C}$, we see that concentrations tend to be lower in lower density regions, except at the lowest densities, where they increase. Spin parameters are maximized in median density regions, and decreased in high and low density regions. Accretion rates are heavily suppressed in high density regions and maximized in low density regions. For halos with $M_{\rm vir} \geq M_{\rm C}$, the trends are less dynamic and less well constrained due to low statistics, but show similar relationships overall. Note that high mass halos are not found in low density regions, so the trends observed represent trends in relatively high density regions only.

different smoothing radii used to determine the local density around halos. Due to the close relationship between virial radius and halo mass, we've plotted only smoothing radii that are greater than $\sigma_{s,min} \sim 4R_{\rm vir}$. We then define the characteristic smoothing length as $\sigma_{s,char} = 2\sigma_{s,min}$, which provides a reliable picture of local effects, while not being too much influenced by a halo's own profile or averaged out by larger smoothing scales. These characteristic smoothing radii are, from left to right columns, $\sigma_{s,char} = 1$, 2, 4, and 8 h^{-1}Mpc, respectively. To avoid overly crowding plots with lower mass halos, we plot only smoothing radii from $\sigma_s = \frac{1}{2}\sigma_{s,char}$ to $4\sigma_{s,char}$. The curves with corresponding grey shading reflect the 95% confidence interval on the median for the characteristic local density for a given mass bin.

In addition to choosing smoothing radii sufficiently greater than the virial radii of the halos, we balance each mass bin to have a flat mass-density relation. For a given mass bin, this involves 2 dimensional sub-binning by halo mass and a given local density parameter, then randomly eliminating halos from appropriate sub-bins to force approximately equivalent mass distributions for each density sub-bin (limited by the coarseness of the 2D sub-grid). We perform this procedure uniquely for each mass bin - density smoothing radius pair used. If this procedure is not done, the results would be contaminated by an underlying mass dependence, which is noticeable at smaller smoothing radii but rather insignificant for larger radii. Finally, we smooth the relations using a Gaussian filter with $\sigma = b(M_{\rm vir})$, where $b(M_{\rm vir})$ is the size of the horizontal (density) bins in a given mass bin. So, regions with wider density bins are smoothed with a larger σ than regions with narrow density bins. We determine bin widths based on the number of halos in the population under consideration, with better statistics allowing for smaller bins.

The resulting relations in Fig. 2.5 show some clear density dependence at

lower masses, where the range of local densities probed is high, while the data at high masses is comparatively flat and spans a narrower range of densities. The significantly extended range of densities home to lower mass halos reflects that these halos may be found in regions both underdense (voids) and very overdense (clusters), while more massive halos tend to reside exclusively in higher density regions. Additionally, lines representing different smoothing radii are shifted relative to each other, due to the averaging out of extreme densities with increasing smoothing scale.

In order to more effectively analyse these correlations, we prepared an alternate representation using percentilized axes. In Fig. 2.6, in a given mass bin, we've rank ordered halos by density parameter and the plotted halo property. The resulting curves represent the percentile ranks of the medians (determined relative to the entire mass bin) of each halo property for a given density percentile rank. This representation has the advantage of shifting and stretching the curves on each panel to facilitate comparison between different smoothing scales and halo masses. We also provide Fig. A.3 as a means of translation between Figs. 2.5 and 2.6, by relating actual values of halo properties to corresponding percentile ranks. This percentilized form of correlations between halo properties and local density will be the basis for much of our ensuing discussion.

In Fig. 2.6, we see that except in the lowest density regions, low mass halos ($M_{\rm vir} < M_{\rm C}$) have median concentrations that scale monotonically with increasing local density. Surprisingly, we also find that low mass halos in the lowest 15% of local densities have higher concentrations than halos in the roughly $20 - 40$th percentile range. So, for halo masses less than the characteristic mass $M_{\rm C}$, we find halo concentration scales strongly with local density, with the caveat that concentrations go up in very low density regions. Halos at or above $M_{\rm C}$ display a much

weaker correlation between density and concentration, though massive halos tend to be more concentrated in lower density regions. For $\lambda_{\rm B}$, we find that halos less massive than $M_{\rm C}$ in both high and low density regions have lower spin parameter compared to halos in median density regions. More massive halos, however, tend to have spin parameters that scale monotonically with local density. Lastly, all halos tend to accrete less in higher density environments, though low mass halos exhibit far stronger accretion suppression than massive halos. Interestingly, this indicates that halos in low density regions (bottom 20% of densities) accrete more rapidly than halos in higher density regions.

2.5.2 Redshift evolution of halo properties at different densities

One of the principal analysis methods we've used to investigate the origins of the trends in Fig. 2.6 is to examine the median evolution of halo properties along the most massive progenitor branch (MMPB) of halos in regions of different density at $z = 0$. In Figs. 2.7 and 2.8, for a given mass bin, we've selected all halos in the $0-10$th, $45-55$th, and $90-100$th percentile ranges of characteristic local density $\sigma_{s,char}$ at $z = 0$ to represent halos in low, median, and high density regions, respectively. Using the halo merger trees, we follow the MMPB of each halo and record the properties of each progenitor. We then present the median halo properties of the most massive progenitors of halos that end up in these low, median, and high density regions at $z = 0$. Note that because the density selections are made at $z = 0$, the progenitors of those halos are not guaranteed to reside in similar density regions at higher redshifts. Once an MMPB mass drops below the completeness threshold $M_{\rm min} = 10^{10}{\rm M}_{\odot}$, we discard any remaining progenitors from the analysis. This is done in order to exclude halos with low

particle counts that may have unreliable halo properties. The dark grey and light grey shading reflect the 95% confidence interval on the median and the $20-80$th percentile range of the halo property at a given redshift, respectively. These are shown only for halos in median density regions at $z = 0$, though similar trends apply to halos in low and high density regions at $z = 0$.

In order to minimize bias introduced by the longest lasting MMPBs (those that remain above $M_{\rm min}$ out to higher than average redshifts), we implement a "median preserving" approach. Tracing time backwards from $z = 0$, when a given MMPB drops below $M_{\rm min}$, we determine the halo property rank of that MMPB's earliest eligible progenitor $P_{\rm earliest}$ (with $M_{\rm vir} > M_{\rm min}$) with respect to all other eligible halos at that time step. Then, in addition to eliminating further progenitors of $P_{\rm earliest}$, we eliminate progenitors of the MMPB with rank $R' = N - R$, where N is the total number of halo progenitors in consideration at the relevant redshift and R is the rank of $P_{\rm earliest}$. For example, if the earliest eligible progenitor P_i of a given MMPB ranks in the 67th percentile in $C_{\rm NFW}$ compared to all other eligible progenitors at that redshift, then in addition to eliminating the remaining progenitors of P_i, we eliminate any remaining progenitors of the MMPB that ranks in the $100 - 67 = 33$rd percentile in $C_{\rm NFW}$ at that same redshift. This procedure is applied uniquely for each halo property presented and provides a less biased determination of the median properties of halo progenitors than a simple low statistics cut-off. For example, if we naively plot the median mass evolution of a group of halos, excluding progenitors that fall below $10^{10}{\rm M}_{\odot}/h$, the median mass of the group will not fall below that threshold until every single halo in the group has done so. Using the median preserving approach, however, the median halo mass would fall below the threshold sooner, because high mass progenitors would be paired off and removed along with low mass progenitors. Finally, each

curve is smoothed using a Gaussian filter with smoothing σ = 2, 3, 6, and 10 time steps for mass bins from left to right columns, respectively. We discuss our interpretation of Fig. 2.7 and related progenitor property figures in the following sections.

2.5.3 Mass Accretion Rate

In Figs. 2.5 and 2.6, we use the dynamically time averaged specific mass accretion rate, defined as

$$\frac{\dot{M}_{\tau_{\rm dyn}}}{M} = \frac{1}{M(t)} \frac{M(t) - M(t - \tau_{\rm dyn})}{\tau_{\rm dyn}}, \tag{2.4}$$

while in Fig. 2.7 we use the instantaneous specific mass accretion rate, defined at a given timestep t_i, as

$$\frac{\dot{M}}{M} = \frac{1}{M(t_i)} \frac{M(t_i) - M(t_{i-1})}{t_i - t_{i-1}}. \tag{2.5}$$

See Rodriguez-Puebla et al. (2016) Appendix A for details about the timesteps saved in the Bolshoi-Planck simulation we are using. In Fig. 2.6 we see that except for the most massive halos, those in higher density regions have suppressed accretion rates compared to halos in lower density regions. From Fig. 2.5, we can additionally see that in very high density regions, the median accretion rates for halos less massive than $M_{\rm C}$ even become substantially negative, indicating a net loss, or "stripping" of material from the halo. Accretion rates of halos in median and low density regions tend to be very similar, if not marginally higher in low density regions. It should again be noted that halos more massive that $M_{\rm C}$ span a much narrower range of local densities and have far poorer statistics compared to less massive halos, resulting in typically less dynamic correlations between halo

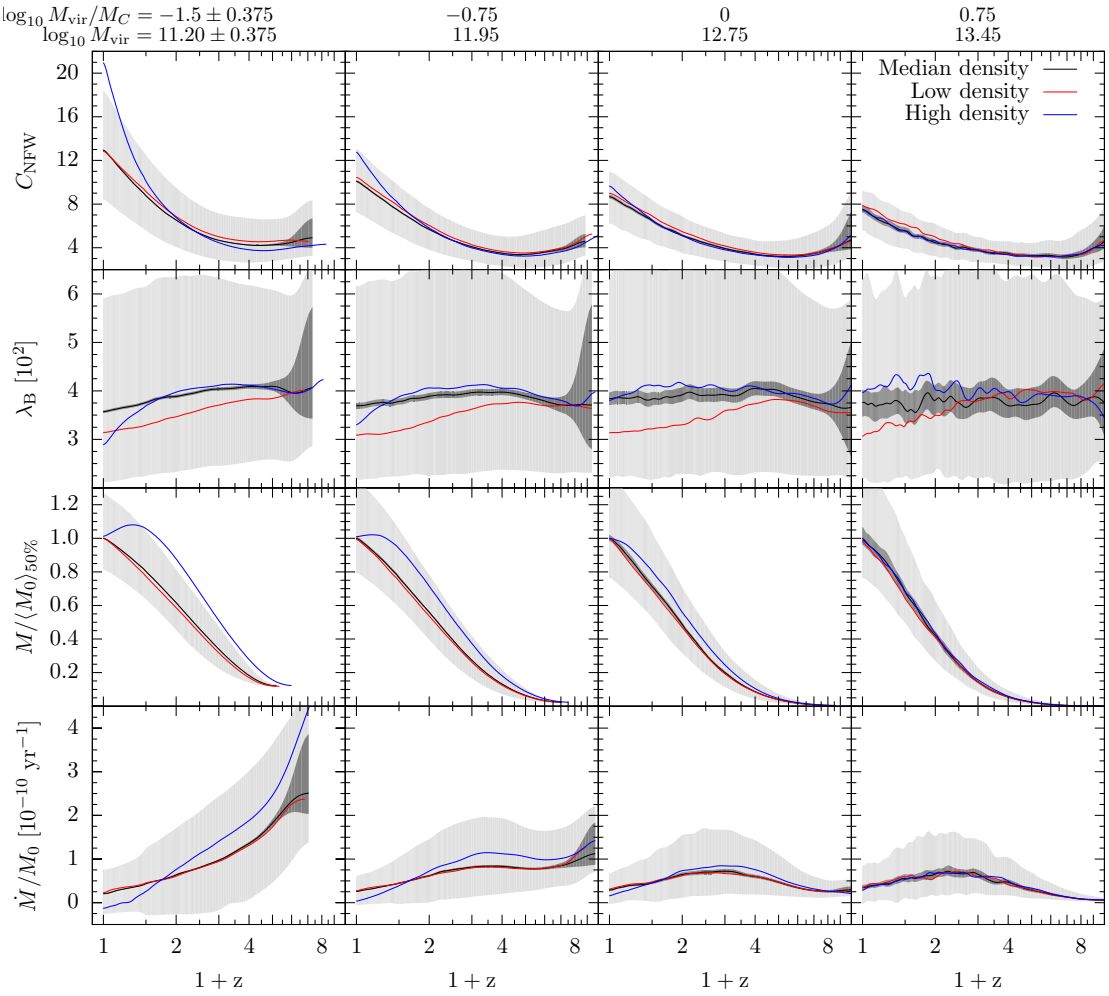

Figure 2.7: NFW Concentration, spin parameter, mass, and specific mass accretion rate histories for halos that end up in high (blue), median (black), and low (red) density regions at z = 0. Halos are selected based on their percentile rank in characteristic local density parameter ($\sigma_{s,\rm char} = 1, 2, 4$, and $8h^{-1}$Mpc for mass bins from left to right, respectively). Halos that are in the percentile ranges $\mathcal{P} = 0-10, 45-55$, and $90-100$ represent halos in low, median, and high density regions, respectively. The curves reflect median properties of the progenitors of the z = 0 halo populations. The dark grey shading reflects the 95% confidence interval on the median and the light grey shading reflects the $20-80\%$ dispersion of each property, shown only for halos in median density regions. We see that low mass halos in high density regions at $z = 0$ experienced rapid growth of concentration and reduction of spin parameter at late times compared to halos in lower density regions. Halos in high density regions also experienced sharp accretion rate suppression and even mass loss at late times. Halos in low density regions at $z = 0$ had slightly higher concentrations and consistently lower spin parameters than halos in median density regions throughout most of their history. Halos in low density regions accreted slightly less at early times and slightly more at late times compared to halos in median density regions.

properties and local density.

Fig. 2.7 Rows 3 and 4 show the evolution of virial mass and instantaneous specific accretion rate for halos in low, median, and high density regions at $z = 0$. Halos in high density regions tend to have much more massive progenitors compared to halos in median and low density regions and accrete material more rapidly and sooner than halos in lower density regions. Halos in high density regions also experience much lower accretion rates at late times.

In Fig. 2.9 Row 1, we plot the relation between local density and the half-mass scale factor $a_{M_{1/2}}$, used in this analysis as an indicator of halo formation time. Consistent with the mass growth profiles from Fig. 2.7, we see that low mass halos in high density regions form earlier than halos in lower density regions. In Fig. 2.8 Row 1, we see that halos in high density regions at $z = 0$ experience much higher tidal forces than halos in lower density regions, particularly at $z \lesssim 1$. Furthermore, Fig. 2.9 Row 3 shows that tidal force correlates strongly with local density. Thus, tidal forces histories along the MMPBs of $z = 0$ halos are probably closely related to their local density histories. For halos in high density regions at $z = 0$, the strongly reduced median tidal force their progenitors experience at redshifts $z \gtrsim 1$ indicates that those progenitors live in closer to median density regions at earlier times, and only enter very high density regions at late times ($z < 1$). Halos in high density regions at $z = 0$ thus form earlier and accrete significant amounts of material sooner than halos in lower density regions, however migration into very high density regions at $z < 1$ results in strongly reduced accretion rates and even net mass loss among lower mass halos. Halos in high density regions, corresponding to regions with strong tidal fields, have suppressed accretion rates due to the reduced impact parameters infalling material would require to be captured by the halo (Hahn et al., 2009a; Hearin, Watson & van den

Bosch, 2015). Additionally, halos may lose weakly bound particles or those whose orbits are sufficiently elongated.

Halos in lower density regions tend to have higher accretion rates than halos in higher density regions, though this trend plateaus for halos in regions of less than median density. One may expect accretion rates to be reduced in low density regions, due to the presumably decreased amount of local material available for accreting, but we find this is not the case. In fact, in Fig. 2.7 Row 3, we see that halos in low density regions evolve from slightly less massive progenitors than halos in median density regions, implying that halos in low density regions must accrete more rapidly at late times to end up with the same $z = 0$ masses as halos in median density regions. Indeed, in Fig. 2.7 Row 4, we see that the accretion rate histories of these two halo populations are extremely similar, albeit with halos in low density regions accreting marginally less at high redshifts ($z \gtrsim 1$) and slightly more at low redshifts than halos in median density regions (consistent with the mass growth profiles). Halos in low density regions experience consistently lower tidal forces throughout their lifetimes than halos in median density regions. This suggests that halos in low density regions may be able to accrete a larger fraction of available surrounding material than halos in median density regions due to decreased competition from neighbouring halos.

2.5.4 Concentration

In this paper, we use the Navarro, Frenk & White (1996, NFW) radial density profile to define concentration,

$$C_{\rm NFW} \equiv R_{\rm vir}/R_s, \tag{2.6}$$

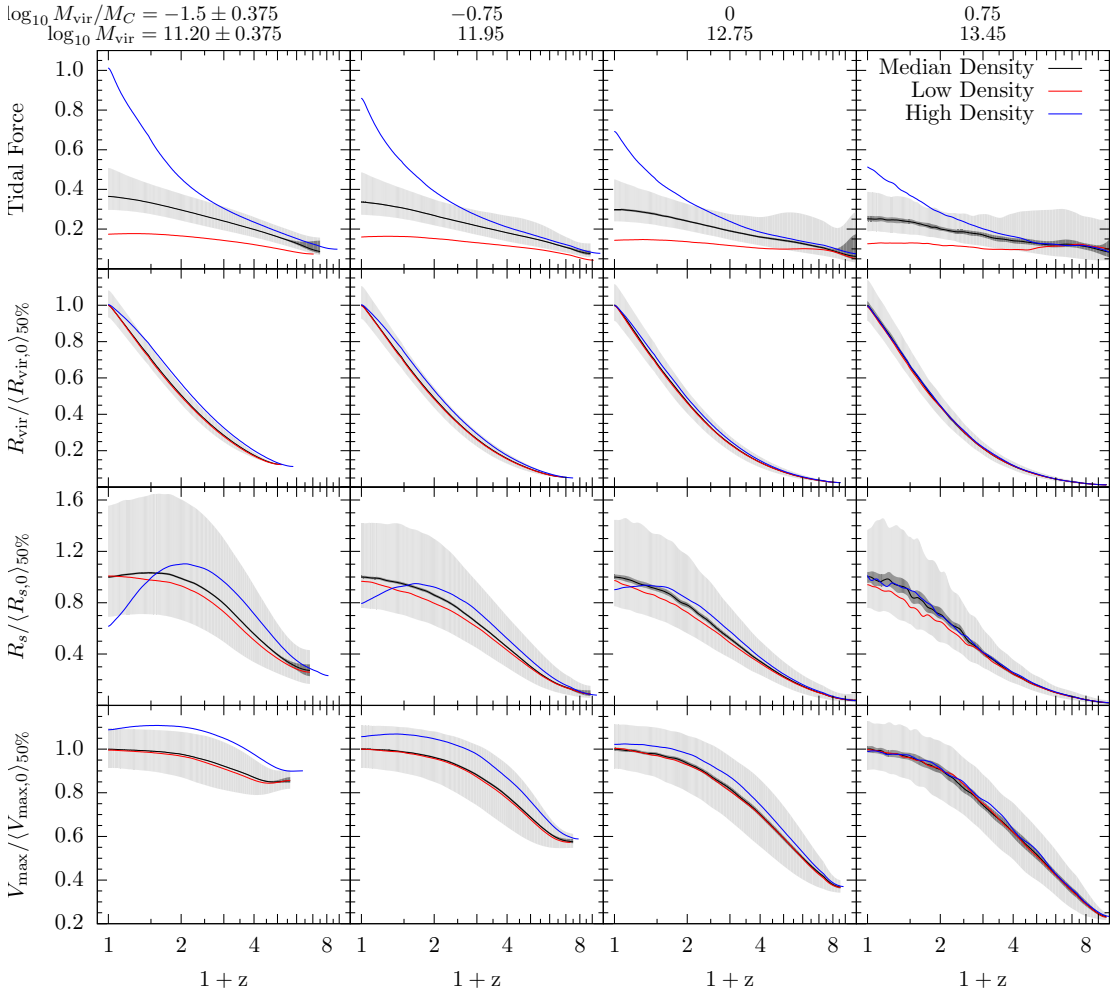

Figure 2.8: Same as Fig. 2.7, but showing tidal force, virial radius ($R_{\rm vir}$), scale radius (R_s), and maximum circular velocity ($V_{\rm max}$). In order to efficiently compare different mass bins, we normalize $R_{\rm vir}$, R_s, and $V_{\rm max}$ by the median values of the median density population at $z = 0$. We see that halos in high density regions at $z = 0$ experience strong tidal forces at late times, but significantly weaker tidal forces at higher redshifts. Since tidal force correlates strongly with local density, it seems halos in high density regions at $z = 0$ migrated from roughly median density regions around $z \lesssim 2$. Halos in high density regions at late times evolved from halos with larger $R_{\rm vir}$ and R_s and higher $V_{\rm max}$ compared to halos in lower density regions, but experienced a dramatic reduction in scale radius at late times. Halos in low density regions at $z = 0$ experienced consistently low tidal forces throughout their evolution and somewhat lower scale radii than halos in median density regions.

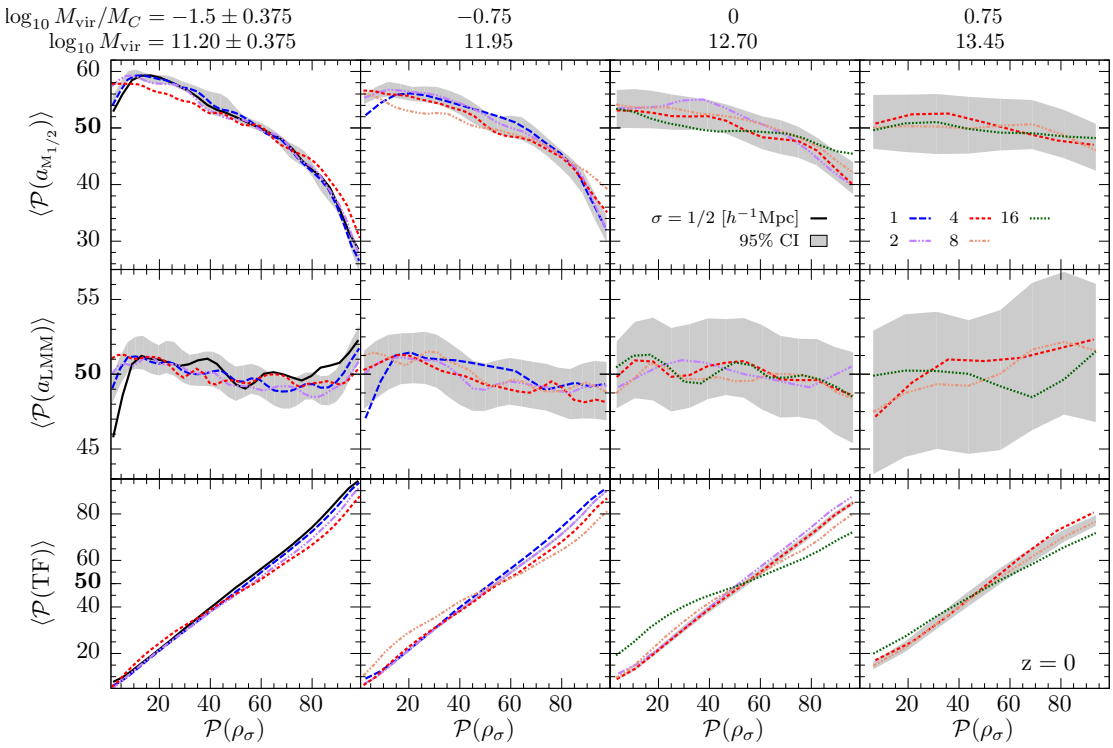

Figure 2.9: Same as Fig. 2.6, but showing half-mass scale factor ($a_{M_{1/2}}$), scale of last major merger ($a_{\rm LMM}$) and tidal force. We see that the percentilized $a_{M_{1/2}} - \rho$ relation is roughly inversely proportional to the $C_{\rm NFW} - \rho$ relation. Low mass halos in high density regions typically formed earlier than halos in lower density regions, except in the lowest density regions, where we see a downturn in $a_{M_{1/2}}$. Low mass halos in very low density regions most recently experienced major mergers at earlier times than halos in higher density regions. We observe little correlation between $a_{\rm LMM}$ and local density above $\mathcal{P}(\rho_\sigma) \approx 20$. Tidal forces correlates strongly with local density, suggesting we can use tidal force history as a reliable tracer of local density history.

where the scale radius R_s is determined by fitting a halo to the NFW profile,

$$\rho_{\rm NFW}(r) = \frac{4\rho_s}{(r/R_s)(1+r/R_s)^2}. \tag{2.7}$$

For halos with less than 100 particles, we revert to using the Klypin concentration $C_{\rm Klypin}$ (see, e.g. Klypin, Trujillo-Gomez & Primack, 2011; Rodriguez-Puebla et al., 2016), which can be solved for numerically using a relationship between $V_{\rm max}$ and $M_{\rm vir}$. Most of our analysis focuses on halos with more than 100 particles, except for when we follow the progenitors of halos to high redshift (e.g. Fig. 2.7). However, for comparison with Fig. 2.6, we also provide relations between $C_{\rm Klypin}$ and local density in Fig. A.5. We do not include halos below $M_{\rm vir} = 10^{10}\ h^{-1}$Mpc ($\sim 70$ particles) in any part of our analysis.

From Fig. 2.6 Row 1, we see that NFW Concentration ($C_{\rm NFW}$) of low mass halos ($M_{\rm vir} < M_{\rm C}$) scales monotonically with local density, except for in low density regions, where we see an upturn in concentration. Higher mass halos ($M_{\rm vir} \geq M_{\rm C}$) display little correlation between concentration and local density, though it should be noted that higher mass halos tend to be confined to higher density regions. The fundamental questions raised here are: (1) why do low mass halos in high density regions have much higher concentrations; and (2) why do low mass halos in very low density regions ($\mathcal{P}(\rho_\sigma) < 20$) have higher concentrations than those in somewhat higher density regions ($\mathcal{P}(\rho_\sigma) \approx 20-50$)? In order to understand these trends, we now examine correlations between several additional halo properties and local density, as well as the time evolution of halo concentration and related halo properties in regions of different density.

First, we look at the correlation between halo formation time and local density. We use the scale factor at which a halo first reached half its peak mass ($a_{M_{1/2}}$) as an indicator of formation time. In Fig. 2.9 Row 1, we plot the relation between

half-mass scale factor and local density, using the same method and plotting styles as in Fig. 2.6. Especially for lower mass halos, we see that the relation between half-mass scale factor and density is inversely proportional to the $C_{\rm NFW}$-ρ_σ relation, even for the lowest density regions. This indicates that halos in higher density regions generally formed earlier than those in lower density regions, with the exception that halos in very low density regions ($\mathcal{P}(\rho_\sigma) < 20$) typically formed somewhat earlier than those in slightly higher density regions ($\mathcal{P}(\rho_\sigma) \approx 20$). If we assumed a simple model for concentration evolution, such as $C_{\rm NFW} \propto (1+z)^{-1}$ at fixed mass as in Bullock et al. (2001), then the inverse proportionality between the $C_{\rm NFW} - \rho_\sigma$ and $a_{M_{1/2}} - \rho_\sigma$ relations would seem consistent; halos in high density regions have higher concentrations *because* they formed earlier, and thus have had more time to grow $C_{\rm NFW}$. However, this conclusion assumes that halo concentration evolves at the same rate in regions of different density, which, as we will show, is not the case.

We plot in Fig. 2.9 Row 2 the relation between the scale factor of the last major merger ($a_{\rm LMM}$) and local density. Overall the correlation is very weak, except for low mass halos in very low density regions, where we see that halos typically last experienced a major merger earlier than halos in higher density regions. The downturn at low densities in the $a_{\rm LMM} - \rho_\sigma$ relation roughly corresponds to the downturn at low densities in the $a_{M_{1/2}} - \rho_\sigma$ relation, upturn in $C_{\rm NFW}$, and downturn in $\lambda_{\rm B}$, indicating these may all be due to the same mechanism.

We now turn to the evolution of halo concentration in regions of different density. In Fig. 2.7 Row 1, we select groups of halos in high, median, and low density regions at $z = 0$ and plot the median concentrations of their progenitors at each time step. What we immediately see is that low mass halos in high density regions have only recently ($z \lesssim 1$) diverged sharply in concentration compared to

halos in median and low density regions. In fact, we see that at higher redshifts ($z \gtrsim 1$), the $z = 0$ high density halos had equal, if not slightly lower concentrations than halos that end up in median and low density regions at $z = 0$. Clearly, low-mass halos in high density regions have drastically different rates of concentration growth than halos in lower density regions at late times. Halos in low density regions historically have slightly higher concentrations than those in median density regions, though overall the difference between the two is slight. However, we should keep in mind that from Fig. 2.6 Row 1 we see that the upturn in concentration for halos in very low density regions occurs around $\mathcal{P}(\rho_\sigma) \approx 20$, so by comparing low density ($\mathcal{P}(\rho_\sigma) = 5$) to median density ($\mathcal{P}(\rho_\sigma) = 50$), we are somewhat obscuring the low density upturn. Nevertheless, there does seem to be a systematic difference between concentrations histories of halos in median and low density regions at z = 0. These results redirect our questions as follows: (1) why do halos in high density regions at $z = 0$ exhibit drastically increased concentrations at late times compared to halos in lower density regions; and (2) why do halos in low density regions at $z = 0$ have systematically higher concentrations throughout most of their lifetimes?

Our next step is to break down the concentration evolution by examining the evolution of virial radius $R_{\rm vir}$ and scale radius R_s, which are related by $C_{\rm NFW} = R_{\rm vir}/R_s$. In Fig. 2.8 Rows 2 and 3, we plot the evolution of virial radius and scale radius for halos in regions of different density at $z = 0$. We see that all halos have relatively similar virial radii (as one would expect, given that we have normalized the mass-density correlation within each mass bin). Halos in high density regions had larger virial radii at earlier times, reflecting that they evolved from higher mass halos than the median and low density groups (see also Fig. 2.7 Rows 3 and 4 for accretion history comparison). However, the variation in

virial radius between halos in different density environments does not significantly contribute to the large concentration discrepancy at late times. This leaves the scale radius, which indeed shows drastically different evolution between halos in different density regions. Low mass halos ($M_{\rm vir} < M_{\rm C}$) in high density regions at $z = 0$ experience rapid scale radius growth at early times, followed by a plateau around $z = 1$, and a sharp decline at late times. We see a similar growth and plateau trend in median and low density regions, but no significant decrease in scale radius. Additionally, low mass halos in low density regions have consistently lower scale radii than halos in median density regions. This systematic difference in scale radius growth rate between halos in median and low density regions at $z = 0$ suggests there may be differences in the accretion histories of the two populations, but as shown in Fig. 2.7 Row 4, the instantaneous accretion rate histories are practically identical. However, we note that the redshift at which the accretion rate of halos in high density regions crosses below the accretion rate of halos in median and low density regions roughly corresponds to the redshift at which the scale radii of halos in high density regions begins to decrease.

Since the scale radius represents the location at which the spherically averaged density profile transitions from an inner $\rho \propto r^{-1}$ to an outer $\rho \propto r^{-3}$ dependence, the differences in scale radius evolution indicate fundamental differences in the evolution of halo density profiles in regions of different density. So, do halos in high density regions really have scale radii that are shrinking (r^{-1} core physically decreasing in size)? One way to probe structural changes to the central regions of these halos is by looking at maximum circular velocity evolution $V_{\rm max}$, shown in Fig. 2.8 Row 4. The systematically higher $V_{\rm max}$ for halos in high density regions is a reflection of their more massive progenitors. We see that low mass halos in high density regions at $z = 0$ do display slightly decreased $V_{\rm max}$ at late

times, indicating some net loss of high energy particles from the central regions of these halos. However, this is not a strong effect, and certainly not indicative of a drastically reduced scale radius. This suggests that these halos likely have density profiles that are evolving away from the NFW profile, resulting in a poor NFW fit with artificially reduced R_s values. Indeed, most low mass halos in high density regions have outer density profiles that fall off faster than r^{-3} (Avila-Reese et al., 1999), presumably due to tidal stripping of material from the outer regions of these halos. Forcing an NFW fit to these halos will tend to produce artificially small R_s values, due compensation for the steep fall off of their outer density profiles.

As shown by the halo mass evolution plot (Fig. 2.7 Row 3), low mass halos in high density regions have dramatically reduced $M_{\rm vir}$ at late times, due to negative accretion rates (i.e., stripping of material from the halos). Halos in high density regions tend to be much more stripped than halos in low density regions. Furthermore, in Fig. A.7, we see that when halos that have lost more than 2% of their peak mass are removed from the population, the median halo concentration sharply decreases in high density regions, but changes little in median and low density regions. This suggests that inflated concentrations in high density regions are simply a consequence of the modified density profiles (and subsequently poorer NFW fits) of halos that are undergoing extreme mass loss. While exceptionally high concentrations correlate strongly with halos in very high density regions, they are a poor and indirect descriptor of the properties of these halos. It would be better to characterize these halos using a fitting function that properly fits their outer regions. We are currently investigating how to best characterize halo profiles in regions of different density and for halos that have been appreciably stripped.

There are only small differences in concentration evolution between halos in low density regions and those in median density regions, suggesting that differences in the median formation times may be the main reason for differences in the median concentrations of these populations. Low mass halos in low density regions typically formed earlier, and have had more time to increase their concentrations compared to halos in median density regions. Early forming halos will also tend to have higher central densities and smaller scale radii than late forming halos.

2.5.5 Spin Parameter

Next, we investigate the local density dependence of spin parameter. We present results for both the Bullock spin parameter (Bullock et al., 2001) and the Peebles spin parameter (Peebles, 1969a), defined as

$$\lambda_{\rm B} = \frac{J}{\sqrt{2} M_{\rm vir} V_{\rm vir} R_{\rm vir}}, \tag{2.8}$$

and

$$\lambda_{\rm P} = \frac{J \left|E\right|^{1/2}}{G {M_{\rm vir}}^{5/2}}, \tag{2.9}$$

respectively, where J and E are the total halo angular momentum and energy, and G is the gravitational constant. However, we focus our analysis on $\lambda_{\rm B}$.

We see from Fig. 2.6 Row 2 that at $z = 0$ low mass halos ($M_{\rm vir} < M_{\rm C}$) in high density regions have lower spin parameters than halos in median density regions. Similarly, halos in low density regions have distinctly lower $\lambda_{\rm B}$ than halos in median density regions for all masses. We note that the downturn in spin parameter for halos in low density regions occurs at roughly the same density as the upturn in concentration for these same halos (Fig. 2.6 Row 1), suggesting that the underlying cause of these trends may be related. The relation between local

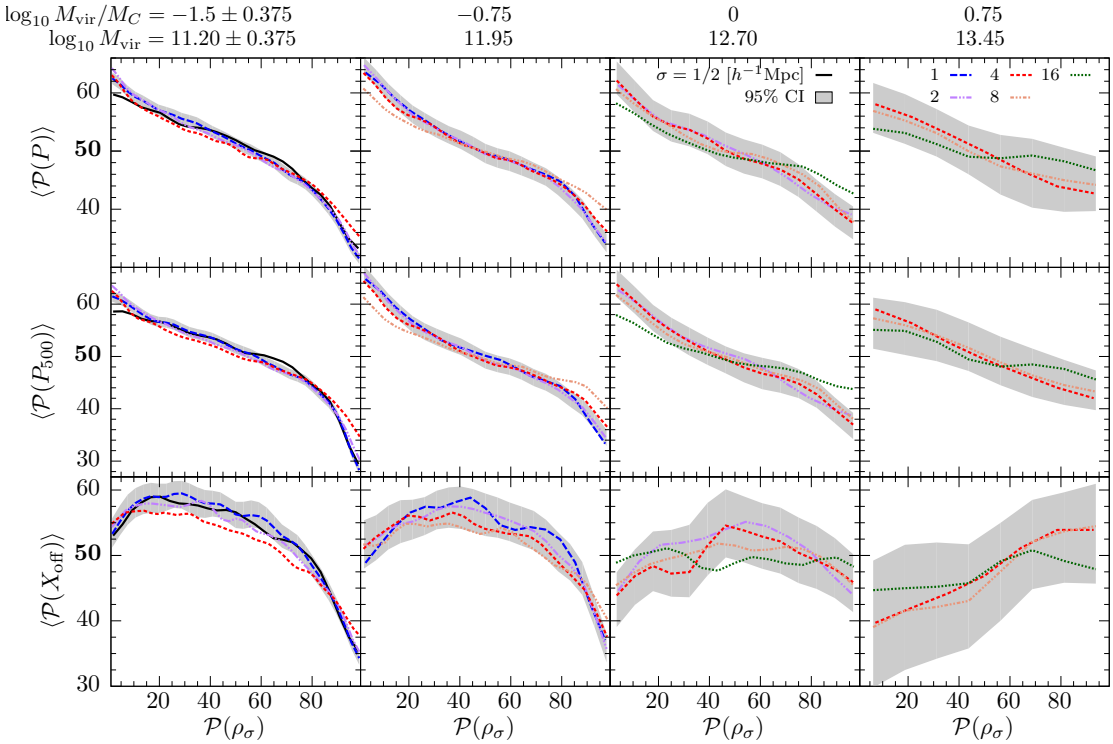

Figure 2.10: Same as Fig. 2.6, but showing prolateness at $R_{\rm vir}$ (P), prolateness at R_{500c} (P_{500c}), and the offset of halo center of mass from halo peak density ($X_{\rm off}$). We see that prolateness measured at both $R_{\rm vir}$ and R_{500c} monotonically decrease with increasing local density density for all masses and all smoothing scales. Prolateness is one of only a few halo properties (along with halo mass and Tidal Force (Fig. 2.9 Row 3)) that exhibit a clear monotonic relationship with with local density. That halos are more prolate at lower density may be because they form along thinner filaments at lower densities. We find that for low mass halos $X_{\rm off}$ is lowest in high density regions and highest in median density regions, indicating that halos tend to have more mass asymmetry in median density regions and less in high density regions. The decrease of $X_{\rm off}$ in higher density regions parallels that of prolateness, so lower mass halos are rounder and better centred at higher density, but the decrease of $X_{\rm off}$ at low densities implies that the increasingly prolate halos are also somewhat better centred at low density. The parallel behaviour of $X_{\rm off}$ and the half-mass scale factor ($a_{M_{1/2}}$, Fig. 2.9 Row 1) suggests a connection between $X_{\rm off}$ and the timing of halo formation in regions of different density. Note also the similar behaviour as a function of density of $X_{\rm off}$ and the spin parameters $\lambda_{\rm B}$ and $\lambda_{\rm P}$ (Fig. 2.6 Row 2 and Fig. A.8 Row 2).

density and $\lambda_{\rm P}$ is very similar (Fig. A.5 Row 2), though with slightly higher $\lambda_{\rm P}$ in high density regions compared to median density regions. We then focus our analysis on the following questions: (1) why do lower mass halos in high density regions typically have lower spin parameters compared to halos in median density regions; and (2) why do halos in low density regions typically have lower spin parameters than halos in median density regions?

One of the principal mechanisms for halos to acquire angular momentum is through mergers (e.g., Vitvitska et al., 2002). Understanding the variation in halo merger rate in regions of different density may be useful in explaining some of the dependence of spin parameter on local density. From the correlation between scale factor of the last major merger ($a_{\rm LMM}$) and local density, plotted in Fig. 2.9 Row 2, we see that halos in very low density regions last experienced a major merger at earlier times than halos in median density regions. This suggests that halos in low density regions may have lower spin parameters partly due to reduced frequency of major mergers at late times compared to halos in median density regions. However, halos in high density regions last experienced major mergers on very similar time-scales to halos in median density regions, indicating that differences in their spin parameter distributions must be a result of other mechanisms.

We now look at the time evolution of spin parameter for halos in different density regions at $z = 0$, plotted in Fig. 2.7 Row 2. Low mass halos in high density regions at $z = 0$ have only recently developed reduced spin parameters; in fact, before $z \sim 1$ these halos had typical spin parameters equal to or greater than the progenitors of halos in median density regions at $z = 0$. This reduction in spin parameter at late times for halos in high density regions appears coincident with the increase in concentration and reduction in accretion rate relative to halos in lower density regions, all of which likely stem from the relative increase in tidal forces

around this same epoch. On the other hand, halos in low density regions display consistently lower median spin parameters throughout their evolution than halos in higher density regions. This indicates that the lower spin parameters in low density regions originate early in the formation history of these halos. Halo formation in regions of lower local density may result in typically lower spin parameters due to reduced tidal torques (Peebles, 1969a; White, 1984; Porciani, Dekel & Hoffman, 2002) compared to halos forming in higher density regions. High mass halos display nearly constant median λ_B with redshift. We also show the time evolution of the Peebles spin parameter (Fig. A.6), which displays similar differences between halos in different density environments, but has a different overall redshift dependence than the Bullock spin parameter (Rodriguez-Puebla et al., 2016). We reiterate that median trends should not be confused with individual halo evolution. Spin parameters of individual halos can fluctuate considerably throughout their lifetimes due to accretion events and stripping.

In order to test the effect that halo stripping has on spin parameter, we plot in Fig. A.7 the correlation between spin parameter and local density, excluding halos that have lost more than 2% of their peak mass. While medians of spin parameter are determined using only un-stripped halos, we compute percentiles relative to all halos in order to make a fair comparison to the all-halo correlation (Fig. 2.6 Row 2). We see that in high density regions where stripping is most common, halos that are not appreciably stripped have higher spin parameters. This effect is most prominent for low mass halos, since higher mass halos are less likely to be strongly stripped. Thus, the downturn in spin parameter for low mass halos in high density regions is strongly correlated with these halos being stripped, a process that is much less frequent in lower density regions.

We've seen that many halos in high density regions evolved from regions of

lower density. The transition into very high density and high tidal force regions results in suppression of accretion rates and eventual stripping of material from the outer regions of many halos. Suppressed accretion rates are accompanied by decreased spin parameters, possibly as a result of halos preferentially losing eccentric, high angular momentum particles. Halos in low density regions have occupied low density regions for most of their evolution. We suggest that the underdense regions in which these halos formed exerted weaker tidal torques on collapsing protohalos, which effectively set the typical spin parameter of these halos. Spin parameter has high dispersion in all environments (Fig. A.4), and can vary widely over the lifetime of an individual halo due to sensitivity to accretion events such as major mergers. Nevertheless, low tidal torques exerted on halos throughout their lifetimes seems to be a plausible explanation for the lower spin parameters of low mass halos in low density regions at $z = 0$.

2.5.6 Prolateness

Finally, we take a look at how halo shape varies with environment density. We've defined a new halo shape parameter, *Prolateness*, defined as

$$P \equiv 1 - \frac{1}{\sqrt{2}} \left[\left(\frac{b}{a} \right)^2 + \left(\frac{c}{a} \right)^2 \right]^{1/2}, \tag{2.10}$$

such that $1 - P$ is the magnitude of the vector $(\frac{b}{a}, \frac{c}{a})$ normalized by $\frac{1}{\sqrt{2}}$, where a, b, and c are the lengths of the largest, second largest, and smallest triaxial ellipsoid axes, respectively, determined using the weighted inertia tensor method of Allgood et al. (2006). Prolateness ranges from 0 (perfect sphere) to 1 (maximally elongated, i.e. a needle), with most halos falling somewhere in the range of $0.2 - 0.6$.

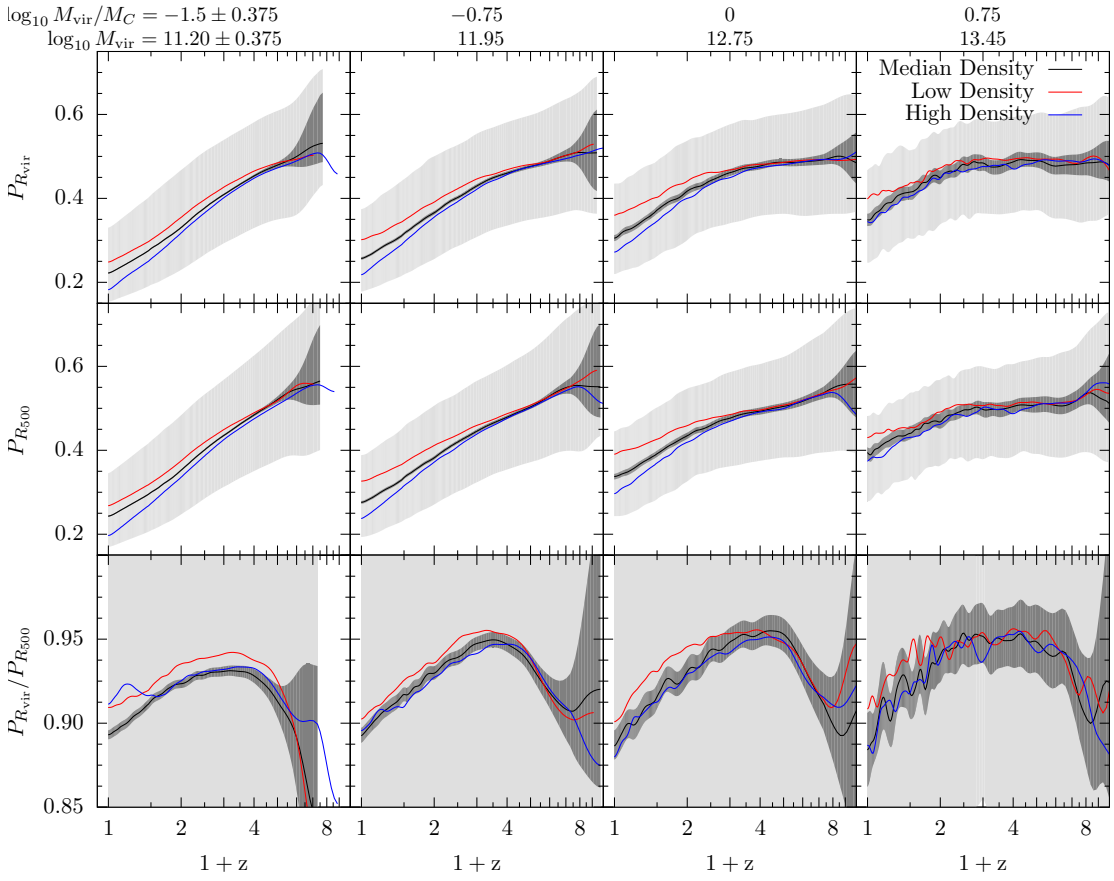

Figure 2.11: Same as Fig. 2.7, but showing prolateness measured at $R_{\rm vir}$ ($P_{R_{\rm vir}}$), prolateness measured at R_{500c} ($P_{R_{500c}}$), and the ratio of these two. We see that all halos are more prolate at high redshift, and become less prolate over time. Halos in high density regions at $z = 0$ tend to sphericalize more quickly than halos in low density regions, which tend to sphericalize the slowest. This is true for prolateness measured at both $R_{\rm vir}$ and R_{500c}. The ratio $P_{R_{\rm vir}}/P_{R_{500c}}$ tells us that since $z \lesssim 3$, the outer regions of halos become rounder more quickly than the inner regions. Additionally, lower mass halos in low density regions have the least change in shape from the inner ($P_{R_{500c}}$) to outer ($P_{R_{\rm vir}}$) regions since early in their formation history, while halos in median and high density regions at $z = 0$ show a greater disparity between inner and outer shape throughout most of their evolution.

We see from Fig. 2.10 Rows 1 and 2 that prolateness measured at both $R_{\rm vir}$ and R_{500c} (where $R_{500c}/R_{\rm vir}$ is typically about 0.7) decreases monotonically with increasing density. Halos in low density regions are more prolate and halos in high density regions are less prolate. Interestingly, this is true for all of the mass bins we present, suggesting that a universal phenomenon underlies this relationship. We attribute the rounder halos in high density regions partly to stripping by massive neighbours. Tidal stripping would tend to preferentially remove loosely bound particles with more elliptical orbits, resulting in rounder halos. However, we would expect this to more dramatically affect $P_{R_{\rm vir}}$ than $P_{R_{500c}}$, which does not seem to be the case. $P_{R_{500c}}$ is equally, if not slightly more correlated with density than $P_{R_{\rm vir}}$, especially in high density regions. This suggests a more general phenomenon may govern the evolution of halo prolateness, such as accretion geometry. Total accretion rate (Fig. 2.6 Row 3) displays a similar relationship as prolateness from median to high density regions, but is largely flat for halos in regions below median density. We expect then, that prolate halos in low density regions differ from rounder halos in higher density regions by the nature of how they accrete material, but not their total accretion rate. For example, halos in low density regions may accrete a larger fraction of material along a preferred axis, or reside in thinner filaments, compared to halos in median density regions, which would tend to build prolate halos (e.g., Allgood et al., 2006; Vera-Ciro et al., 2011; Despali, Giocoli & Tormen, 2014; Despali et al., 2016). Halos in high density regions may be rounder due to a combination of more isotropic accretion of material, and tidal stripping of material with highly eccentric orbits. Altogether, these trends pose one primary question for clarification: is there a single underlying mechanism that drives the relationship between local density and halo prolateness?

Looking at the evolution of halo prolateness for halos that end up in different

density regions at $z = 0$ (Fig. 2.11), we see that all halos grow less prolate with time, but those in higher density regions do so more rapidly than those in lower density regions. This is true for prolateness measured at both $R_{\rm vir}$ and R_{500c}, and for $M_{\rm vir} \lesssim M_{\rm C}$. We note that shapes of halos in high density regions at $z = 0$ begin to diverge from those in median density regions around redshift ($z \sim 1.5$), which is roughly when these halos begin to experience dramatically higher tidal forces (see Fig. 2.8 Row 1). Low mass halos in low density regions begin to sphericalize at a slower rate than halos in median density regions early in their evolution ($z \sim 2.5$). Overall, we observe a gradual divergence in sphericalization rate between halos in high density regions and those in low density regions, starting around $z \sim 1.5-2.5$ for halos less massive than the critical mass $M_{\rm C}$. This contrasts with certain other halo properties, such as $C_{\rm NFW}$ and $\lambda_{\rm B}$, where we see sharp deviations at late times for halos that end up in high density regions. Since we expect tidal stripping to be chiefly responsible for these sharp trends in $C_{\rm NFW}$ and $\lambda_{\rm B}$, the absence of dramatic differences in prolateness at late times suggests tidal stripping may not be the main underlying reason for halos rounding out most rapidly in high density regions.

In Fig. 2.11 Row 3, we plot the evolution of the ratio of prolateness measured at $R_{\rm vir}$ to prolateness measured at R_{500c}. This gives us a sense for how the shape of the inner region of the halo is changing relative to the outer region. The ratio $R_{\rm vir}/R_{500c}$ is less than unity; it is well known (e.g., Allgood et al., 2006) that halos are somewhat more prolate at smaller radii. In general, we see that the outer regions of halos tend to sphericalize more rapidly than the inner regions (at least, for $z \lesssim 4$). For low mass halos, we see that those in low density regions have less difference between their inner and outer shapes for most of their history compared to those in higher density regions. The slight bump that halos moving into high

density regions experience at late times ($z \sim 0.25$) indicates a rapid "inside-out" rounding – initially their inner regions, followed by subsequent rounding of the outer regions. We expect this phenomenon to be related to harassment by more massive halos and tidal stripping.

Overall, we find that halos in high density regions at $z = 0$ are rounder than those in low density regions, but have a greater difference between their inner (more prolate) and outer (less prolate) shapes. We expect that the nature of the accretion rate of halos (including where they are located in the cosmic web) underlies these differences, but that tidal stripping from massive halos in high density regions also plays a part in modulating halo shape.

2.6 Discussion and Conclusions

We investigate how properties of distinct dark matter halos in the Bolshoi-Planck simulation depend on the density of their surrounding environment. We determine local densities using a CIC method of counting particles on a 1024^3 grid and then smoothing with a Gaussian kernel with several different smoothing radii. In §2.3, we plot distributions of cosmic densities and find that they are well fit by a Generalized Extreme Value Distribution. We find that at smaller smoothing scales, the density distributions peak at lower densities and sample more non-linear structure (voids) than larger smoothing scales, which peak closer to the average density of the simulation and span a narrower total range of densities.

In §2.4, we present halo mass functions in different density regions for $z = 0$, 0.5, 1, and 2. We find that mass functions in lower density regions have lower characteristic masses than in higher density regions. The mass functions extend to higher masses and have higher characteristic masses at low redshift, especially in high density regions, but otherwise evolve little from z = 2 to z = 0.

§5 begins by summarizing correlations between various halo properties and the environmental density around the halo, and the redshift evolution of halo properties at different densities. In §2.5.3 through §2.5.6, we present results on how halo mass accretion rate ($\dot{M}_{\tau_{\rm dyn}}/M$), NFW concentration ($C_{\rm NFW}$), spin parameter ($\lambda_{\rm B}$), and shape ($P$) depend on the local density smoothed on several length scales around the halos. For each halo mass range we choose a characteristic smoothing scale that is at least 8 times greater than the typical virial radii of the halos, allowing us to capture local effects that are lost when smoothing on larger scales, while not being too influenced by the halos' own density profiles. In Fig. 2.5 we plot the relationship between local density and $C_{\rm NFW}$, $\lambda_{\rm B}$, and specific accretion rate, which we plot again but in percentilized form in Fig. 2.6. We find that low mass halos ($M_{\rm vir} < M_{\rm C}$) in high density regions accrete significantly less than halos in lower density regions. The median accretion rate in the highest density regions even drops below zero, indicating that a majority of low mass halos in very high density regions are losing mass due to being tidally stripped by nearby massive neighbours. Halos in low density regions accrete at similar rates as those in median density regions. Higher mass halos have a less dramatic drop in accretion rate in high density regions for two reasons:

1. The highest mass halos are the ones stripping the lower mass halos, and so should have high accretion rates, unless they are in the vicinity of an even more massive halo. Also, massive halos tend to be physically separated from other massive halos, making them less likely to be stripped.

2. High mass halos occupy exclusively high density regions. Any trends observed will then only span a narrow range of densities, and be limited in dynamic range as a result.

These points (lack of stripping and narrow range of mostly higher than average

densities) account for the main differences between halos below $M_{\rm C}$ and above $M_{\rm C}$ for most of the halo property–density relations we observe.

Maulbetsch et al. (2007) found that halos of the same final mass accreted their mass earlier in denser environments, and also accreted a significantly higher fraction of their mass in major mergers. We have not investigated the fraction of mass accreted in major mergers in this work, but do find that halos accreted their mass earlier in high density regions. Since halos in high density regions have suppressed accretion rates at $z = 0$, their progenitors must be more massive than the progenitors of halos in lower density regions, and thus will have formed earlier on average. Since the total accretion rate of halos in low density regions is similar to halos in median density regions, we expect that the fraction of mass accreted in mergers may play a role in differentiating halo properties in low and median density regions.

In §2.5.4, we find that low mass halos in high density regions have dramatically higher NFW concentrations than halos in lower density regions. This trend has been well established in the literature (e.g., Bullock et al., 2001; Avila-Reese et al., 2005; Macciò et al., 2007), and is primarily caused by tidal stripping. This tends to remove material from the outer regions of halos, resulting in steeper outer profiles, poorer NFW fits, and hence artificially reduced scale radii and raised NFW concentrations. We find that the minimum median concentration varies with local density, and is in lower density regions for lower mass halos. In the lowest mass bin ($M_{\rm vir} = 10^{11.2}{\rm M}_{\odot}$), halos in the lowest density regions have concentrations about 30% higher (about 10% difference in percentile) than the minimum median concentration, which is around the 20th percentile in local density. We find a corresponding decrease in half-mass scale factor (earlier formation time) in low density regions, and also see that halos in low density regions have had a

consistently elevated median concentration compared to halos in median density regions. This suggests that the halos in the lowest density regions formed earlier on average and have had more time to grow their concentrations than halos in somewhat higher density regions.

We find that the spin parameter (§2.5.5) is about 30% lower in the lowest density regions than in median density regions for all halo masses. Furthermore, halos in the lowest density regions have had consistently lower spins (Fig. 2.7), and experienced consistently lower tidal forces (Fig. 2.8) throughout their evolution. The magnitude of this effect is similar to that of the increase in concentration in the lowest density regions, and so may be related to differences in the nature of the accretion histories of halos in different density regions (amount of material accreted in lumps, etc.). The systematic offset in median spin parameter is a reflection of the lower tidal torques exerted on halos in low density regions throughout their evolution. We therefore expect that low mass halos with lower spins in low density regions would tend to host rotationally supported galaxies with less extended disks, and possibly also smaller early-type galaxies as well (e.g., Kravtsov, 2013). This could be observationally tested by comparing galaxy sizes and morphologies at the same stellar mass in low and median density regions.

In high density regions, we find that low mass halos have reduced spin parameters and high mass halos have increased spin parameters compared to halos in median density regions. Low mass halos tend to be heavily stripped in high density regions at $z \sim 0$ (Fig. 2.5). We expect that tidal stripping preferentially removes the high angular momentum particles from the outer regions of halos, reducing their spin parameters. This role of tidal stripping in suppressing spin parameter is supported in Figs A.7 and A.8, where we see that low mass halos that have not been appreciably stripped do not have lower spin parameters in high density

regions than in median density regions. Because this stripping occurs mainly at low redshift, after most galaxy formation has ended in central galaxies in low mass halos in dense regions, we do not expect that it will affect the sizes of these galaxies. Wang et al. (2011a) found that halos in higher tidal field environments and in higher density environments (smoothed in spheres of radius 6 h^{-1}Mpc) have higher spins, with the trends stronger for higher mass halos. This is consistent with our results for halo masses $\gtrsim M_{\rm C}$. We would expect to see some downturn in spin in high density regions for their lowest mass bin ($M_{\rm vir} = 10^{12} - 10^{12.5}$ M$_\odot$), but this would be a quite small effect and is likely within the statistical error of the analysis. We see stronger suppression of spin in high density regions for lower masses (and smaller smoothing scales) than studied by Wang et al. (2011a).

We find in §2.5.6 that halo prolateness is monotonically dependent on density. Halos in the lowest density regions are typically the most elongated at both $R_{\rm vir}$ and R_{500c}, become rounder at the slowest rate, and have the least change between inner (R_{500c}) and outer ($R_{\rm vir}$) shape throughout their evolution. Halos in the highest density regions are the roundest at both radii measured and sphericalize the most rapidly, but have a relative change between inner and outer shape consistent with halos in median density regions. We also see that more massive halos tend to be more elongated at a given redshift, and have less relative change between inner and outer shape than lower mass halos. These results are largely consistent with other works that have studied how halo shape varies with radius (or overdensity within the halo) and evolves over time (e.g., Allgood et al., 2006; Vera-Ciro et al., 2011; Despali, Giocoli & Tormen, 2014; Despali et al., 2016), which find that the shape of a shell at a given overdensity reflects the nature of the accretion at the epoch when that shell primarily assembled. Early in their evolution, halos tend to build elongated shells due to highly directional accretion

along narrow filaments in lower density regions. As their host filaments grow thicker, they experience more isotropic merging and overall suppressed accretion of fast moving material and tend to build more spherical shells in higher density regions (see, e.g. Borzyszkowski et al., 2016). In future work, we intend to further investigate how halo properties correlate with their location in the cosmic web.

The results we present in this paper are consistent with Avila-Reese et al. (2005), which found that halos in cluster environments had lower spin parameters, higher concentrations, and are more round than halos in the field. Macciò et al. (2007) found that higher-concentration low-mass halos are found in denser environments, and lower-concentration ones in less dense environments, which helps to explain assembly bias, i.e. that higher-concentration early-accreting halos with mass $M_{\rm vir} < M_{\rm C}$ are more clustered (Gao, Springel & White, 2005; Gao & White, 2007; Wechsler et al., 2006). However, they found only a weak dependence of mean axis ratio on environment (with high density regions having slightly rounder halos), and no significant difference in spin parameter in different density regions. This is not inconsistent with our results, but highlights the necessity for better statistics to adequately constrain trends in regions of extreme high and low density, especially for high dispersion halo properties like spin parameter.

Chapter 3

Halo Mass Loss

3.1 Background

In the modern ΛCDM standard cosmological paradigm, galaxies form and evolve within dark matter halos (reviewed in Frenk & White, 2012; Primack, 2012). Determining the evolving properties of the halos is therefore important for understanding the formation of galaxies in the expanding universe. Ever since simulations were first able to resolve dark matter halos (e.g., Navarro, Frenk & White, 1996) there have been studies of the abundance and other properties of the halos—for example, from the Millennium Simulations (Bett et al., 2007, 2010; Ludlow et al., 2013), the first large high-resolution cosmological simulations. Other simulations have been used to investigate how halo properties are affected by their environments (e.g., Hahn et al., 2007b,a; Wang et al., 2011b; Paranjape, Hahn & Sheth, 2018, and papers cited there) and by their mass assembly histories (e.g., Wong & Taylor, 2012). Here we use analysis of halo properties in new large cosmological simulations based on the Planck (Planck Collaboration et al., 2014b, 2016) cosmological parameters, the Bolshoi-Planck and MultiDark-Planck simulations (Klypin et al., 2016b; Rodríguez-Puebla et al., 2016, and references therein).

The general expectation has been that dark matter halos typically grow in mass with cosmic time, for example with the mass at any redshift z approximately given by $M(z) = M(0)\exp(-\alpha z)$, where $\alpha \sim 0.8$ is fit to individual halo growth trajectories (e.g. Wechsler et al., 2002b; Dekel et al., 2013; Rodríguez-Puebla et al., 2016, 2017, and references therein). However, Lee et al. (2017) showed that in regions of high dark matter density, most low-mass halos are actually losing mass due to tidal stripping. But although some halos lose rather than gain mass, until the present paper there has not been any detailed investigation of the causes and consequences of halo mass loss. As we will show, there are two main causes of halo mass loss: relaxation after major mergers and tidal stripping.

After a halo major merger (i.e., with the merging halos having mass ratio greater than 0.3 to 1), the virial ratio of the kinetic and potential energies $T/|U|$ of the resulting halo is often initially considerably larger than the virial value 0.5. As the halo relaxes toward virial equilibrium, a small fraction of its mass, typically $\sim$10%, moves beyond the virial radius. This includes a large fraction of the higher angular momentum material, and as a consequence the halo spin parameter λ decreases, as shown by D'Onghia & Navarro (2007). An example of halo mass loss after a major merger was demonstrated and briefly discussed in Behroozi et al. (2015, Section 5.2), and the phenomenon was also mentioned in Behroozi, Loeb & Wechsler (2013). As we will see, this post-merger mass loss phenomenon is rather common.

Tidal stripping of subhalos has been extensively discussed in the literature (e.g. van den Bosch, 2017, and refererences therein), but here we concentrate on distinct halos. Tidal stripping of distinct dark matter halos that are close to (or pass through) more massive halos has been discussed in the literature Hahn et al. (2009b); Behroozi, Loeb & Wechsler (2013); Behroozi et al. (2014); Hearin,

Behroozi & van den Bosch (2016). It can lead to more than 10% mass loss, sometimes much more. This affects only a relatively small fraction of the halos except in dense regions, where most halos with mass $\lesssim 10^{12} M_\odot$ suffer significant mass loss.

Interestingly, the effects of these two halo mass loss mechanisms are nearly orthogonal. As we will show, halos suffering mass loss after a major merger typically have lower concentration and higher spin and prolateness than average, while halos that are significantly tidally stripped have higher concentration and lower spin and prolateness.

For a study like ours, it is essential to use the analysis of a large simulation for which all halos have been found at many time steps and the merger history of each halo has been determined. Inevitably, the results of the study of halo properties and their evolution reported here depends on the halo definition used. Here for the halo mass and radius we use the virial definition (see, e.g., Rodríguez-Puebla et al., 2016). The halo concentrations, spins, and other halo properties would be different if we had used another halo definition (though it is straightforward to map one concentration definition to another, once the associated halo profiles are specified). It would certainly be useful to compare the results reported here with those that follow from other halo property definitions, when such results become available.

This paper is organized as follows. In §2 we discuss the simulations and methods used, including definitions of key concepts that we use, including tidal force TF, halo concentration $C_{\rm NFW}$, and prolateness P. §3 discusses the frequency, causes, and consequences of mass loss, with §3.1 emphasizing halos mass loss after major mergers and §3.2 focussing on tidal stripping. We recommend that readers skip ahead to Figures 13 and 14, which show typical behaviours of many

halo properties after major mergers and after tidal stripping. §4 presents our Discussion and Conclusions.

3.2 Simulations and Method

In this paper we study the halos in the Bolshoi-Planck simulation (Klypin et al., 2016b; Rodríguez-Puebla et al., 2016), which have been analyzed using the ROCKSTAR halo finder (Behroozi, Wechsler & Wu, 2013) and the CONSISTENT TREES formalism (Behroozi et al., 2013b) for constructing halo merger trees. The cosmological parameters for the Bolshoi-Planck simulation were $\Omega_{\Lambda,0} = 0.693, \Omega_{\rm M,0} = 0.307, \Omega_{\rm B,0} = 0.048, h = 0.678, n_s = 0.96$ and $\sigma_8 = 0.823$. The halo masses studied are given by

$$M_{\rm vir} = \frac{4\pi}{3}\Delta_{\rm vir}\rho_{\rm m}R_{\rm vir}^3, \tag{3.1}$$

where $\Delta_{\rm vir}$ is given by the Bryan & Norman (1998) fitting formula $\Delta_{\rm vir}(z) = (18\pi^2 + 82x - 39x^2)/\Omega(z)$, where $\Omega(z)$ is the ratio of mean matter density $\rho_{\rm m}$ to critical density $\rho_{\rm c}$ at redshift z, and $x \equiv \Omega(z) - 1$. Using other halo mass definitions (e.g., splashback radius More, Diemer & Kravtsov, 2015) and/or other halo finders would lead to different results (e.g. Behroozi et al., 2015), but we do not consider such alternatives in this paper since doing so would require reanalysis of the many timesteps of a large simulation.

The outputs from the 178 saved timesteps of the Bolshoi-Planck simulation analyzed by ROCKSTAR are discussed in Rodríguez-Puebla et al. (2016, especially the Appendices), and they can be downloaded from the UCSC Hyades astronomical computer system.[1] Here we summarize the definitions of the halo properties that we study in this paper.

[1] `http://hipacc.ucsc.edu/Bolshoi/MergerTrees.html`

- NFW concentration $C_{\rm NFW}$ is defined as

$$C_{\rm NFW} = \frac{R_{\rm vir}}{R_s}, \tag{3.2}$$

where the Navarro, Frenk & White (1996, NFW) profile is given by

$$\rho_{\rm NFW}(r) = \frac{4\rho_s}{(r/R_s)(1+r/R_s)^2}. \tag{3.3}$$

The scale radius R_s is the radius where the logarithmic slope of the density profile is -2. The NFW profile is completely characterized by two parameters, for example ρ_s and R_s, or alternatively the halo mass $M_{\rm vir}$ and concentration parameter $c_{\rm vir}$.

- Maximum circular velocity $V_{\rm max}$ is the maximum of $[GM(<r)/r]^{1/2}$ at any radius $r < R_{\rm vir}$, where $M(<r)$ is the mass enclosed by spherical radius r.

- Bullock spin parameter $\lambda_{\rm B}$ is defined following Bullock et al. (2001) as

$$\lambda_{\rm B} = \frac{J}{\sqrt{2}M_{\rm vir}V_{\rm vir}R_{\rm vir}}, \tag{3.4}$$

The distribution and redshift dependence of $\lambda_{\rm B}$ is discussed in Rodríguez-Puebla et al. (2016) and Somerville et al. (2018, Appendix B) and compared with that of the Peebles (1969b) spin parameter

$$\lambda_{\rm P} = \frac{J|E|^{1/2}}{GM_{\rm vir}^{5/2}}, \tag{3.5}$$

where J and E are the total angular momentum and the total energy of a halo of mass $M_{\rm vir}$.

- Scale factor of the last major merger $a_{\rm LMM}$ is the scale factor $a = (1+z)^{-1}$

of the most recent merger with halo mass ratio greater than 0.3 to 1 along the halo's largest progenitor track.

- Tidal Force (TF) experienced by a halo is calculated as the strongest tidal force from any nearby halo, in dimensionless units ($R_{\rm halo}/R_{\rm Hill}$). The Hill radius (see, e.g., Hahn et al., 2009b; Hearin, Behroozi & van den Bosch, 2016) is the radius within which material can remain gravitationally bound to a secondary halo. It is given by $R_{\rm Hill} = D(M_{\rm sec}/3M_{\rm prim})^{1/3} = R_{\rm sec}(D/3^{1/3}R_{\rm prim})$, where the primary (secondary) halo is the larger-virial-radius (smaller-virial-radius) halo of a pair whose centers are separated by distance D.

- Prolateness is defined as

$$P \equiv 1 - \frac{1}{\sqrt{2}}\left[\left(\frac{b}{a}\right)^2 + \left(\frac{c}{a}\right)^2\right]^{1/2}, \tag{3.6}$$

  such that $1-P$ is the magnitude of the vector $(\frac{b}{a}, \frac{c}{a})$ normalized by $\frac{1}{\sqrt{2}}$, where a, b, and c are the lengths of the largest, second largest, and smallest triaxial ellipsoid axes, respectively. Prolateness ranges from 0 (perfect sphere) to 1 (maximally elongated, i.e. a needle), with most halos falling somewhere in the range of $0.2-0.6$. We will plot the Prolateness of halos both within the virial radius $R_{\rm vir}$ and the radius R_{500c} enclosing average density 500 times critical density $\rho_c = 3H^2/(8\pi G)$, where $H = \dot{a}/a$ is the Hubble parameter.

- $X_{\rm off}$ is the offset of the density peak of a halo from its center of mass within $R_{\rm vir}$, in units of h^{-1} kpc.

- $D_{\rm off} = X_{\rm off}/R_{\rm vir}$.

- Virial ratio $T/|U|$ is the ratio of kinetic energy T to potential energy $|U|$. According to the virial theorem, a fully relaxed halo has $T/|U| = 0.5$.

- Environmental density ρ_σ is the local environment density smoothed on different scales (σ) and $\rho_{\rm avg}$ is the average density of the simulation. (See (Lee et al., 2017) for details.)

As in Lee et al. (2017), in this paper we will plot halos in four mass bins, corresponding to $\log_{10} M_{\rm vir}/(h^{-1}M_\odot) = 11.2 \pm 0.375$, 11.95 ± 0.375, 12.7 ± 0.375, and 13.45 ± 0.375. The lowest mass $z = 0$ halos in our analysis still contain roughly ~ 450 particles to minimize noise introduced from low particle counts. As shown in Rodríguez-Puebla et al. (2016), $M_{\rm vir} = 10^{12.7}h^{-1}M_\odot$ is the mass of 1σ fluctuations just collapsing at $z = 0$, and the other mass bins are separated by $10^{0.75}h^{-1}M_\odot$. As in Lee et al. (2017), we quote the environmental density ρ_σ smoothed at 1 h^{-1}Mpc for halos in the lowest mass bin, 2 h^{-1}Mpc in the next mass bin, 4 h^{-1}Mpc in the next mass bin, and 8 h^{-1}Mpc in the highest mass bin; these radii are large enough that the central halo has little effect on the density.

3.3 How mass loss affects halo properties

We first motivate our analysis of mass loss mechanisms and how they affect halo properties by looking at how common mass loss is among distinct halos at $z = 0$. In Fig. 3.1, we plot the cumulative distribution of the mass loss fraction ($M_{\rm vir}/M_{\rm peak}$), which describes how much of a halos' maximum mass remains at $z = 0$. For many halos this fraction is 1 (or, their maximum mass is their current mass). We will consider halos to be "diminished" when they have experienced mass loss. Halos that have lost more than 5% of their mass since their peak mass are appreciably diminished. We will generally consider halos that have lost less than 5% of their mass since their peak mass to belong to the group of undiminished – or normal – halos. This distinction between diminshed and normal halos is provided

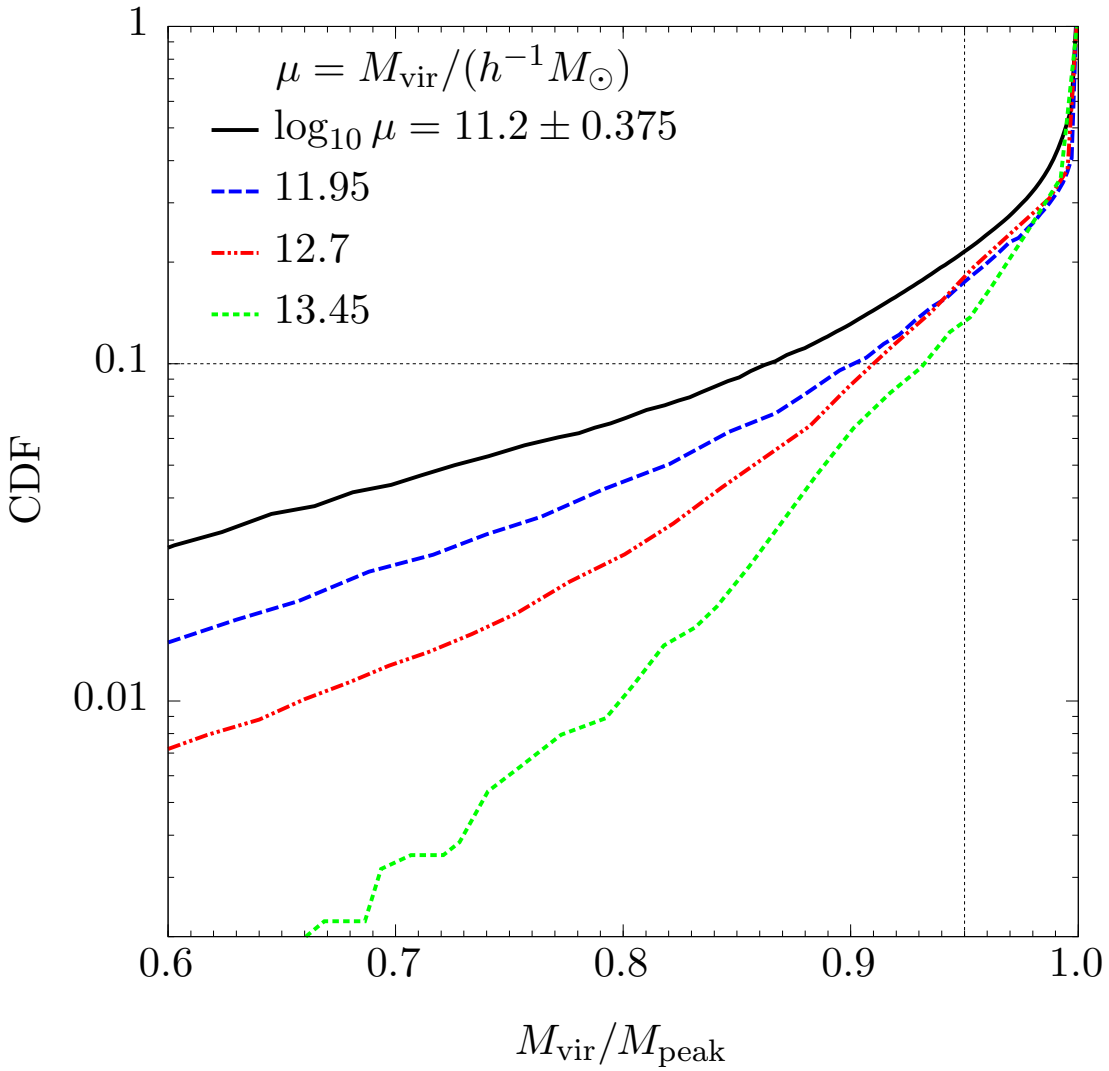

Figure 3.1: Cumulative distribution function of mass loss fraction for distinct halos. We divide our halos into 4 mass bins of width $\Delta \log_{10} \mu = 0.75$. Lower mass halos have typically lost more mass than higher mass halos. The fraction of halos that have experienced appreciable mass loss (greater than 5% since their peak mass) ranges from roughly 12% (highest mass bin) to 22% (lowest mass bin). Roughly 5% of low mass halos have experienced dramatic mass loss ($> 30\%$ since $M_{\rm peak}$), while very few high mass halos have.

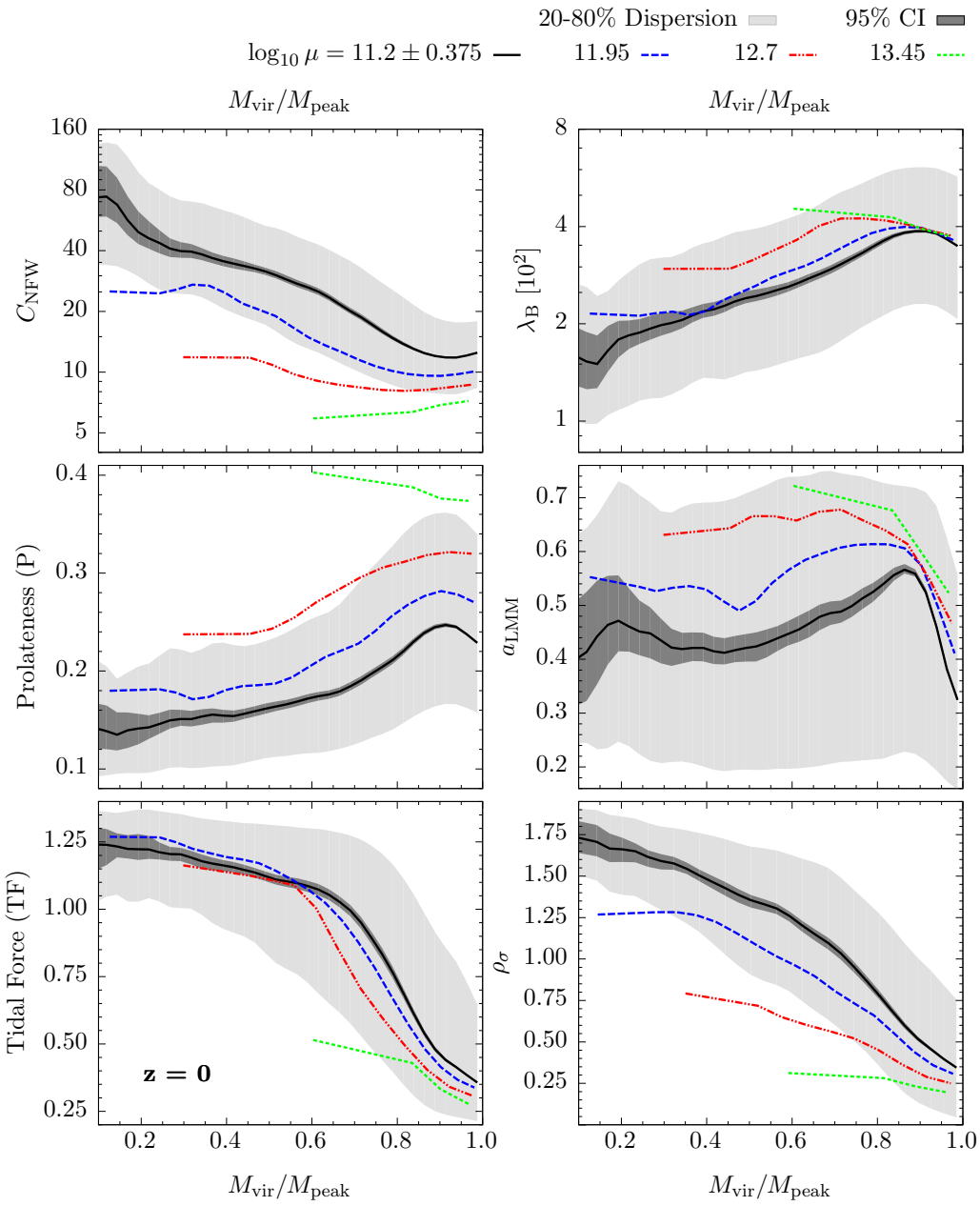

Figure 3.2: Median $z = 0$ relations between mass loss fraction and NFW concentration ($C_{\rm NFW}$), Bullock spin parameter ($\lambda_{\rm B}$), prolateness (P), scale factor of last major merger ($a_{\rm LMM}$), tidal force (TF), and local density (ρ_σ). We use the same mass bin definitions as in Fig. 3.1. We include only distinct halos. Light grey shading reflects the 20-80th percentile dispersion, while dark grey shading indicates the 95% confidence interval on the median, shown only for the lowest mass bin. Halos that have lost a small amount of mass ($5 - 15\%$ for low mass halos) tend to have lower concentrations, higher spin parameters, and are more prolate compared to halos that have not lost mass. Conversely, halos that have experienced more dramatic mass loss ($> 20\%$ for low mass halos) display the opposite behaviour: they have lower concentrations, lower spin parameters, and are more spherical compared to halos that have not lost mass. Additionally, halos that have lost a small amount of mass are much more likely to have experienced a recent major merger, while halos that have experienced dramatic mass loss tend to experience higher tidal forces and live in significantly higher density regions than

by the vertical dotted black line in Fig. 3.1. We see that the lowest mass bin is composed of roughly 22% diminished halos, while the highest mass bin contains about 12%. We haven't yet established at what degree of mass loss other halo properties are noticeably affected, but clearly a significant fraction of halos are potentially subject to these effects. An additional point to establish is that mass loss is more common for lower mass halos. High mass halos rarely experience dramatic mass loss, while roughly 5% of low mass halos have lost more than 30% of their mass since their peak mass.

To begin understanding how mass loss affects other halo properties, we plot in Fig 3.2 relations between the mass loss fraction ($M_{\rm vir}/M_{\rm peak}$) and several halo properties. Each panel presents medians of the given relation for each of the four halo mass bins (we use the same four mass bins throughout this analysis). For the lowest mass halos we show the $20-80\%$ dispersion with light grey shading and the 95% confidence interval on the median in dark grey shading. Higher mass halos may have similar dispersions, but will have wider confidence intervals (not shown) due to having fewer halos. High mass halos also do not extend to very low values of $M_{\rm vir}/M_{\rm peak}$ since they rarely lose more than about 30% of their peak mass. We observe similar trends in spin parameter, prolateness, and (inverted) concentration as a function of mass loss fraction. In each of these properties we identify a change in one direction coincident with a moderate amount of mass loss, along with a change in the opposite direction for heavily diminished halos. For halos in the lowest mass bin this turnaround occurs at a mass loss level of roughly 10% $M_{\rm peak}$; for higher mass halos the turnaround is more gradual and shifted towards higher levels of mass loss. Overall, we see that low mass halos that have lost between $5-15\%$ $M_{\rm peak}$ have lower concentrations, higher spin parameters, and are more prolate than normal halos, while those that have lost more than

15% $M_{\rm peak}$ have increasingly higher concentrations, lower spin parameters, and are more spherical than normal halos.

Looking at the remaining panels of Fig. 3.2, we see that moderately diminished halos are far more likely to have had a recent major merger than normal halos. At least for low mass halos, there is a strong peak in the typical $a_{\rm LMM}$ coincident with a mass loss of about 15% $M_{\rm peak}$, while normal halos experienced very few recent major mergers. This suggests that merging history may play an important role in influencing these halo properties, especially in the moderate mass loss regime, where we observe the strongest correlation with $a_{\rm LMM}$.

Finally, in the bottom two panels of Fig. 3.2, we show the relations between tidal force, local density and mass loss fraction. We see a monotonic relationship with mass loss fraction in both cases and for all mass bins. Halos that have lost more mass tend to be experiencing stronger tidal forces and are found in higher density regions than those that have lost less mass. We note that the tidal force we've used is an approximation of the true tidal force, since for each halo we consider only the force from the single most tidally influential nearby halo. The local density, however, is computed by smoothing the particle data from the simulation, providing an accurate indication of the density of the surrounding environment. We expect that the plateauing of the tidal force for halos that have lost more that about 40% $M_{\rm peak}$ is an artifact of our approximation method, and that the true tidal force would scale more linearly with mass loss fraction, as does the local density.

Given these relationships between the intensity of halo mass loss and other halo properties, we found it natural to propose two distinct mass loss mechanisms:

1. mass loss due to relaxation after a recent major merger, and

2. mass loss due to tidal stripping in very high density environments.

These two mechanisms are not exclusive, and in (somewhat rare) cases can both be contributing to mass loss simultaneously. To quantify these processes, we divide all halos in each mass bin into one of four groups, labelled as follows:

- Tidal Stripping (TS): potentially subject to tidal stripping (has experienced tidal force > 1 since $M_{\rm peak}$), but has **not** experienced mass loss from a recent major merger ($a_{\rm LMM} < 0.45$);
- Relaxation (R): **not** subject to tidal stripping, but potentially subject to mass loss during the relaxation period following a recent major merger ($a_{\rm LMM} > 0.45$);
- Tidal Stripping + Relaxation (TS+R): potentially subject to **both** tidal stripping and relaxation mass loss following a recent major merger;
- Neither (N): does not satisfy conditions for either mass loss mechanism.

Note that we have not yet imposed any selections based on mass loss directly. Each of these groups contain halos that cover a broad range of mass loss levels, including zero mass loss. In certain subsequent figures, we'll specifically select diminished halos (those that have lost $> 5\%$ of their peak mass) from these groups to emphasize the effects of each mass loss mechanism.

In Fig. 3.3, we show a visual representation of how these groups are organized (with shape areas representative of the mass bin centred on $\log_{10} M_{\rm vir}/{\rm M}_\odot = 11.2$); additionally, in Fig. 3.4 we show how many diminished halos fall into each of these groups for each of the four mass bins in our analysis. We find that low mass halos are the most likely to be potentially subject to tidal stripping alone (about 23% of halos in our lowest mass bin are in group TS compared to only about 2% of halos in the highest mass bin). However, high mass halos are more commonly subject to major merger induced mass loss (about 67% of halos in our highest mass bin

are in group R compared to only about 39% of low mass halos). Few halos are potentially subject to both mass loss mechanisms (group TS+R), with the total ranging from 15% of low mass halos to only 7% of high mass halos. The combined fraction of halos that are potentially subject to these two mass loss mechanisms (groups R, TS, and TS+R) is about 77% for all mass bins.

3.3.1 Post-Merger Relaxation and Mass Loss

The most common mass loss mechanism for dark matter halos is the shedding of excess high energy material in the aftermath of a halo merger event. From Fig. 3.4 we can see that halos with a recent major merger but no recent history of high tidal force (group R) are by far the most common group of mass loss candidates. In Fig. 3.5, we show the cumulative distribution functions of the mass loss ratio for all halos in groups N, TS, and R to highlight the distribution of diminished halos among those that, respectively, do not appear to be influenced by tidal or post-merger mass loss, are susceptible to tidal stripping exclusively, and are susceptible to post-merger mass loss exclusively. We additionally plot in the right column the minimum mass loss fraction since the peak mass for halos in groups N and TS and since the scale factor of the last major merger for halos in group R. We see that about 6% (low mass) – 8% (high mass) of group N halos have lost more than 5% of their peak mass at $z = 0$, a much lower fraction than the $12 - 22\%$ of all halos (Fig. 3.1). Essentially no group N halos have lost more than 20% of their peak mass. Clearly, removing halos associated with possible mass loss mechanisms (groups TS, R, and TS+R) also removes the majority of diminished halos, leaving only a small percentage of weakly diminished halos. The small number of remaining group N halos experienced mass loss either due to a third mechanism, or due to weaker manifestations of tidal stripping (with tidal

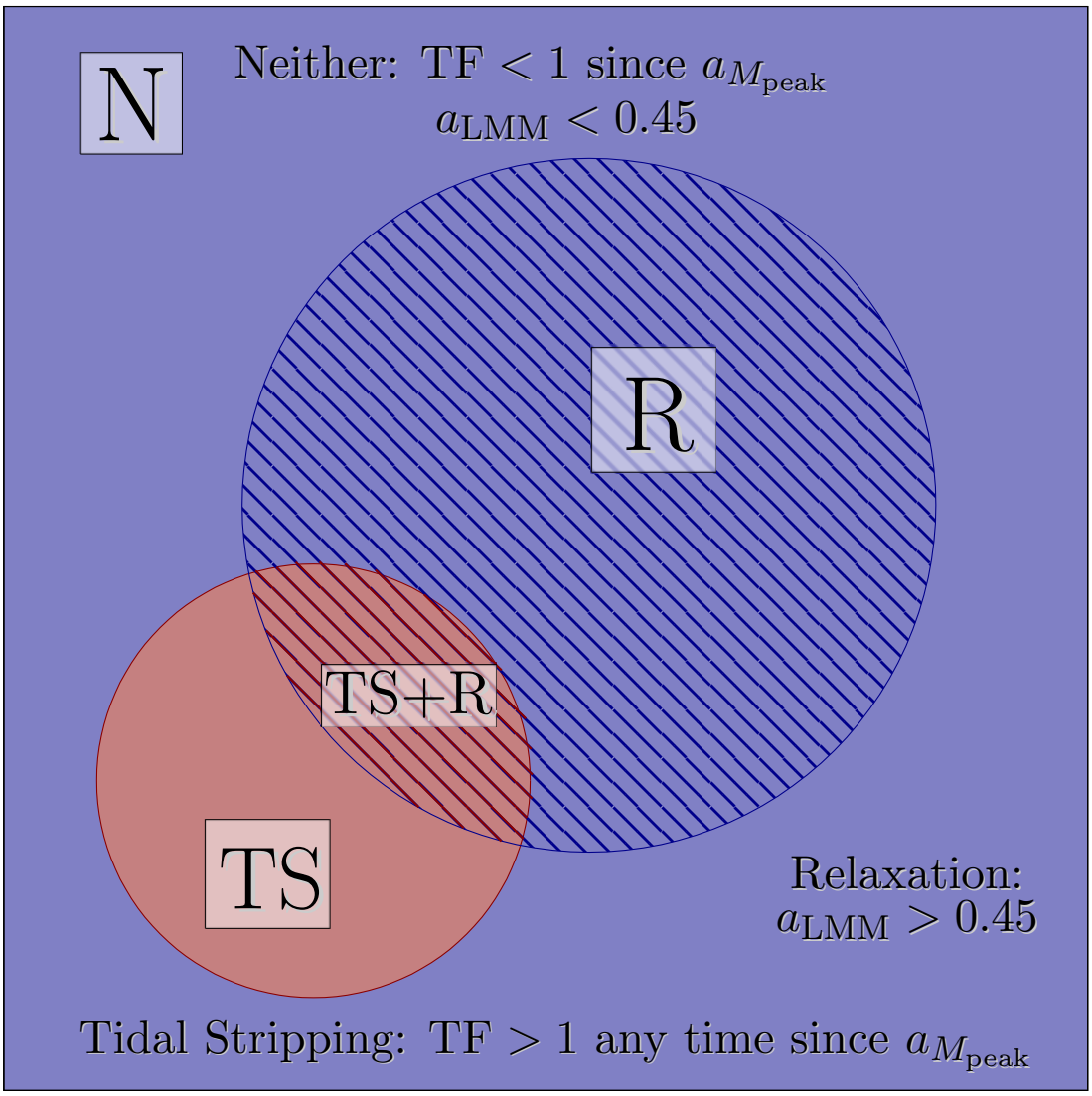

Figure 3.3: We present a visual representation of the four mass loss group labels we use in this analysis. All halos in each mass bin are assigned to one of these groups according to their tidal force and major merger history. TS (tidal stripping) halos are subject to tidal stripping only, R (relaxation) halos are subject to post major merger mass loss only, TS+R halos are subject to both tidal stripping and post-merger mass loss, and N (neither) halos do not satisfy the conditions for either mass loss mechanism.

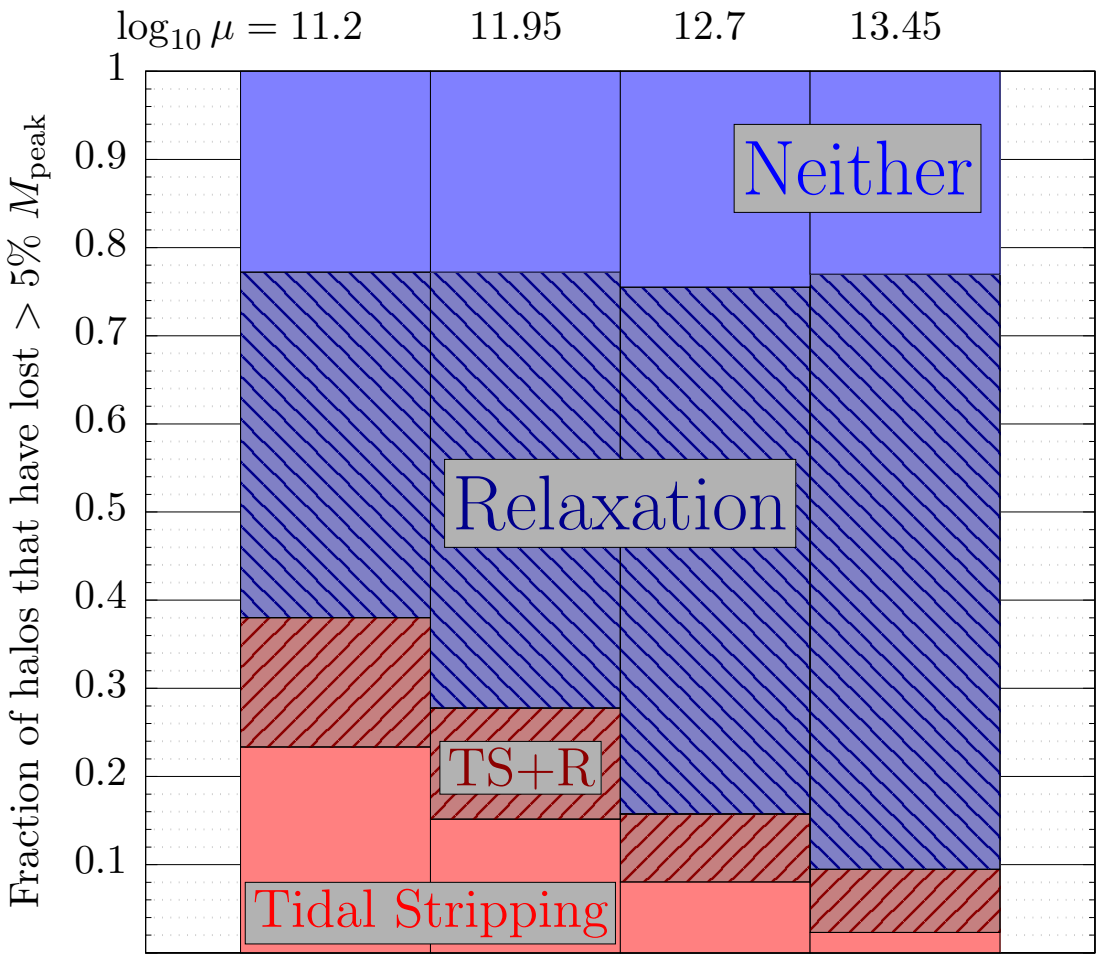

Figure 3.4: Fraction of halos in each mass loss group for different halo mass bins. From each group, we show only the subset of distinct halos that have lost more than 5% of their peak mass. We use the same mass bin definitions as in Fig. 3.1. Group N halos are not apparently subject to the mass loss mechanisms we identify in this analysis, Group TS halos are potentially subject to tidal stripping but not major merger induced mass loss, Group R halos are potentially subject to mass loss following a major merger but not tidal stripping, and Group TS+R halos are potentially subject to both tidal stripping and major merger induced mass loss. Diminished lower mass halos are much more likely to be found in Group TS (about 23% of diminished low mass halos compared to only about 2% of diminished high mass halos), but less likely to be in Group R (about 39% of diminished low mass halos compared to about 67% of diminished high mass halos). Altogether, about 77% of diminished halos fall into one of the three mass loss groups (TS, R, and TS+R); the remaining 23% of halos (group N) have likely lost mass via minor mergers.

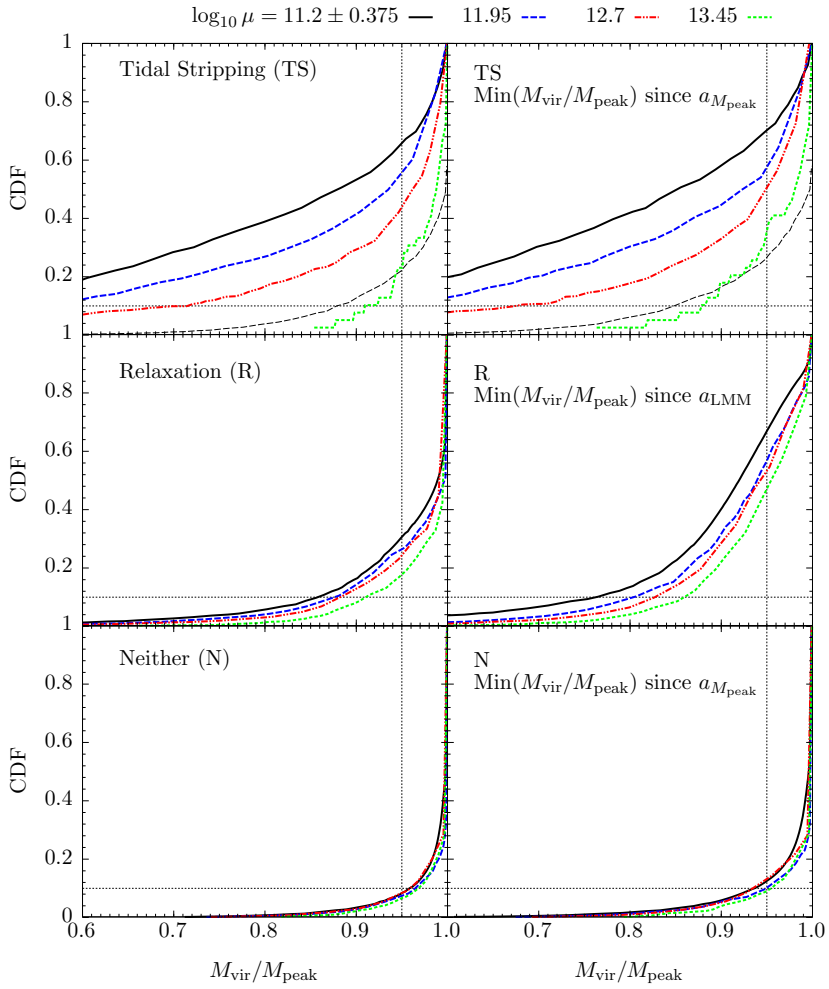

Figure 3.5: Cumulative distribution functions of mass loss fraction for distinct halos that are tidally stripped (group TS, top row), have had a recent major merger (group R, middle row), and are neither tidally stripped nor had a recent major merger (group N, bottom row). We use the same mass bin definitions as in Fig. 3.1. In the left column we define the mass loss fraction for each halo as the ratio of final halo mass at $z = 0$ to peak halo mass, while in the right column we instead compute the fraction using the minimum virial mass since the halo reached $M_{\rm peak}$ (or since $a_{\rm LMM}$ for group R halos). This allows us to compare the distribution of mass loss fractions at $z = 0$ compared to the distribution of peak mass loss for each group. Different coloured lines represent different mass bins.

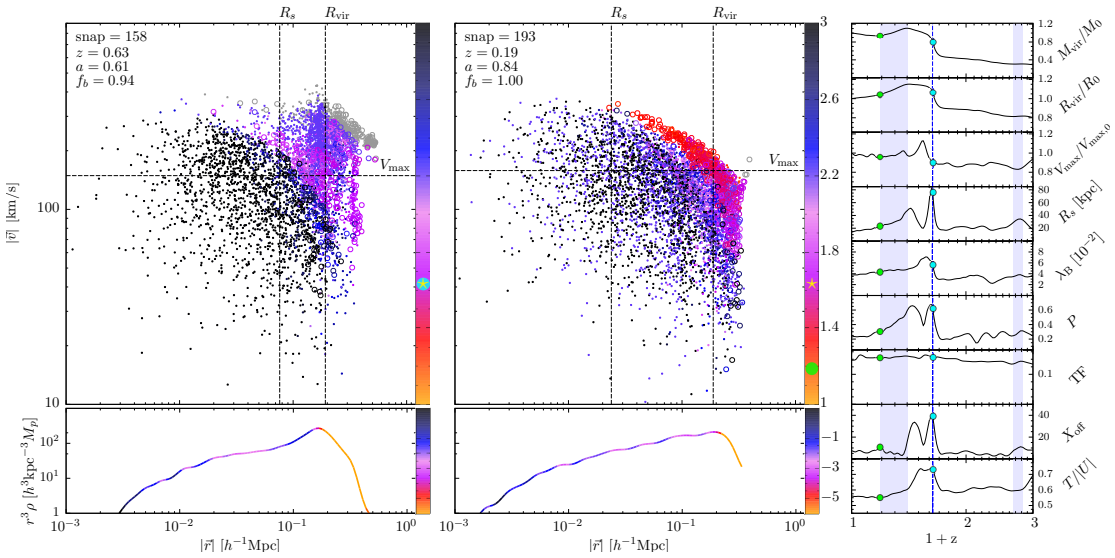

Figure 3.6: Particle distributions, density profiles, and halo property evolution of an individual group R halo at two distinct snapshots. Large panels show the distribution of particles at $z = 0.63$ (left) and $z = 0.19$ (right). On the x-axis (y-axis) we plot the magnitude of the radial (velocity) vector of each particle, with the center and bulk velocity of the halo as the origin. Individual particles are coloured according to the redshift they are first accreted onto the halo (the associated colour bar is in units of $1 + z$). Solid points represent particles that will remain bound to the halo at $z = 0$, while open circles represent particles that will be removed from the halo by $z = 0$. Gray coloured particles are unbound. In each large panel, we also indicate the current simulation snapshot, scale factor, fraction of particles that are bound (f_b), and the current location of $V_{\rm max}$, R_s, and $R_{\rm vir}$. In the associated colour bar on the right, the yellow star indicates the occurrence of a major merger, while the cyan and green circles indicate the current time. The (bottom) panels below the particle distributions show the halo density profiles at each snapshot. We scale the profiles by r^3 to highlight deviations of the outer profile from a r^{-3} (NFW) slope. The associated color bar on the right indicates the $\log r - \log \rho$ slope of the density profile. For an NFW halo, the slope would be -1 (dark blue) below R_s, and -3 (purple) above R_s. Black sections indicate extremely shallow profiles, while red and orange sections indicate very steep profiles. The rightmost column of plots show the full evolution of mass, virial radius, $V_{\rm max}$, scale radius, spin parameter, prolateness, tidal force, $X_{\rm off}$, and virial ratio for this halo from $z = 2$ to 0. The green (cyan) circles indicate the location of the left (right) main panels. The vertical blue dashed line shows where a major merger occurs, and the blue shaded regions indicate periods of mass loss. Mass, virial radius, and $V_{\rm max}$ are each normalized by their $z = 0$ values. The left main panel ($z = 0.63$) coincides with the last major merger.

force below 1) or merger-induced mass loss (from a minor merger); we will further investigate these possibilities shortly.

Looking at the distribution of the mass loss fraction among group R halos (those that experienced a recent major merger but no tidal stripping; Fig. 3.5, middle row), we see that roughly 18% (low mass) – 32% (high mass) of halos are diminished. However, the distribution changes considerably when looking at the minimum mass loss fraction since the last major merger; in this case, the fraction of diminished halos jumps to roughly $48-68\%$ of all group R halos. Furthermore, we see that nearly all group R halos experienced mass loss of a few percent of their peak mass or more, with lower mass halos tending to lose more mass than higher mass halos. Most major mergers cause losses of around $5-15\%$ $M_{\rm peak}$ and very few result in heavy mass loss of more than $\sim$ 20% $M_{\rm peak}$, consistent with the trends from Fig. 3.2 that peak around $M_{\rm vir}/M_{\rm peak} \approx 0.90$ for low mass halos (lower concentration, higher spin, more prolate halos). Once halos have relaxed and begun re-accreting material after a major merger, they will eventually return to and exceed their original peak mass and restore the mass loss fraction to 1. This explains why the left panel (mass loss fractions at $z = 0$) is so different from the right panel; many of the halos have completed the mass loss process and begun re-accreting, reducing their apparent mass loss fraction.

Let's look in detail at a typical example of mass loss following a major merger. In Fig. 3.6, we show for an individual halo the particle distribution and density profile at two different snapshots ($z = 0.19$ and $z = 0.63$), as well as the full evolution of various halo properties since $z = 2$, including halo mass ($M_{\rm vir}$), virial radius ($R_{\rm vir}$), maximum circular velocity ($V_{\rm max}$), NFW scale radius (R_s), spin parameter ($\lambda_{\rm B}$), prolateness (P), tidal force (TF), offset between density peak and center of mass ($X_{\rm off}$) and virial ratio ($T/|U|$). We've chosen these two snapshots

to highlight the effects of this mass loss scenario on halo properties. At $z = 0.63$ (left main panel), the merging halo has just crossed the virial radius of the main halo; this is the snapshot that ROCKSTAR associates with the merger event. At the same time, we see a sharp increase in halo mass, virial radius, scale radius, spin parameter, prolateness, $X_{\rm off}$, and virial ratio. $V_{\rm max}$ displays a slightly delayed response, and tidal force does not change appreciably. The density profile develops a distinct hump due to the merging core that migrates towards the center of the main halo before splashing back. This behaviour causes corresponding oscillations in the scale radius (which fluctuates due to a poor NFW fit to the temporarily shallower-than-expected outer profile), prolateness, and $X_{\rm off}$. We don't expect to see oscillations in all properties; spin parameter, for example, is not strongly affected by these dynamics. The halo quickly begins to relax, even as additional material flows in following the main merger. By the time the halo mass and virial radius have peaked, most other properties are settling back to historically typical values. The net mass accretion rate turns negative and the halo mass and virial radius start shrinking as high energy loosely bound material escapes beyond the virial radius. At $z = 0.19$ (right main panel), the net accretion rate turns positive again; this is the minimum value of $M_{\rm vir}/M_{\rm peak}$ this halo will reach due to this merger (~ 0.8 in this case). At this point, most halo properties have settled considerably, but scale radius, prolateness, and spin parameter are still somewhat elevated above typical levels. All of the recently accreted material has accumulated along the outermost curved layer of the distribution, with material continuing to flow both in and out along this trajectory. The density profile has smoothed out and appears roughly NFW. We have also created movies that show the full evolution of the halos in Figs. 3.6 and 3.7, which are publicly available. [2]

In Figs. 3.8 and 3.9, we show the distributions of many halo properties for

[2] `https://goo.gl/Qtf9i9`

diminished halos from groups N, TS, R, and TS+R along with non-diminished halos from all groups. We select only diminshed halos from each group to highlight how different types of mass loss influence other halo properties. The distributions are not normalized and have consistent bin sizes within each panel, providing an accurate representation of the relative abundances of halos in each panel. Starting with tidal force (TF; Fig. 3.8 Row 1), we see that most halos with very high TF values (> 1) are diminished group TS halos. Note that this indicates that diminished group TS halos are more abundant than non-diminished TS halos (which would contribute to the gray line), consistent with the CDFs from Fig. 3.5. We also see a tail of diminished group TS and TS+R halos with TF < 1 at $z = 0$, which indicates that at least some halos experience high TF shortly after they reach their peak mass (qualifying them to be in group TS or TS+R), but subsequently return to lower TF regions by $z = 0$. The TF distribution of diminished group N and R halos is similar to that of non-diminished halos, and is limited to the range $0 <$ TF < 1 by the group assignment criteria. The distributions of local density (Fig. 3.8 Row 2) provide qualitatively similar information as the TF distributions (since TF correlates strongly with local density; see Lee et al., 2017). However, we do observe more overlap between local density distributions of low TF (groups N and R) and high TF (groups TS and TS+R) halos than for the TF distributions.

Especially notable for halos that recently experienced a major merger are the next several properties from Fig. 3.8: P, $a_{\rm LMM}$, $C_{\rm NFW}$, and $\lambda_{\rm P}$. Among the diminished halos, we see that halos from group R are significantly more prolate that halos from groups N, TS, and TS+R on average. Group R halos have a peak $C_{\rm NFW}$ similar to that of group N halos, but have notably more low concentration halos than diminished halos from the other groups, and also have the highest

spin parameters. The distributions of $a_{\rm LMM}$ reflect the group selection criteria ($a_{\rm LMM} = 0.45$ is the dividing epoch between groups N/TS and R/TS+R), but also reveal an interesting peak around $a_{\rm LMM} = 0.7$ for diminished group R halos. This peak provides an indication of the characteristic mass loss timescale – the mean time delay between a major merger event and subsequent peak mass loss (in this case fixed at $z = 0$). Halos in group R with $a_{\rm LMM} < 0.7$ likely have begun accreting again, but may not yet have surpassed their previous peak mass by $z = 0$, while group R halos with $a_{\rm LMM} > 0.7$ are likely actively losing mass and have not yet reached their minimum mass.

From Fig. 3.9 Row 1, we see that weakly diminished halos (with a mass loss fraction $\sim 0.8 - 0.95$) are dominated by group R, followed by group N. Strongly diminished group R halos are much less common than those from groups TS and TS+R, reflecting the same trends observed from the CDFs from Fig. 3.1. The distribution of mass loss among diminished group N halos is similar in shape to that of diminished group R halos, but falling off more quickly with increasing mass loss. As do group R halos, weakly diminished group N halos ($M_{\rm vir}/M_{\rm peak} \gtrsim 0.85$) dominate over group TS and TS+R halos in the same mass loss regime, but group N halos are the least common among those that have lost more than 20% of their peak mass. This strongly suggests that the processes responsible for mass loss in group N halos may be similar to the relaxation-based process attributed to mass loss in group R halos (e.g. mass loss after a minor merger). We additionally see in the remaining rows of Fig. 3.9 that diminished group R halos are on average the least symmetric (highest $X_{\rm off}$), and the least relaxed (highest $T/|U|$) compared to diminished halos from the other groups. This is consistent with the the proposed major-merger induced mass loss mechanism. Halos undergoing a major merger would become temporarily unrelaxed and have two cores, increasing both $T/|U|$

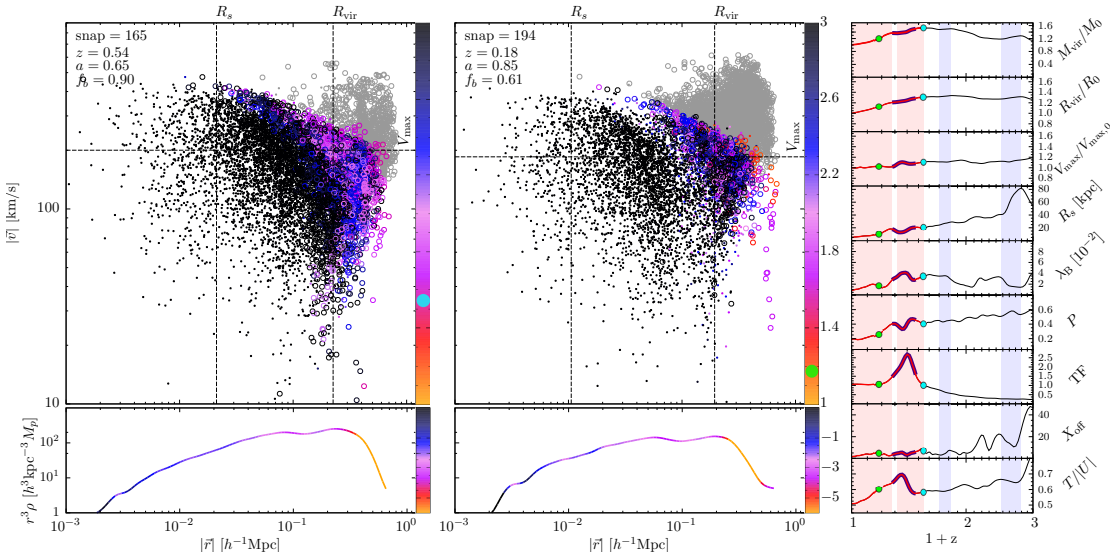

Figure 3.7: Same as Fig. 3.6, but showing a group TS halo at $z = 0.54$ and $z = 0.18$. In this case, no major mergers occur. In the property evolution plots in the rightmost column, red shading indicates periods of mass loss where tidal force is greater than 1 (i.e. tidal stripping). Blue shading indicates periods of mass loss where tidal force is less than 1. The bold red portion (from roughly $z = 0.54$ to 0) indicates where tidal force is greater than 1, and the additional bold purple section shows when this halo is a subhalo of a more massive halo. We've chosen these two snapshots to highlight the affect of tidal stripping on halo properties. The left main panel ($z = 0.54$) coincides with the peak mass and where tidal force becomes greater than 1. We see that most of the (relatively recently accreted) material in the outer part of the halo will be lost by $z = 0$. Shortly after this, the halo becomes a subhalo and experiences much stronger tidal forces. The right main panel ($z = 0.18$) coincides with the minimum tidal force (roughly TF = 1) after the halo again becomes a distinct halo. At this point halo mass, virial radius, $V_{\rm max}$, scale radius, spin, and prolateness have all decreased relative to their pre-subhalo values. We can see a clear separation between the distribution of material in the inner halo and outer halo, and a corresponding steepening of the density profile around this same radius. The decrease in scale radius is a direct consequence of this steepening of the outer density profile. By $z = 0$, the halo will be nearly entirely stripped of the puffed-out outer region.

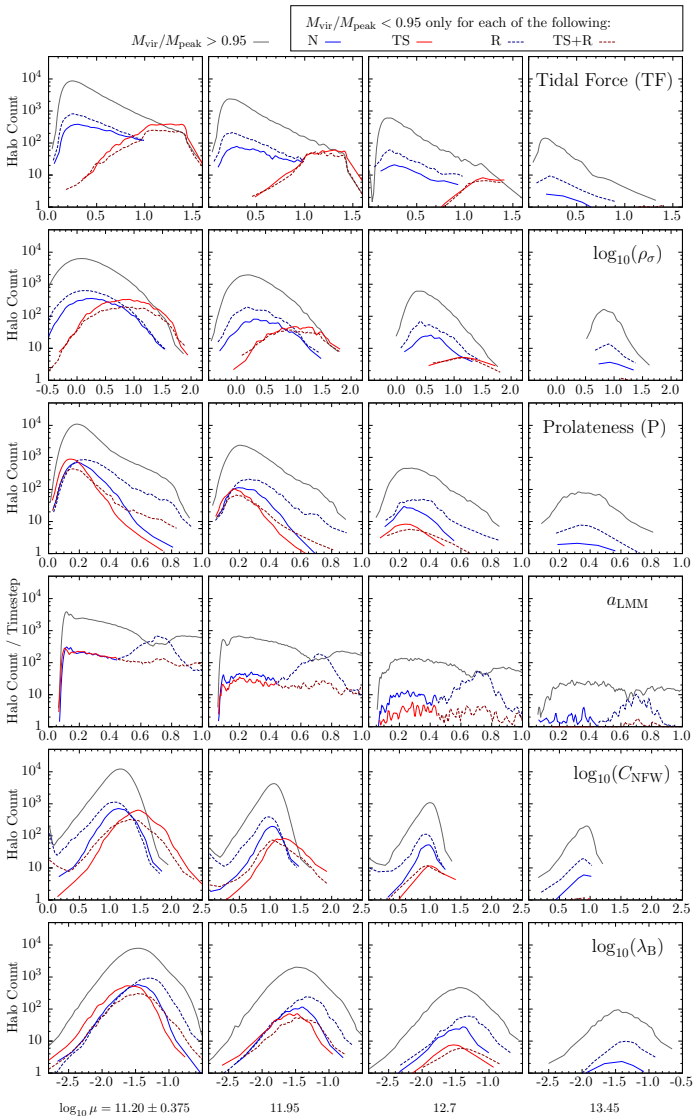

Figure 3.8: Distributions of tidal force, local density, prolateness, scale factor of last major merger, NFW concentration, and Bullock spin parameter for all distinct halos that have not lost a significant amount of mass and for distinct halos that have lost mass in Groups N, TS, R, and TS+R. We use the same mass bin definitions as in Fig. 3.1. Vertical axes show the number of halos in each horizontal bin; all distributions in a given row have the same horizontal bin width to allow for direct comparison to other distributions in the same panel. Values on the horizontal axes correspond to the halo property labelled in the rightmost column of a given row. We divide these distributions into our usual four mass bins, with the lowest mass bin in the leftmost column. The grey lines indicate distributions for all halos in a given mass bin that have not lost more than 5% of their mass since $M_{\rm peak}$. The solid blue, solid red, dashed blue, and dashed red lines represent halos that have lost more than 5% of their mass since $M_{\rm peak}$ and additionally belong to groups N, TS, R, and TS+R, respectively.

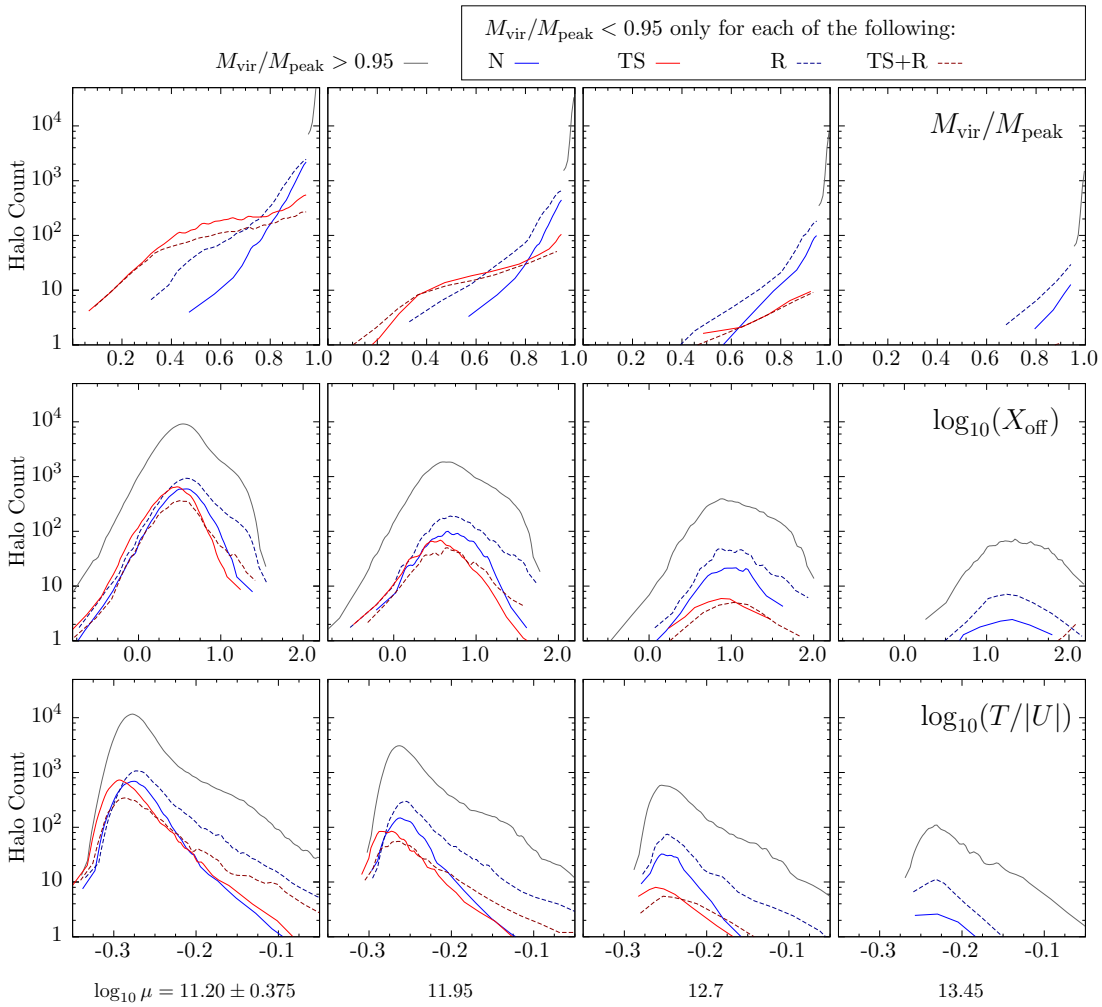

Figure 3.9: Same as Fig. 3.8, but showing mass loss ratio ($M_{\rm vir}/M_{\rm peak}$), offset between halo center of mass and density peak ($X_{\rm off}$), and virial ratio ($T/|U|$). We use the same mass bin definitions as in Fig. 3.1. We see that Group R halos dominate the population of halos that have only experienced moderate mass loss (between 5 and 20% of their peak mass for low mass halos), while tidally stripped Group TS halos are the most common among heavily diminished halos. Group TS halos have slightly lower $X_{\rm off}$ and $T/|U|$ on average compared to undiminshed halos, while Group R halos have slightly higher $X_{\rm off}$ and $T/|U|$ on average. These trends are consistent with our proposed mass loss mechanisms of tidal stripping and post-merger relaxation for Groups TS and R, respectively.

and $X_{\rm off}$ before simultaneously undergoing mass loss and relaxation.

We've additionally followed the most massive progenitors of the same populations plotted in Figs. 3.8 and 3.9 (diminished group N, R, TS, TS+R and not diminished halos) and determined median halo properties of these populations out to high redshift ($z \sim 7$). In Fig. 3.10, we follow the evolution of NFW concentration ($C_{\rm NFW}$), Bullock spin parameter ($\lambda_{\rm B}$), virial mass ($M_{\rm vir}$), and specific mass accretion rate ($\dot{M}/M$). We find that diminished group R halos all exhibit a significant change in behaviour around $z \approx 0.5$ ($a \approx 0.7$), consistent with the strong peak in $a_{\rm LMM} \approx 0.7$ from Fig. 3.8 Row 4. At this epoch, diminished group R halos undergo a decrease in concentration, sharp increase in spin, and increase in specific accretion rate. These halos subsequently regress back towards higher concentrations and lower spins as they approach $z = 0$, but still remain with significantly lower concentrations and higher spins at $z = 0$ compared to the other populations plotted. After the increase in accretion rate coincident with the last major merger, these halos experience a sharp drop in accretion rate than dips below zero briefly, before returning to zero at $z = 0$. This clearly illustrates the mass loss phenomenon these recently merged halos experience – an initial surge in mass from the merging halo (which also sets $M_{\rm peak}$), followed by a period of mild mass loss as the halo relaxes and sheds high energy material. Interestingly, diminished group N halos exhibit each of these trends as well, but with less deviation from their historic median values compared to group R halos. This gives further weight to the suggestion that diminished group N halos have likely experienced mass loss due to a minor merger, rather than unaccounted-for tidal stripping or some other new mass loss mechanism. We additionally note that all halo populations plotted have similar median concentrations and spins at high redshift, while diminished group R halos were the least massive and slowest accreting ha-

los, followed by group N, group TS+R, and group TS halos, respectively. These trends are consistent across all mass bins shown, a further indication that this merger-induced mass loss is a general phenomenon affecting a wide range of halo masses in a similar fashion.

From Fig. 3.11 Rows 2 and 3, we see that for diminished group R halos, changes in concentration ($C_{\rm NFW} \equiv R_{\rm vir}/R_s$) stem almost entirely from changes in R_s rather than $R_{\rm vir}$. The scale radius is strongly amplified during the major merger, and remains substantially elevated at $z = 0$ even after regressing during the post-merger relaxation phase. We do not interpret this dramatic fluctuation in scale radius as a shift in the $\log \rho - \log R_{\rm vir}$ slope change from -1 to -3 as is typically expected for an NFW halo, but rather as a result of a poor fit to a halo profile that no longer resembles the NFW profile. Attempting to fit an NFW profile to an unrelaxed halo with a recent accumulation of mass in the outer regions will tend to produce an artificially elevated scale radius in an attempt to compensate for the shallower than expected outer profile slope. Again, we note that diminished group N halos mirror the R_s evolution of diminished group R halos, but do not experience as dramatic a response.

Finally, we see from Fig. 3.12 that diminished group R halos undergo a sharp increase in prolateness, asymmetry, and virial ratio coincident with the typical last major merger epoch. The prolateness measured at $R_{\rm vir}$ peaks strongly shortly after the merger and then subsides, but remains elevated compared to all other groups at $z = 0$. When measured at R_{500c}, prolateness peaks shortly after $P_{R_{\rm vir}}$ does, and is less dramatic than the peak in $P_{R_{\rm vir}}$, consistent with the picture that a typical merging halo will initially disrupt the outer halo and become substantially stripped before punching into the inner part of the halo. The peak in $D_{\rm off}$ and $T/|U|$ coincide with the peak in $P_{R_{\rm vir}}$, indicating that halos become less symmetric

(halo density peak and center of mass becoming misaligned to due the addition of an off-center clump of material from the merging halo) and unrelaxed. Of the trends shown in Fig. 3.12, $T/|U|$ shows the least dramatic divergence for diminished group R halos compared to diminished halos from groups TS, TS+R, and N. By $z = 0$, diminished group R halos have largely completed the relaxation process, returning to values of $D_{\rm off}$ and $T/|U|$ comparable to the non-diminished halos. Group N diminished halos exhibit similar behavior as those from group R, but are much more weakly elongated, especially when measured at R_{500c}, and typically fully relaxed by $z = 0$. These trends are consistent for all four mass bins shown, albeit with more uncertainty present at higher masses due to low number statistics.

This leaves us with a detailed and coherent picture of how major mergers affect the properties of dark matter halos and ultimately induce mass loss through relaxation. Diminished group R halos, which are those we identify at $a = 1$ as being most directly subject to this process, typically experienced a major merger around $a = 0.7$. The physical properties of the host halo begin to change dramatically as the incoming halo impinges on the host, becomes tidally disrupted, and deposits material on the host halo. The host halo becomes less concentrated, since the NFW scale radius increases to accommodate the recent accumulation of material in the outer profile. Simultaneously, the spin parameter and halo prolateness typically increase due to a non-zero impact parameter and a preferred axis of accretion (mergers would tend to flow along the directions of pre-existing filaments or sheets). The host halo becomes increasingly unrelaxed and less symmetric during this brief mass accretion phase of the merger. As the core of the merging halo becomes fully disrupted and integrated into the host halo, the system relaxes and once again becomes more concentrated, lower spin, less prolate,

and more symmetric. The net mass accretion rate turns negative as the amount of newly infalling material decreases and high energy material gradually dissipates or is moved outside the virial radius of the halo. This is what constitutes the post-merger mass loss mechanism. Post-merger mass loss peaks very shortly before $z = 0$ for diminished group R halos, after the halos have relaxed considerably, but still have considerably higher spin parameters than before the merger.

3.3.2 Tidal Stripping

The other principal mass loss mechanism we've identified in this work is the tidal stripping of material from the outer regions of halos, which primarily occurs in high density regions as a result of strong tidal forces from a nearby massive halo. In Fig. 3.5 Row 1, we see that nearly all group TS halos (those that have had TF > 1 at any point since their peak mass), have less mass at $z = 0$ compared to their peak mass. A majority (66%) of halos in the lowest mass bin ($\log_{10}\mu = 11.2 \pm 0.375$) are diminished at $z = 0$, and about 30% of these halos have lost more than 30% of their mass, a far greater fraction than group R halos from the same mass bin, even when comparing to their maximum mass loss since their last major merger. The left and right panels of the group TS distributions are nearly identical, indicating that these halos are at their historic minimum mass at $z = 0$. In other words, halos that undergo tidal stripping do not generally recover and begin accreting rapidly again. If that were common behaviour, we would expect to see a vertical shift in the right panel (minimum $M_{\rm vir}/M_{\rm peak}$ since $M_{\rm peak}$). This suggests that most group TS halos either become subhalos or disappear completely in subsequent timesteps. There is also a strong mass dependence in the distribution of mass loss fraction among group TS halos. High mass halos are much less likely to be heavily stripped than low mass halos

(66% of low mass halos are diminished at $z = 0$, compared to only 24% of high mass halos). This may be a result of fewer sufficiently massive neighbouring halos for high mass halos than low mass halos. High mass halos tend to be dispersed throughout the cosmic web in nodes and thick filaments, and are less likely to come in contact with another halo sufficiently massive to tidally disrupt it and induce mass loss. Additionally, we have not excluded the possibility of recent minor mergers contributing to mass loss. For low mass group TS halos, we expect mass loss to be primarily due to tidal stripping, but some of the high mass diminished group TS halos in our sample may be experiencing mass loss due to a recent minor merger; indeed, the distribution of of these halos is similar in shape to the distribution of group R and group N halos.

Again, we take a look at an example of an individual halo experiencing significant mass loss via tidal stripping. Fig. 3.7 shows the particle distribution and density profile of the halo at two key snapshots ($z = 0.54$ and $z = 0.18$), as well as the full evolution of many halo properties since $z = 2$. We've chosen these two snapshots to highlight the effects of this mass loss scenario on halo properties. At $z = 0.54$ (left main panel), the halo is just crossing into a region with tidal force $>$ 1, indicating that the Hill radius $R_{\rm Hill}$ from a massive nearby halo is smaller than the virial radius of the halo (i.e., that weakly bound material in the outer part of the halo will be stripped away). This snapshot also coincides with the peak mass of the halo and the start of nearly continuous mass loss for the remainder of the simulation runtime. At $M_{\rm peak}$, most other halo properties have not yet changed significantly in response to tidal effects, although we already see a mild steepening of the outer density profile just before $R_{\rm vir}$, as well as a build up of bound and unbound material outside the virial radius. Shortly after $M_{\rm peak}$, the halo punches into a more massive halo and becomes a subhalo (indicated by the thick purple

line segment in the property evolution panels on the right). This results in a brief increase in virial ratio and a strong peak in tidal force; most other halo properties fluctuate mildly during this period, though we also expect halo finder noise to increase significantly in such regions of extreme density. The (sub)halo re-emerges from the massive halo and again becomes a distinct halo. At $z = 0.18$ (right main panel) the tidal force drops to 1 again, marking the end of the very high tidal force event, although it does not decrease below 1 for the remainder of the simulation. By this time, halo mass and radius have decreased significantly compared to their peak values, and continue to decline. Scale radius, spin parameter and shape have all decreased notably. The outer density profile falls off faster than r^{-3} just before $R_{\rm vir}$, causing the NFW fit to artificially suppress the scale radius. It is perhaps clearer to visually detect from the particle distribution the separation between the inner core of the halo and the soon-to-be-stripped mass of material sitting near the virial radius. Likely, the removal of so much material on the outskirts of the halo, in particular high energy material on very elliptical orbits, contributes to the overall sphericalization and decrease in spin parameter that we see during this process. These trends largely continue towards $z = 0$, by which time the halo has lost roughly 35% of its peak mass.

The trends observed for the individual halo in Fig. 3.7 are consistent with those observed for the whole population of group TS halos. From Fig. 3.8, we'll focus our discussion on Rows 3-6. We see that diminished group TS halos are the least prolate (most spherical), compared to all other populations plotted. At least at low masses, the prolateness distribution of group TS halos both peaks at a lower prolateness and is skewed towards lower prolateness values. Group TS halos have significantly higher average concentrations compared to the other groups. The concentration distribution peaks around $C_{\rm NFW} = 32$ for group TS (compared to

only about 11 for group R halos), but also has a higher dispersion. Very few diminished group TS halos have concentrations below about 10, while this is common for group R and non-diminished halos. These halos also have the lowest average spin parameter compared to the other groups plotted. While the peak spin parameter of diminished group TS halos is only slightly below that of group N halos, the distribution is skewed towards lower spins. These trends indicate that diminished group TS halos are most differentiated from other halos by their much higher average concentration, but also are typically more spherical (less prolate) and have lower spins. These trends are all weaker at higher masses; the properties of group TS halos are more differentiated from the remaining populations at lower masses.

As expected, diminished group TS+R halos display trends that are somewhat intermediary between those of group TS and group R. They have a prolateness distribution similar to that of the non-diminished halos, though peak at slightly lower prolateness. There is a subtle peak in $a_{\rm LMM}$ around 0.7, coincident with the peak in group R halos, indicating merger-induced mass loss is at least partly responsible for the differences in halo properties of group TS+R halos compared to non-diminished halos. These halos also have a higher average concentration than group R, N, and non-diminished halos, but less than group TS halos. The spin distribution of group TS+R halos is similar in shape to that of group N and non-diminished halos, but with an excess of high spin halos (at least for the lowest mass bin).

From Fig. 3.9 we see that low mass diminished group TS and TS+R halos have a dramatically different distribution of mass loss ratio compared to group R and N halos. While halos from all groups are more likely to be less diminished than more diminished, group TS and TS+R halos are much more likely to be

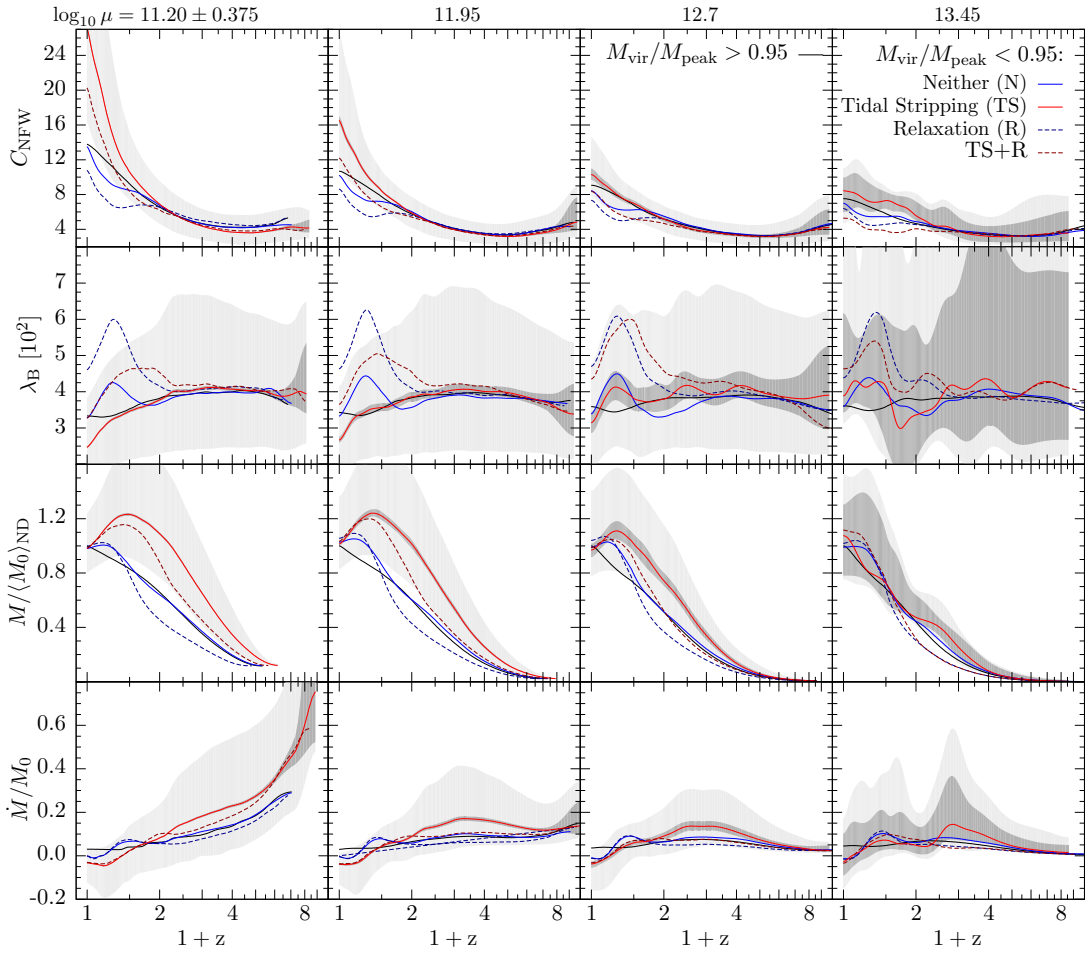

Figure 3.10: NFW Concentration, spin parameter, mass, and specific mass accretion rate histories for all distinct halos that have not lost a significant amount of mass (not diminished (ND): $M_{\rm vir}/M_{\rm peak} > 0.95$) and for distinct halos that have lost mass ($M_{\rm vir}/M_{\rm peak} < 0.95$) in Groups N, TS, R, and TS+R. We use the same mass bin definitions as in Fig. 3.1. The curves reflect median properties of the progenitors of the z = 0 halo populations. The dark grey shading reflects the 95% confidence interval on the median and the light grey shading reflects the $20-80\%$ dispersion of each property, shown only for Group TS halos. Each halo mass curve is normalized to the $z = 0$ value of the not diminished (ND) curve in each mass bin. We see that halos experiencing purely tidal mass loss (Group TS) experience amplified concentrations, reduced spin parameters, and heavily reduced accretion rates and halo mass at late times. In contrast, halos that underwent purely merger induced mass loss (Group R) exhibit temporarily reduced concentrations, strongly amplified spins, and a recent burst of accretion, followed by mild mass loss. Group TS+R halos display milder trends consistent with both tidal stripping and relaxation, while Group N halos display trends that are most consistent with those from Group R, but subdued, suggesting these may be halos experiencing weaker relaxation-based mass loss from minor mergers.

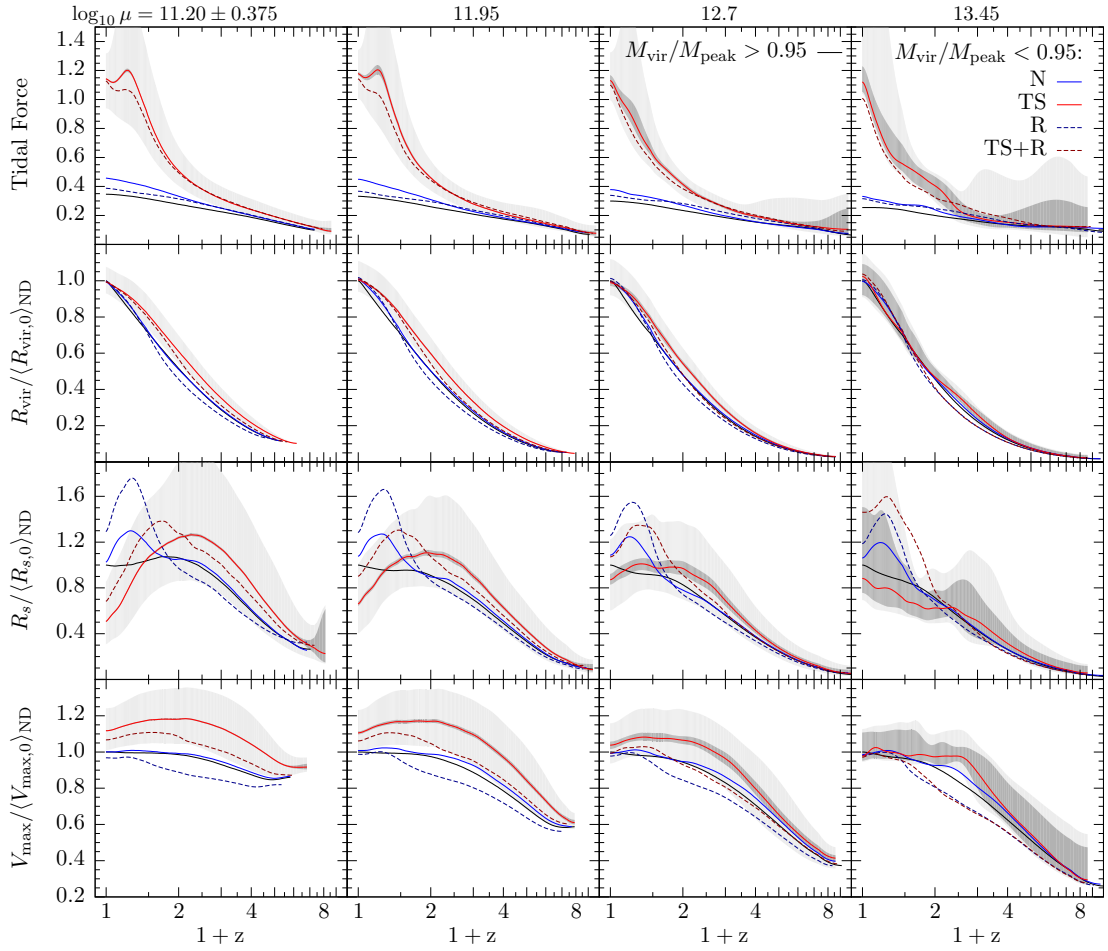

Figure 3.11: Same as Fig. 3.10, but showing tidal force, virial radius ($R_{\rm vir}$), scale radius (R_s), and maximum circular velocity ($V_{\rm max}$). To efficiently compare different mass bins, we normalize $R_{\rm vir}$, R_s, and $V_{\rm max}$ by the median values of the not-diminished (ND) population at $z = 0$. Note that the $R_{\rm vir}$ curves must converge at $z = 0$ as a consequence of the halo mass curves (Fig 3.10 Row 3) converging at $z = 0$. We see that halos experiencing purely tidal mass loss (Group TS) typically experience much stronger tidal forces starting around $z \approx 1 - 2$ and peaking shortly before $z = 0$, strongly depressed scale radii and mildly reduced maximum circular velocity, both roughly coincident with the increase in tidal force. In contrast, halos that underwent purely major merger induced mass loss (Group R) exhibit consistently low tidal force, temporarily amplified scale radii, and a jump in maximum circular velocity roughly coincident with the major merger. Group TS+R halos display milder trends consistent with both tidal stripping and post-merger mass loss, while Group N halos display trends that are most consistent with those from Group R, but subdued, suggesting these may be halos experiencing weaker relaxation-based mass loss from minor mergers.

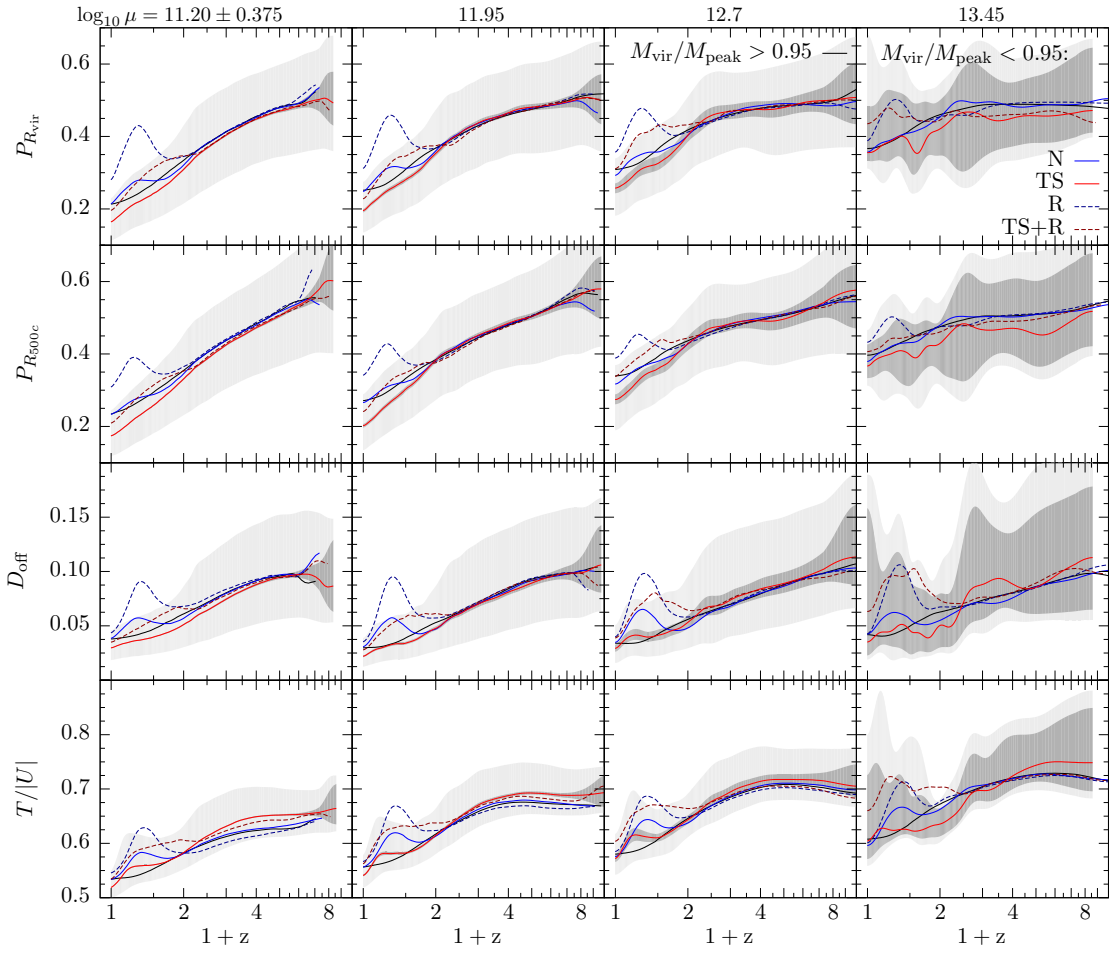

Figure 3.12: Same as Fig. 3.10, but showing prolateness measured at $R_{\rm vir}$ ($P_{R_{\rm vir}}$), prolateness measured at R_{500c} ($P_{R_{500c}}$), $D_{\rm off}$, and the virial ratio. We see that halos experiencing purely tidal mass loss (Group TS) typically become steadily rounder and more symmetric. In contrast, halos that underwent purely major merger induced mass loss (Group R) temporarily become highly elongated, especially at larger radii, highly asymmetric, and unrelaxed, all coincident with the merging event. Group TS+R halos display much milder trends consistent with both tidal stripping and relaxation, while Group N halos display trends that are most consistent with those from Group R, but subdued, suggesting these may be halos experiencing weaker mass loss from minor mergers. Diminished halos from all groups experienced a jump or plateau in virial ratio around $z = 0.5$, followed by relaxation by $z = 0$, with the most unrelaxed halos coming from groups R, TS+R, N, and TS, in order of most to least, respectively.

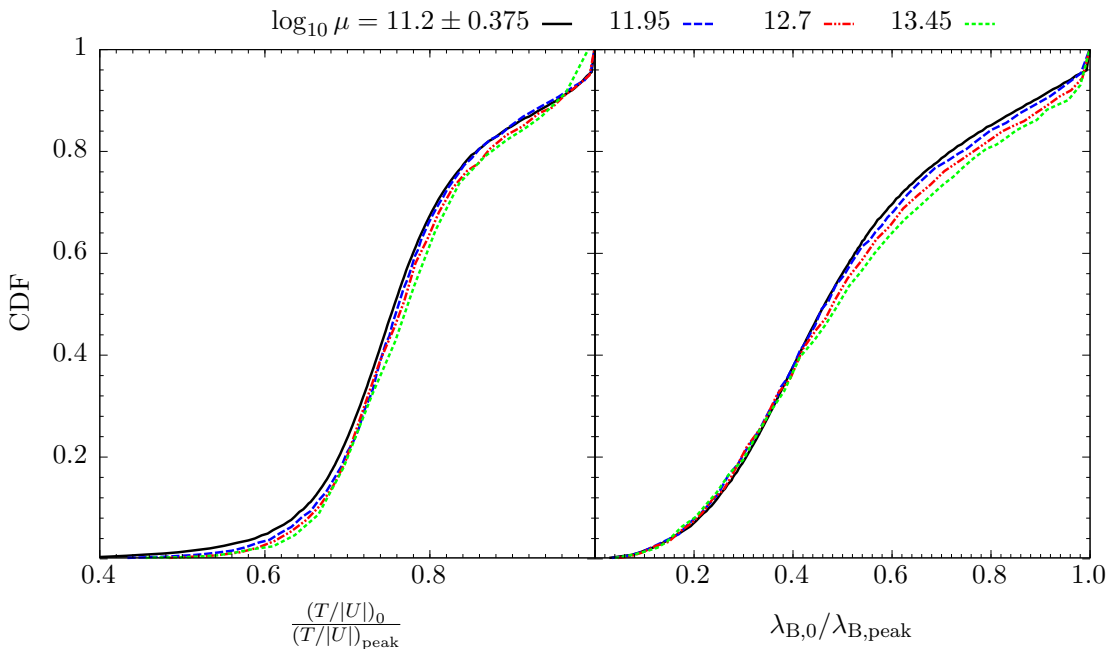

Figure 3.13: Cumulative distribution functions of virial ratio ($T/|U|$) decline on the left panel and spin parameter ($\lambda_{\rm B}$) decline on the right panel for all group R halos (distinct halos that had a recent major merger but have not experienced strong tidal forces). We use the same mass bin definitions as in Fig. 3.1. In each case, we compute the ratio of the $z = 0$ values to the peak value since the last major merger. This provides an indication of the degree to which virial ratio and spin parameter typically decay following a major merger, since both of these properties tend to increase sharply immediately after a major merger. Different coloured lines represent different mass bins, though we see very little mass dependence. The median decline in virial ratio is about 24% of the peak value, while the median decline in spin parameter is about 52% of the peak value. About 80% of these group R halos decline by at least 15% in virial ratio, while nearly 90% decline by at least 15% in spin parameter. This tells us that elevated spin parameters following major mergers are transient; they typically decay substantially by $z = 0$, at least when considering only the material within the virial radius of the halo. Fluctuations in virial ratio are less dramatic that in spin parameter, but show qualitatively similar time-dependence following a major merger.

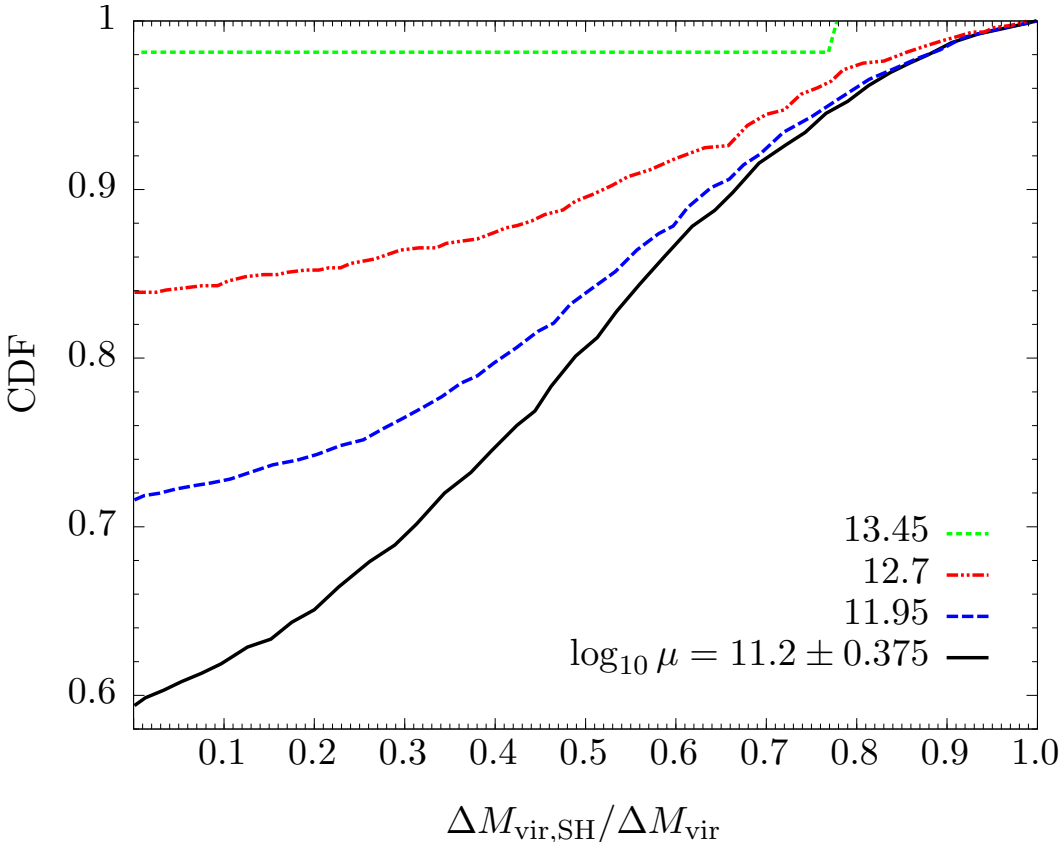

Figure 3.14: Cumulative distribution function of fraction of mass lost while a subhalo for all tidally stripped halos (group TS). We use the same mass bin definitions as in Fig. 3.1. We define $\Delta M_{\rm vir}$ as the total cumulative mass loss since $M_{\rm peak}$, not including any periods of mass growth. So $\Delta M_{\rm vir,SH}$ represents any loss that occurs while (temporarily) a subhalo. Different coloured lines represent different mass bins. For the lowest mass bin, we see that about 60% of halos did not lose any of their mass as subhalos. About 80% of these halos lost half of their mass or less as a subhalos, leaving only about 20% of halos having experienced the majority of their mass loss as a subhalo. Mass loss while a subhalo is much less common for higher halo masses. Roughly 72% of $\log_{10}\mu = 11.95$ halos, 84% of $\log_{10}\mu = 12.7$, and 98% of $\log_{10}\mu = 13.45$ halos have not lost any mass as a subhalo.

heavily diminished ($M_{\rm vir}/M_{\rm peak} < 0.7$) than group R and N halos. Since the distributions of TS and TS+R halos are nearly identical (with only a difference of overall abundance), we expect that tidal stripping is the dominant mass loss mechanism affecting group TS+R halos, rather than post-merger mass loss. The distributions of $X_{\rm off}$ are not remarkable for group TS and TS+R halos, with only a slight tendency towards lower $X_{\rm off}$ for group TS halos (more symmetric). Group TS+R halos are about as relaxed as non-diminished halos, while the purely tidally stripped group TS halos tend to be more relaxed (at least, with lower $T/|U|$) than any of the other groups. This isn't surprising, since tidal stripping should be a relatively distributed process, affecting mostly the outer regions of the halo and especially any loosely bound, high energy particles on highly elliptical orbits. As has been repeated before, these trends hold especially for the lower mass halos, and begin to break down or lose statistical weight at higher masses.

Examining the evolution of halo properties for diminished group TS and TS+R halos further clarifies the role tidal stipping plays in shaping key halo properties like concentration, spin and shape, among others. In Fig. 3.10 we see that low mass diminished group TS and TS+R halos develop increasingly higher concentrations, which diverge from those of the non-diminished halos around $z = 1$. We expect this is roughly the epoch when these halos enter high density regions and begin to experience very high tidal forces. Indeed, shortly following the divergence in concentration, the median mass of group TS and TS+R halos plateaus and begins to decline in response to tidal stripping. Group TS halos have consistently higher concentrations than group TS+R halos since $z = 1$, while the median concentration of group TS+R halos initially drops below that of non-diminished halos, before rapidly increasing and surpasing them by $z = 0$. These fluctuations may be due to the combination of early concentration suppression by a major

merger, followed by concentration amplification from tidal stripping. The spin parameters of diminished group TS halos follow a distinct trend compared to all other groups shown. At least for the lower mass halos, those experiencing purely tidal mass loss also demonstrate increasingly reduced spin parameters. While all halo populations had similar median spins above roughly $z = 2$, those in group TS diverge sharply from the non-diminished halos shortly after $z = 0.5$, around the same time the specific mass accretion rate reaches a minimum. We interpret this to be a result of preferential removal of high energy material on highly elliptical orbits, reducing the net angular momentum of the halo. Interestingly, group TS+R halos have a fairly different spin parameter evolution than group TS halos, even for the lowest mass bin, seen by the increase in spin parameter around $z = 1$. This is presumably in response to a major merger, and results in a broader peak in spin parameter compared to that experienced by group R and N halos. For the specific mass accretion rate (bottom row), we see that for low mass group TS halos the net accumulation of material drops below zero shortly before $z = 0.5$ and reaches a minimum shortly before $z = 0$, but never substantially recovers. Group TS+R halos display similar behaviour, but additionally experience the characteristic bump in accretion rate from a major merger typically around $z = 1$. Note that the typical last major merger experienced by group TS+R halos occurs around $z = 1$, while for group R halos it peaks around $z = 0.5$. This is likely due to the dominance of tidal stripping in the late phase of these halos' evolution. Mergers are less likely to happen when a halo is being tidally disrupted by a larger halo, which places a constraint on the major merger window for group TS+R halos roughly between the assignment cutoff of $a = 0.45$ (or $z = 1.2$) and when stripping kicks in (around $z = 0.5$ for low mass halos). It is clear from these plots that high mass group TS halos behave differently than low mass halos.

In fact, the evolution of high mass group TS halos (and especially group TS+R halos) approach the behaviour of group R halos; that is, a jump in spin parameter and reduced concentration coincident with an increase in accretion rate, followed by relaxation and negative accretion. This suggests that high mass group TS and TS+R halos may be more strongly influenced by minor and major mergers, respectively, while low mass group TS and TS+R halos are likely dominated by the effects of tidal stripping.

By definition, group TS and TS+R halos have completely different tidal force histories, as seen in Fig. 3.12 Row 1. However, note that the tidal forces experienced by halos in all groups are roughly comparable for $z > 2$, indicating that halos being tidally stripped in high density regions at $z = 0$ originated from regions of roughly average density where they experienced much milder tidal forces. Around $z = 1$ the tidal forces experienced by diminished group TS and TS+R halos diverges sharply from the remaining groups until reaching a maximum around TF $= 1.2$ near $z = 0$. For lower mass halos in particular, both TS and TS+R halos peak shortly before $z = 0$, at around $z = 0.2$, roughly coincident with the minimum mass accretion rate (peak mass loss rate). This tells us that specific mass accretion rate is strongly correlated with the tidal force, and that these halos typically have already endured a period of closest approach to a massive halo (peak in tidal force) paired with maximum instantaneous mass loss. Presumably, most of these halos have already made one pass through or near a massive neighbour and are preparing to make subsequent passes before becoming subhalos. Note that since we are only including ($z = 0$) distinct halos in our analysis, we are likely missing transient subhalos (halos that temporarily become subhalos for a period of time while passing through a massive halo, before becoming tidally stripped distinct halos upon emerging). Some of the $z = 0$ distinct group TS and TS+R

halos may have lost much of their mass as transient subhalos around the $z = 0.2$ peak in TF. High mass group TS and TS+R halos still have very high tidal forces at late times, but do not show any clear indication of previous peaks in tidal force.

In Fig. 3.11 Rows 3 and 4 we show the evolution of the NFW scale radius and the maximum circular velocity ($V_{\rm max}$). Low mass diminished group TS halos exhibit a dramatic reversal in scale radius evolution at about $z = 1$, roughly coincident with the transition towards higher density, higher tidal forces regions. Evolution in scale radius is the primary differentiator of evolution in concentration, since the virial radius is not highly sensitive to mass loss or group assignment. For group TS halos, we see that the typical halo experiences a plateauing of scale radius around $z = 1$, followed by a sharp decline all the way to $z = 0$. Group TS+R halos initially experience an increase in scale radius (presumably to due the major merger), peaking around $z = 0.5$, followed by a sharp decrease. Tidal stripping preferentially removes loosely bound material from the outer regions of halos. As a result, tidally stripped halos tend to have density profiles with outer slopes that fall off faster than r^{-3}. Forcing an NFW fit to these halos produces artificially low scale radii in an attempt to compensate for the steep outer profiles. Some of the internal halo structure is influenced by tidal stripping as well, as can be seen by the decline in $V_{\rm max}$ after $z = 1$. $V_{\rm max}$ is not as sensitive to changes to the outer halo as NFW concentration, and provides a more robust quantifier of halo internal structure than the scale radius for non-NFW halos. A decline in $V_{\rm max}$ indicates the removal of particles that spend some of their time in the interior of the halo. High mass group TS halos exhibit little to no scale radius and $V_{\rm max}$ suppression at late times, while high mass group TS+R halos have scale radius and $V_{\rm max}$ evolution comparable to that of group R halos, a further indication that high mass group TS+R halos are primarily influenced by the effects of a major

merger rather than tidal stripping.

Finally, in Fig. 3.12, we examine prolateness, asymmetry ($D_{\rm off}$), and virial ratio ($T/|U|$). All halos generally become less prolate with time, but group TS halos do so the most quickly on average. While the median prolateness of halos in all groups is indistinguishable above $z = 1$, group TS halos sphericalize the most rapidly afterwards. Still, the slope difference between group TS and group N halos after $z = 1$ is slight, and there does not appear to be a sharp change in $P_{R_{\rm vir}}$ or $P_{R_{500c}}$ coincident with the onset of tidal stripping, as we see with spin and scale radius, for example. Instead, tidally stripped halos are gradually rounded as they lose particles on highly elliptical orbits. Both the inner ($P_{R_{500c}}$) and outer ($P_{R_{\rm vir}}$) shapes of group TS halos are noticeably rounder than halos from other groups at $z = 0$, indicating that stripping is not solely affecting the outer regions of halos. We also see that group TS halos are the most symmetric (lowest $D_{\rm off}$) and have the lowest virial ratios at $z = 0$. However, tidal stripping does not appear to strongly affect the halo center of mass, since there remains little difference between group TS and not-diminshed halos throughout their evolution. Group TS halos do experience somewhat different virial ratio evolution, however, since they are typically the least relaxed at high redshift and experience a plateau during the tidal stripping phase. Group TS+R halos have trends that combine elements of those from groups R and TS, favoring group TS and low masses and group R at high masses; that is, a jump up in prolateness (especially $P_{R_{\rm vir}}$), $D_{\rm off}$, and $T/|U|$, followed by gradual declines for low mass halos, and evolution consistent with group R halos at high masses.

Altogether, these trends produce a clear picture of how tidal stripping influences halo properties. Group TS and TS+R halos move from average density regions at high redshift into high density regions where they experience increas-

ingly strong tidal forces around $z = 1$. These strong tidal forces are likely due to a single nearby massive halo, whose tidal field eventually begins to preferentially remove loosely bound high energy material from the subjected halo. As the halo begins to loose mass due to tidal harassment, its scale radius begins to artificially depress due to a steepening outer profile, its spin decreases, and it becomes rounder. Most halos reach a minimum accretion rate as they pass by or through the neighbouring halo shortly before $z = 0$. We don't expect many of these group TS halos will remain distinct halos for long, since most are at their minimum mass since $M_{\rm peak}$ at $z = 0$ (i.e. very few have started accreting mass again after being stripped). Group TS+R halos have a similar pattern of behaviour to group TS halos at late times, but additionally experienced a major merger (typically around $z = 1$, right before experiencing very strong tidal forces). These halos initially evolve as group R halos do, with decreased concentrations and increased spins, accretion rates, prolateness, asymmetry, and virial ratios, before following the trends of group TS halos as tidal stripping commences. We note that the trends outlined here apply most directly to low mass halos. Higher mass halos seem to be increasingly influenced by merger events. The evolution of high mass group TS+R halos appears dominated by the affects of recent major mergers. Even high mass group TS halos may have lost mass via minor mergers rather than significant tidal stripping.

3.4 Discussion

By analysing the properties of group R halos that have lost more than 5% of their peak mass at $z = 0$ (as we did in Figs. 3.8 - 3.12), we select halos whose last major merger occurred roughly at $a = 0.7$. Halos that had a major merger at a much earlier epoch likely already completed any potential mass loss phase and

resumed accreting beyond their previous peak mass, while those that had a major merger much after $a = 0.7$ may still be accumulating material from the merger and have not yet begun to lose mass. As a result, we don't follow the evolution of these diminished group R halos to the point that they typically start accreting normally again. We get a glimpse of how the properties of an example individual halo recover after a major merger in Fig. 3.6; in this case, the effects of the merger are largely transient, with scale radius, shape, spin parameter, $X_{\rm off}$ and virial ratio all eventually returning to typical pre-merger values. Spin parameter is one of the slowest to settle, and $V_{\rm max}$ never settles substantially. In order to get a sense for how much the spin parameter and virial ratio typically decline after being elevated via a major merger, we examine in Fig. 3.13 the ratio of the $z = 0$ value of these quantities to their maximum values after $M_{\rm peak}$ for all group R halos. Note we don't make any cuts on mass loss, though we expect most of these halos have lost mass at some point (see, e.g., Fig. 3.5). We see that the virial ratio of group R halos typically declines by about 25% from their peak virial ratio after a major merger. For a fully relaxed final halo, this would be a peak virial ratio of $T/|U| \sim 0.66$. Very few halos decline by more than 40%, while about 80% of halos decline by at least 15%. Declines in spin parameter are more substantial, with the typical $z = 0$ value being about 52% less than the peak value since the major merger. The distribution is also more broad, with roughly 8% of halos declining by over 80% and only 10% losing 15% or less of their peak spin parameter value. Remarkably, there is very little mass dependence, indicating that major mergers affect halos in a relatively mass-independent manner. Some of these halos will still be in the process of settling in virial ratio and spin parameter, tending to bias these results towards lower settling fractions.

Given that both mergers and tidal stripping can produce changes to the density-profile-fitted NFW concentration, what implications does this have for the relationship between concentration and formation time? First, major mergers will tend to decrease NFW concentrations, at least temporarily, while tidal stripping will tend to raise NFW concentrations. Younger halos will tend to experience more frequent mergers than older halos, producing a bias towards lower concentrations. At the same halo mass, older halos will tend to be tidally stripped halos in higher density regions, which will cause halos to be biased towards higher concentrations. As a result, the evolution in NFW concentration due to mass loss either through major mergers or tidal stripping will tend to boost the concentrations of early forming halos and decrease the concentrations of late forming halos. Similarly, higher mass halos would tend to have more merger-induced concentration decrease than lower mass halos, creating a bias in the concentration-mass relation. Note, however, that this bias may not be relevant for extremely high mass, just collapsing halos observed at high redshift (see, e.g. Ludlow et al., 2012b), because these halos have not existed long enough to reach equilibrium. If one were to adopt an alternative measure of halo concentration that does not depend on a parametric fit to the entire halo density profile, for example by using the maximum circular velocity and the radius at which it is maximum, we would expect to see a weaker dependence of concentration on formation time, as well as a flattening in the concentration-mass relation compared to using the NFW concentration definition we've adopted in this analysis. Such a study, which would require reanalysis of the halos in a big simulation, is beyond the scope of the present paper.

While we focus on $z = 0$ distinct halos for our analysis, it is true that many tidally stripped halos have previously been subhalos for one (or more) short periods. In the top row of Fig. 3.5 we include a curve for the lowest mass bin only

that represents the cumulative distribution of mass loss fraction for halos that have never been subhalos since their peak mass (the dashed black line, normalized using the full mass bin). From this we see that the majority of diminished group TS halos were subhalos previously, presumably on their first pass through a more massive halo (as was the case in the example in Fig. 3.7). Only about 35% of diminished group TS halos have not been subhalos since their peak mass, and this fraction drops precipitously for halos that have lost more than about 20% of their peak mass. This tells us that tidally stripped distinct halos typically have already passed through a more massive halo, and are destined to be permanently captured as subhalos on the next approach or experience additional pass-throughs before finally being captured. However, we do see some mild and even significant mass loss among the minority of group TS halos that have not been subhalos since their peak mass. Some amount of mass loss can certainly be attributed to tidal stripping by nearby massive halos. The tidal influence of a massive halo can extend well beyond its virial radius; in fact, the tidal force quantifier we're using ($R_{\rm Hill}/R_{\rm vir}$) typically rises above unity before a halo enters within the virial radius of a larger halo. Group TS halos that haven't been subhalos since their peak mass, but have lost a significant fraction of their peak mass ($\gtrsim 20\%$), typically lost most of their mass through major or minor mergers rather than tidal stripping. This can happen when a halo experiences one or more successive minor mergers coincident with entering a high tidal force region, or when a halo experiences severe mass loss following an early ($a_{\rm LMM} < 0.45$) major merger and never fully recovers before entering a high tidal force region. This minority group of halos represents a somewhat complicated and varied collection of scenarios that involve a combination of tidal stripping and mass loss from major and minor mergers. One further question we've investigated is whether the majority of tidal mass loss occurs while

halos are passing through larger halos or while they are distinct halos (before or after passing through). In Fig. 3.14, we show the distribution of the fraction of mass lost while a subhalo since $M_{\rm peak}$ for each of the four halo mass bins (group TS only). Here we do not segregate halos based on mass loss severity, so this includes group TS halos that have lost very little to zero mass. We compute $\Delta M_{\rm vir}$ as the integrated mass loss, not including any positive contributions from periods of accretion, rather than the net mass loss. We see a strong mass dependence; about 60% of the lowest mass halos have not lost any mass as a subhalo, while virtually no high mass halos have lost mass as subhalos. Roughly 20% of halos in our lowest mass bin have lost half or more of their mass as subhalos. Given that a majority of low mass diminished group TS halos have previously been subhalos, this implies that most of these halos experience the majority of their mass loss after they have passed through a more massive halo. This picture is also consistent with our individual halo example (Fig. 3.7), where most of the mass loss occurs after the halo has re-emerged from the larger halo (after the end of the thick purple line segment on the property evolution plots).

Throughout this work we've suggested that diminished group N halos may be the result of mass loss following minor (rather than major) mergers. Indeed, the trends shown in Figs. 3.8 - 3.12 illustrate convincing parallels between diminished group R and N halos. A related analysis by students working with us (Wu & Zhang, 2017) investigates halo by halo whether diminished group N halos did have recent minor mergers, as well as further characterizes the responses of several halo properties to major (and minor) mergers. They use the evolution of halo mass and $V_{\rm max}$ to predict the occurrence of mergers since $a = 0.5$ for each halo, validating their results with the known major merger events from the ROCKSTAR catalog. While this method may not be a reliable predictor of true minor merger events

for an individual halo, it remains useful to provide statistics for populations as a whole. In particular, they found that group N halos typically had their last minor merger around $a = 0.7$, consistent with the distribution of $a_{\rm LMM}$ for group R halos, solidifying our conjecture that group N halos are an extension of the group R mass loss phenomenon towards smaller mass ratios. They also build on the characterization of how spin parameter, $X_{\rm off}$, scale radius, prolateness, and virial ratio respond to major mergers (e.g, Figs. 3.11-3.12), by for each property providing statistics on the number of peaks and when they occur following mergers. Consistent with the results presented in this work, they show that spin parameter and virial ratio typically peak once about $\Delta a = 0.03$ after a merger, while $X_{\rm off}$, scale radius, and prolateness often have two merger-induced peaks (a result of the merging and backsplash of two separate high density halo cores). For properties that peak twice, the first peak usually occurs immediately following the merger, while the second peak is typically delayed by about $\Delta a = 0.08$, but has a fairly broad distribution. Furthermore, they find that the presence of two peaks in these properties is most common for halos that experience a maximum mass loss of $5 - 15\%$ of their peak mass (as opposed to only $< 5\%$ or $> 15\%$). They also considered merger-induced 3rd and 4th peaks, but did not find any convincing indication that these occur. All of these trends are roughly consistent for both major and minor mergers.

3.5 Conclusions

Our main conclusions are as follows:

1. Roughly 22% of low mass (12% of high mass) $z = 0$ distinct halos have lost more than 5% of their peak virial mass.

2. Mass loss occurs either via tidal stripping in high density regions or via relaxation following a merger.

3. Relaxation after most major mergers results in more than 5% mass loss, with the regime of $5 - 15\%$ mass loss being the most common. This is roughly true for all halo masses.

4. Merger-induced mass loss that peaks at $z = 0$ ($a = 1$) results from mergers around $z = 0.4$ ($a = 0.7$). This is the characteristic delay between a merger and the minimum mass the halo subsequently reaches. Note that this delay is somewhat time dependent and will be different for mergers that occur at different times.

5. Halos undergoing merger-induced mass loss typically have lower concentrations, higher spin parameters, are more elongated, more asymmetric, and less relaxed than halos not currently experiencing mass loss. These differences are the result of strong impulses generated by a merger event that have not fully settled back to typical pre-merger values.

6. Minor mergers can also induce mass loss. Minor merger induced mass loss parallels major merger induced mass loss, but has a generally weaker effect on halo properties.

7. A majority of low mass halos in high tidal force regions have lost more than 15% of their peak mass and will not recover. Significant amounts of mass loss ($> 30\%$) are not uncommon. High mass halos rarely experience tidal stripping.

8. Halos undergoing tidal stripping typically have higher concentrations, lower spin parameters, and are more spherical than halos not currently experienc-

ing mass loss. These differences result from steepening of the outer density profiles of halos via preferential removal of high energy material on elliptical orbits.

9. Most tidally stripped distinct halos that have lost more than 5% of their peak mass were previously subhalos as they passed through a more massive halo. This is more likely to have been the case for halos that have lost more mass.

Appendix A

Appendix

This Appendix contains figures that supplement those in the text. Like Fig. 2.3, Fig. A.1 shows the probability distribution of local environment density, but smoothed on $\sigma_s = 4h^{-1}$Mpc rather than $1h^{-1}$Mpc. Fig. A.2 illustrates the connection between percentilized cosmic local densities and halo local densities at various redshifts and smoothing scales, and Fig. A.3 relates the percentilized halo property–density correlation plot (Fig. 2.6) to the non-percentilized halo property–density correlation plot (Fig. 2.5). Fig. A.4 is a supplement to Fig. 2.6, showing the 20-80 percentile range and the 95% confidence interval on the median at the 1/2 h^{-1}Mpc smoothing. Supplementing Figs. 2.6 and 2.7, which show the NFW concentration and $\lambda_{\rm B}$ distribution with density at $z = 0$ and their redshift evolution, Figs. A.5 and A.6 show the similar behaviour of Klypin concentration and $\lambda_{\rm P}$. Fig, A.5 also shows the distribution with density of halo maximum circular velocity $V_{\rm max}$. Figs. A.7 and A.8 supplement Fig. 2.6 by showing only halos that have lost less than 2% of their mass versus those that have lost more than 2% of their mass, showing the strong effects of stripping on halo concentration, spin, and mass accretion rate, especially for lower mass halos in high density regions. Figs. A.9, A.10, and A.11 extend Fig. 2.5 to

higher redshifts ($z = 0.5, 1$, and 2), and Figs. A.12, A.13, and A.14 similarly extend Fig. 2.6 to higher redshifts. We show in Figs. A.15 and A.16 the scatter, median relations, and dispersions between halo specific mass accretion rate and concentration at different redshifts and masses. Finally, Figs. A.17 and A.18 explore the relationship between when halos reach their maximum mass loss since $M_{\rm peak}$ and when they had their last major merger, and Figs. A.19 and A.20 explore the relationship between when halos reach their maximum mass loss since $M_{\rm peak}$ and when they experienced their peak tidal force.

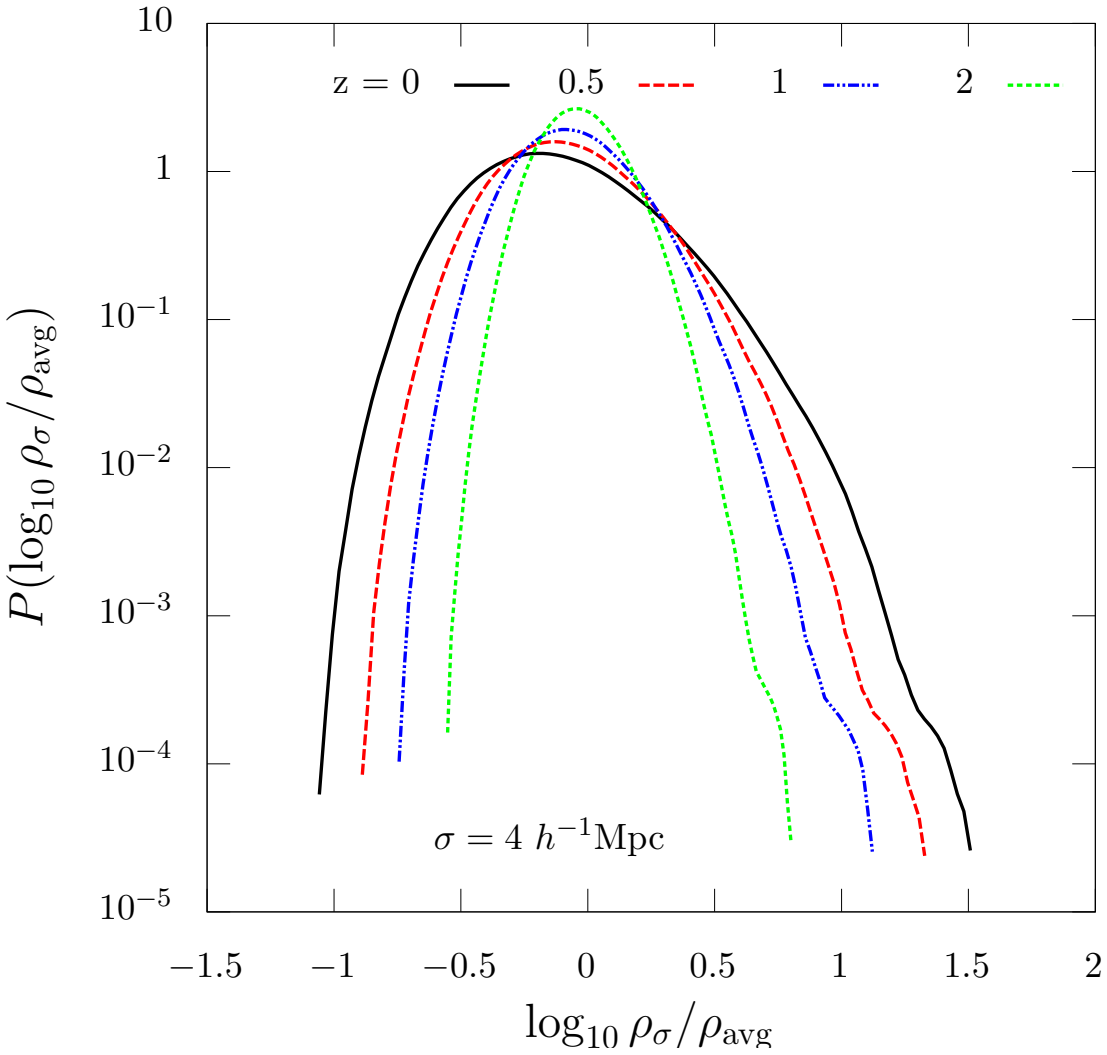

Figure A.1: Probability distributions of local environment density smoothed using $\sigma_s = 4\ h^{-1}$Mpc for the entire simulation volume, shown with log scaling on the vertical axis. Different coloured lines represent the same smoothing scale, but at different redshifts. Voids grow emptier with time, shifting the peak to lower densities. Non-linear structure grows as redshift decreases, but not as dramatically as on smaller scales (Fig. 2.3).

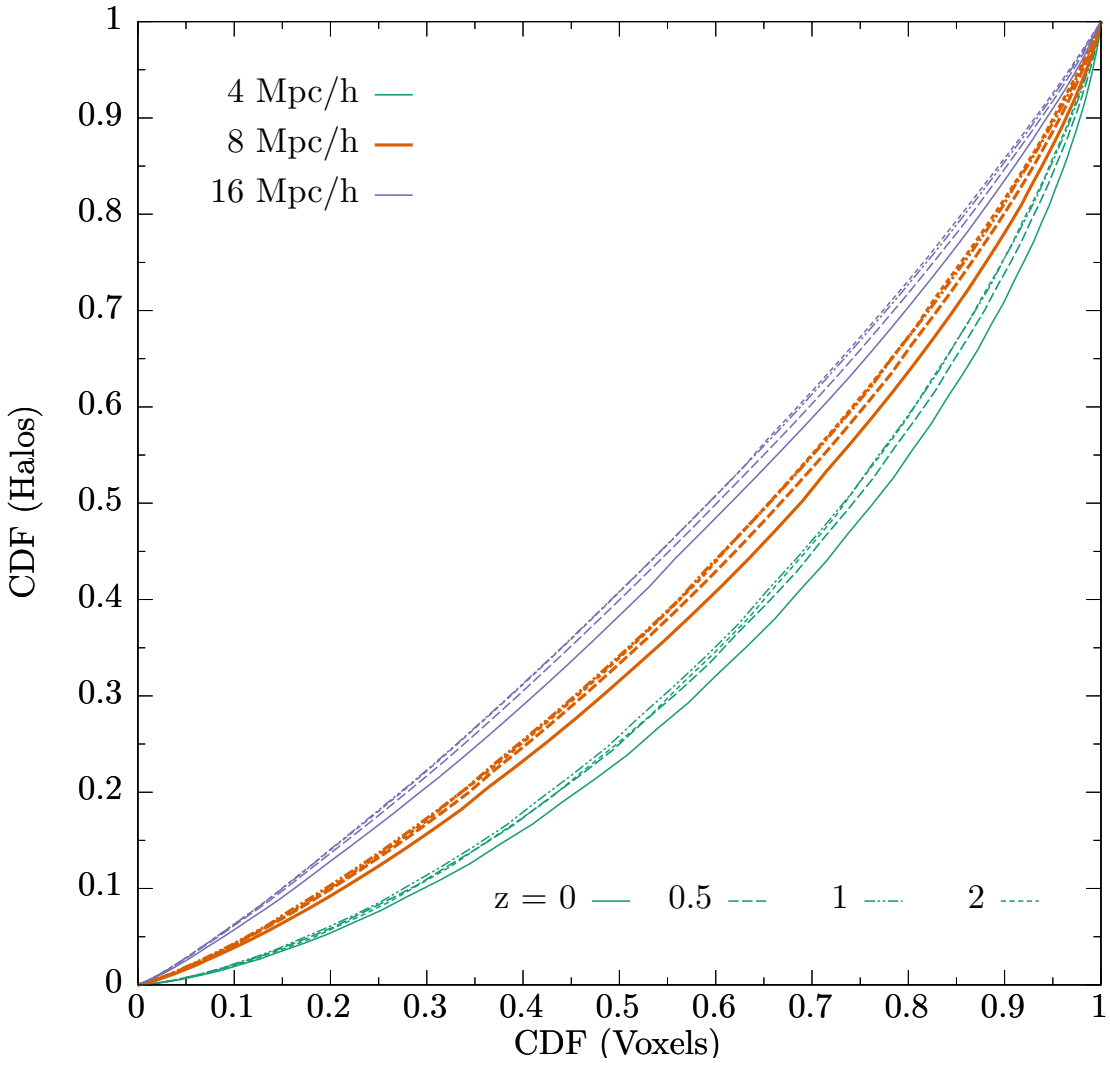

Figure A.2: Association between percentilized cosmic local densities and halo local densities, smoothed on scales $\sigma = 4$, 8, and 16 h^{-1}Mpc, and for redshifts 0, 0.5, 1, and 2. Cumulative distribution functions indicate how percentiles of density in the full simulation volume translate to percentiles of density around halos ($M_{\rm vir} > 10^{10}$ $M_\odot$). We see that the distributions of halo local densities and full volume densities are most similar at $z = 2$, and least similar at $z = 0$. Halos tend to accumulate in higher percentiles of full volume density at low redshift compared to at high redshift.

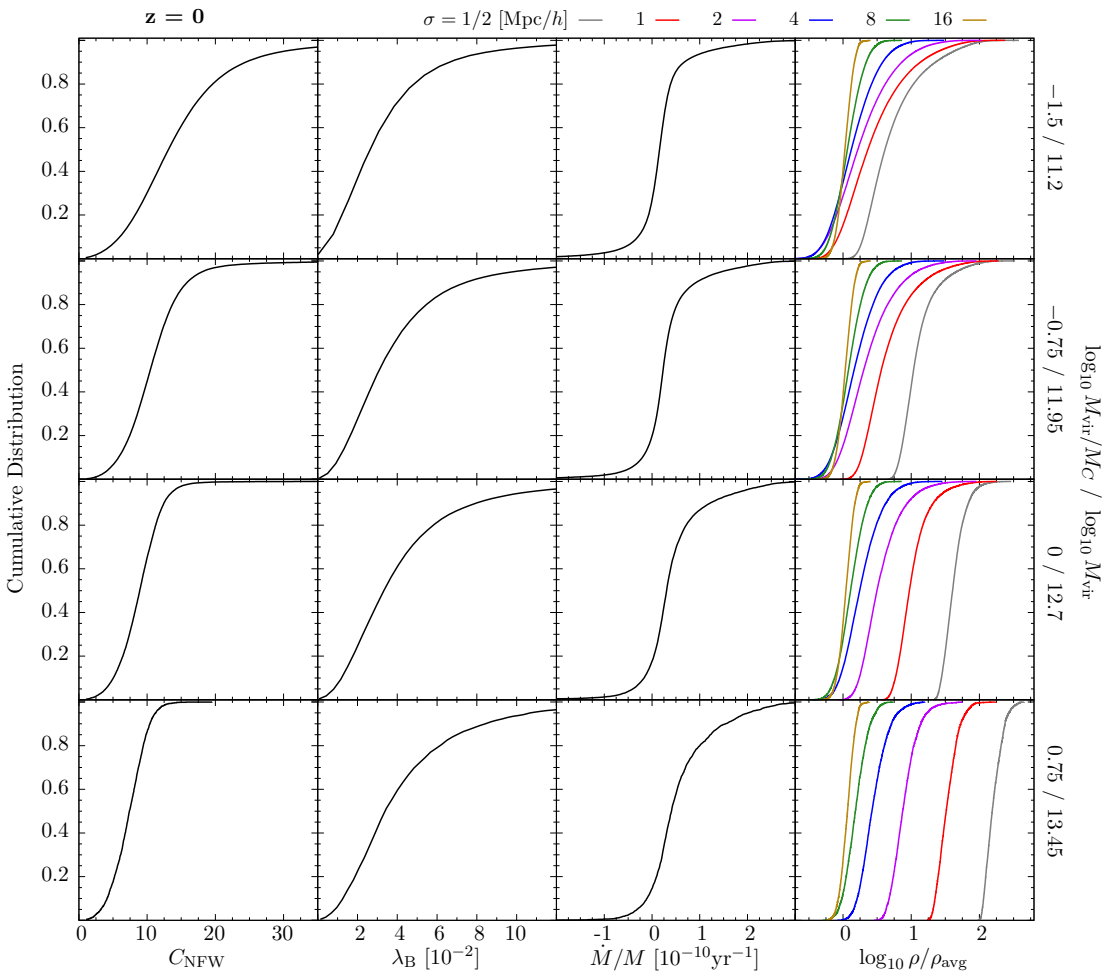

Figure A.3: Cumulative distribution functions of NFW concentration, spin parameter, specific accretion rate, and smoothed local density parameter, shown at z = 0 with the same mass bins as Fig. 2.6. Each row corresponds to an individual mass bin, with mass labels indicated on the right vertical axis. This figure relates the percentilized halo property–density correlation plot (Fig. 2.6) to the real valued halo property–density correlation plot (Fig. 2.5).

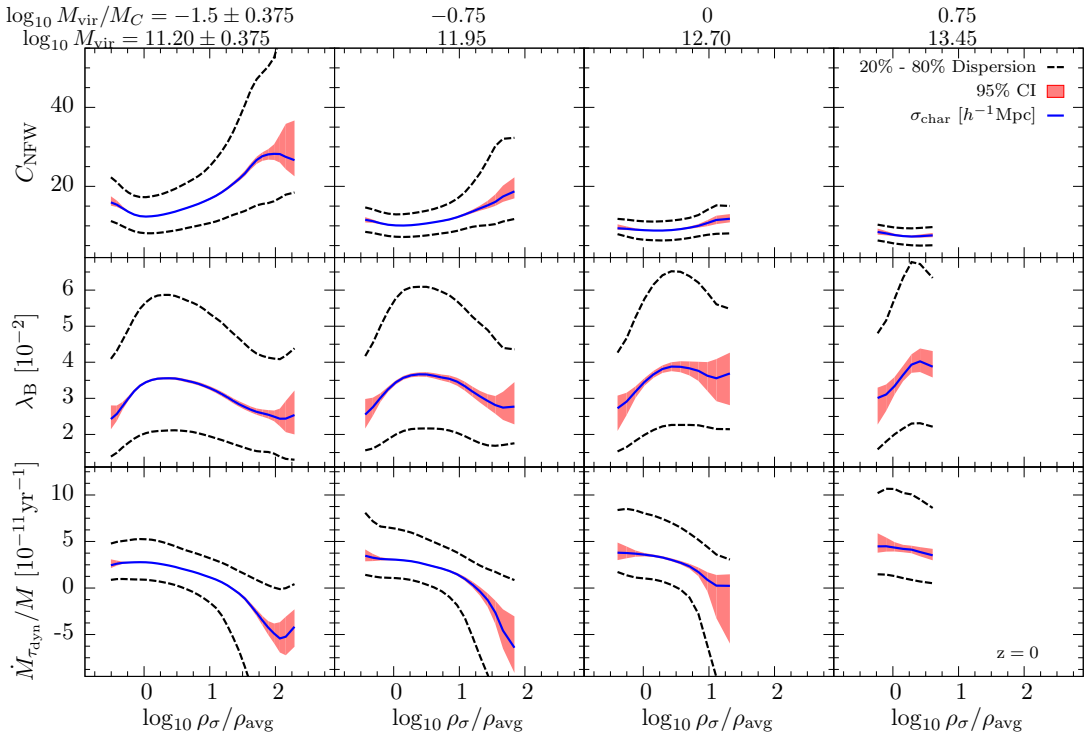

Figure A.4: Same as Fig. 2.6, but with dotted black lines showing 20-80 percentile range scatter in $C_{\rm NFW}$, $\lambda_{\rm B}$, and $\dot{M}/M$. The pink shaded area indicates the 95% confidence interval on the median. Only the 1/2 h^{-1}Mpc smoothed density parameter is shown. The scatter tends to be greater at high densities than low densities for $C_{\rm NFW}$ and accretion rate, but independent of density for spin parameter.

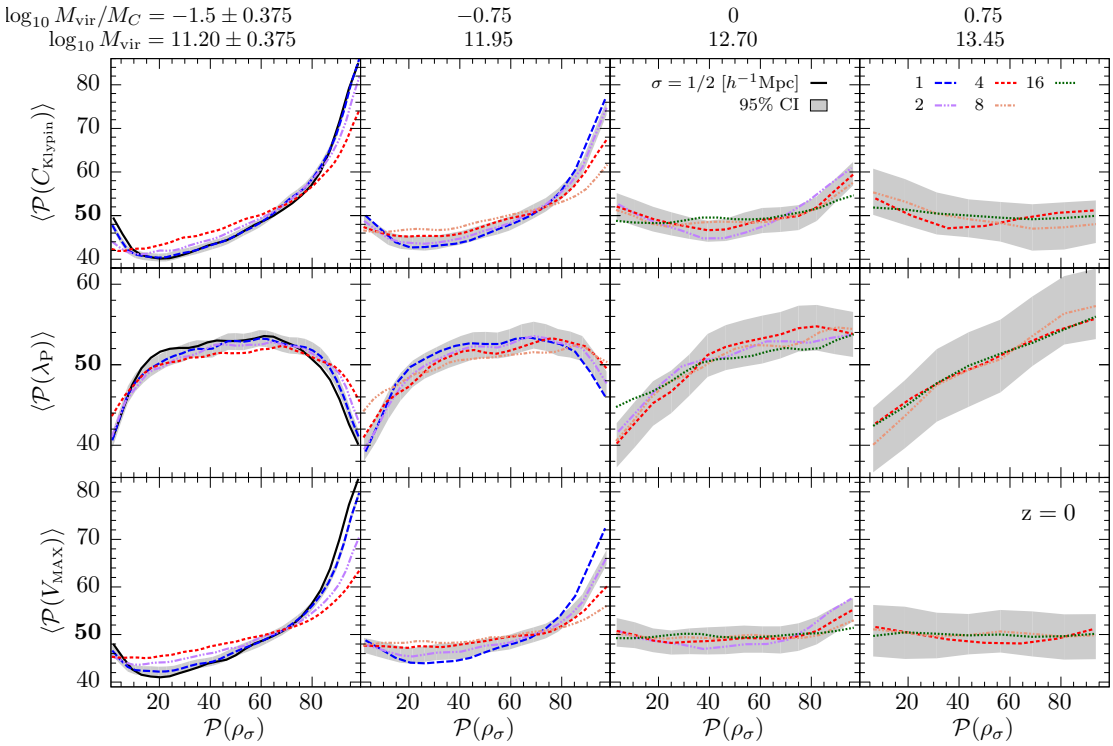

Figure A.5: Same as Fig. 2.6, but showing Klypin concentration ($C_{\rm Klypin}$), Peebles spin parameter ($\lambda_{\rm P}$), and maximum circular velocity ($V_{\rm max}$). The $C_{\rm Klypin} - \rho$ relation is very similar to the $C_{\rm NFW} - \rho$ relation, but with slightly less $C_{\rm Klypin}$ increase in high density regions. We also see a similar relation between $V_{\rm max}$ and local density: low mass halos in high density regions have much higher $V_{\rm max}$ than halos in lower density regions, with the reverse observed in very low density regions. $\lambda_{\rm P}$ is less reduced in high density regions and slightly more reduced in low density regions compared to $\lambda_{\rm B}$.

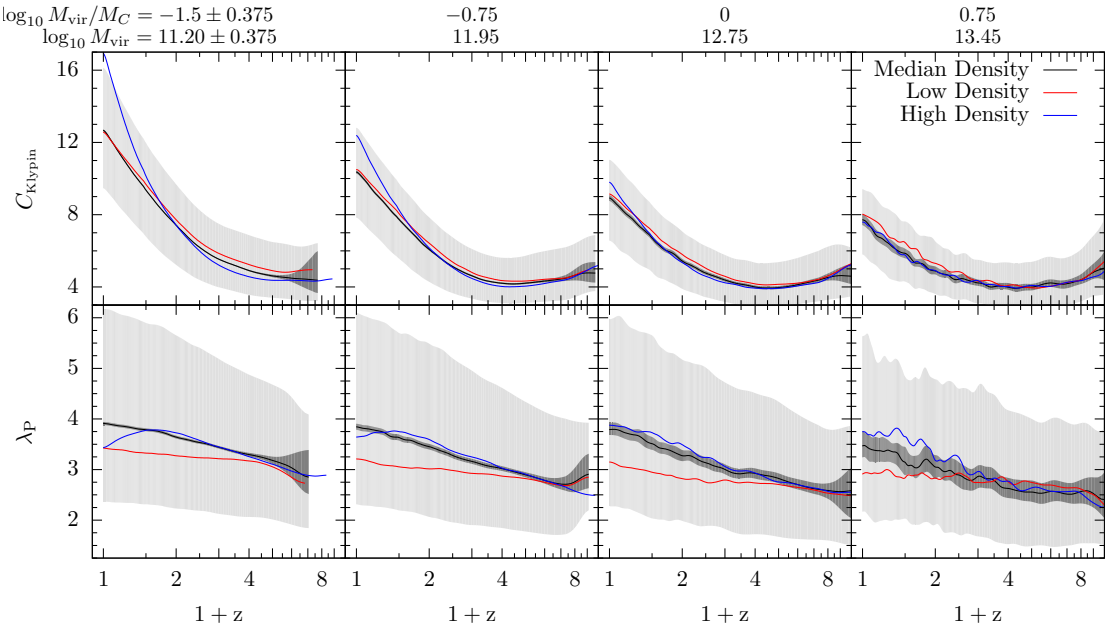

Figure A.6: Same as Fig. 2.7, but showing concentration determined using the Klypin method and Peebles' spin parameter. We observe similar trends as in 2.7 Rows 1 and 2, except that median $C_{\rm Klypin}$ values of low mass halos in high density regions are lower than $C_{\rm NFW}$, and λ evolution tends to increase with time (tendency towards positive slope rather than negative like $\lambda_{\rm B}$).

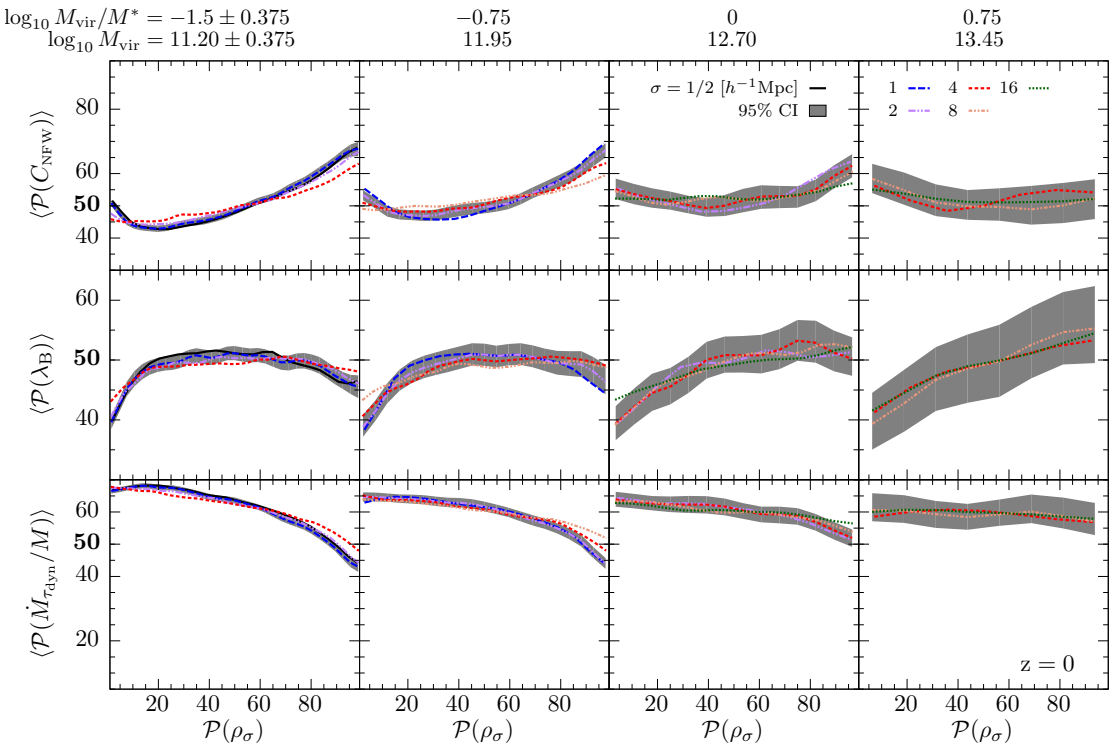

Figure A.7: Same as Fig. 2.6, but does not include halos that have lost more than 2% of their mass ($M_{\rm vir}/M_{\rm peak} < 0.98$). We determine medians using this sub-population, but we determine percentiles relative to all halos in the mass bin, allowing a fair comparison to Figs 2.6 and A.8. The correlations presented are only appreciably different for low mass halos in high density regions, where we see that concentrations are lower, spin parameters are higher, and accretion rates are higher compared to the all-halo correlations.

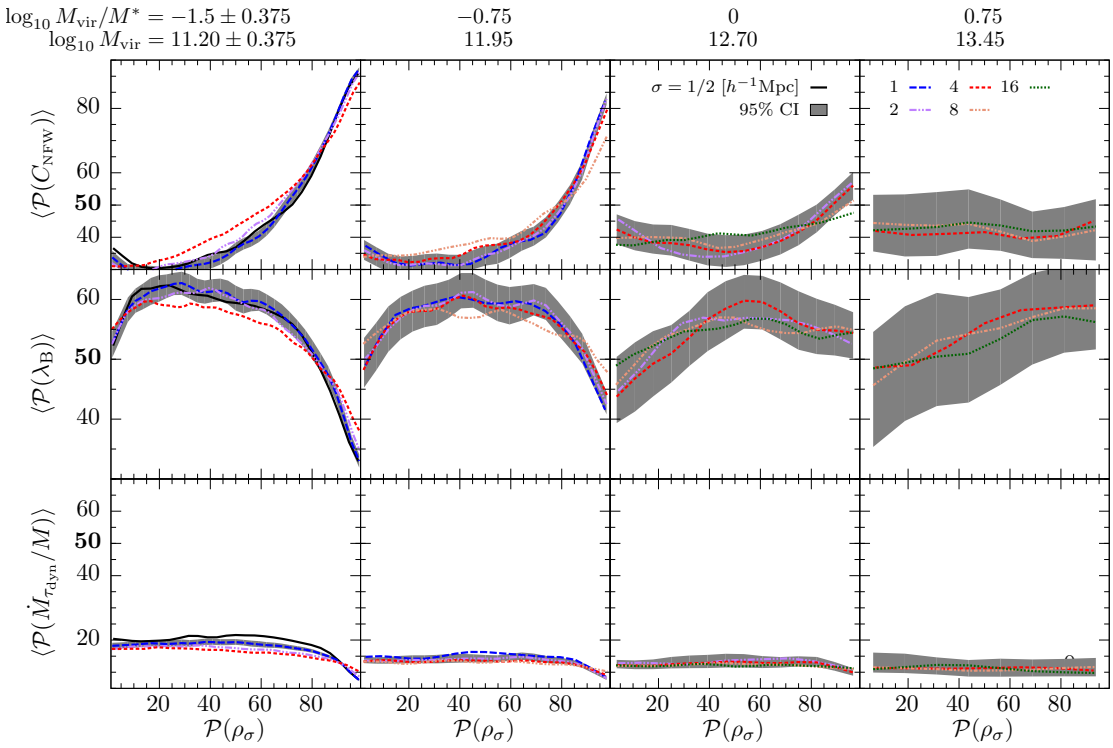

Figure A.8: Same as Fig. 2.6, but only includes halos that have lost more than 2% of their mass ($M_{\rm vir}/M_{\rm peak} < 0.98$). We determine medians using this subpopulation, but we determine percentiles relative to all halos in the mass bin, allowing a fair comparison to Figs 2.6 and A.7. We see that in high density regions, low mass stripped halos have high concentrations, low spin parameters, and very low accretion rates. In low density regions, low mass stripped halos also have low accretion rates, but lower concentrations, and higher spin parameters. Stripping has an opposite effect on concentration and spin parameter in high density regions compared to low density regions. Note that there are few stripped halos in low density regions compared to in high density regions.

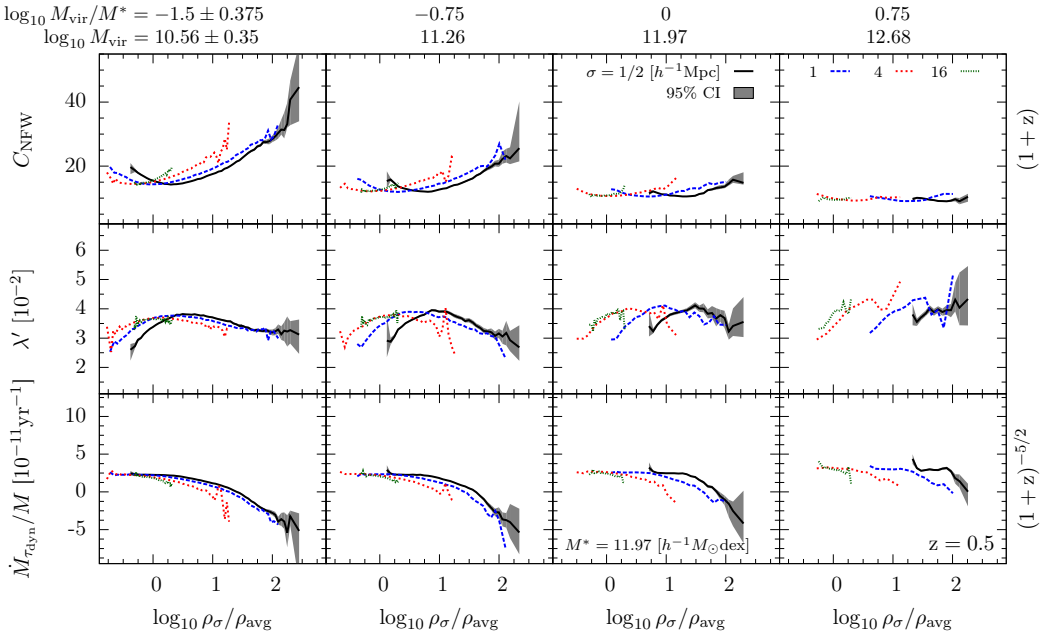

Figure A.9: Same as Fig. 2.5, but at redshift $z = 0.5$. We scale the specific mass accretion rate by $(1 + z)^{-\frac{5}{2}}$ and concentration by $(1 + z)$ to correct for global redshift evolution and allow for more straightforward comparison across redshifts. The mass bins are fixed in terms of $\log_{10} M_{\rm vir}/M^*$, where M^* is the characteristic mass for a given redshift (at $z = 0.5$, $M^* = 10^{11.97} h^{-1}{\rm M}_\odot$). Note that λ' refers to $\lambda_{\rm B}$.

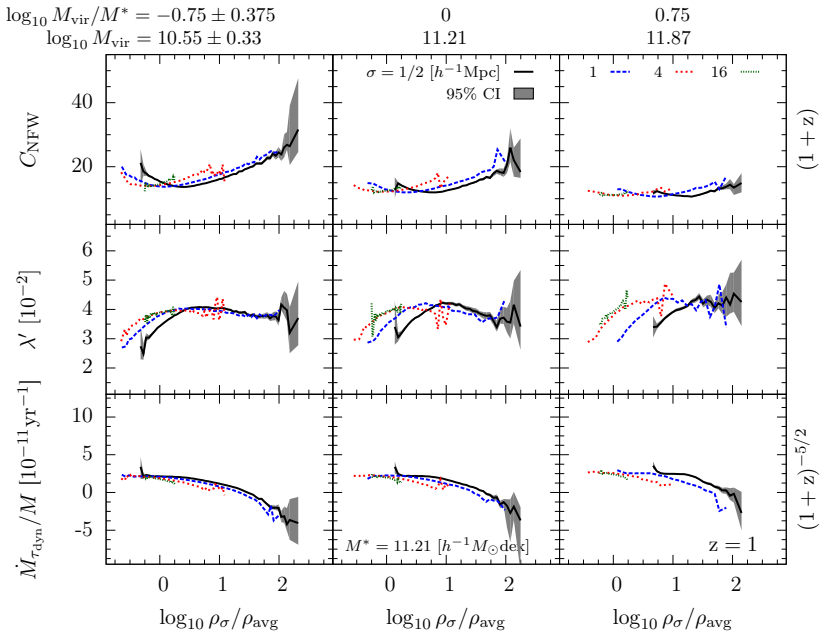

Figure A.10: Same as Fig. A.9, but at redshift $z = 1$.

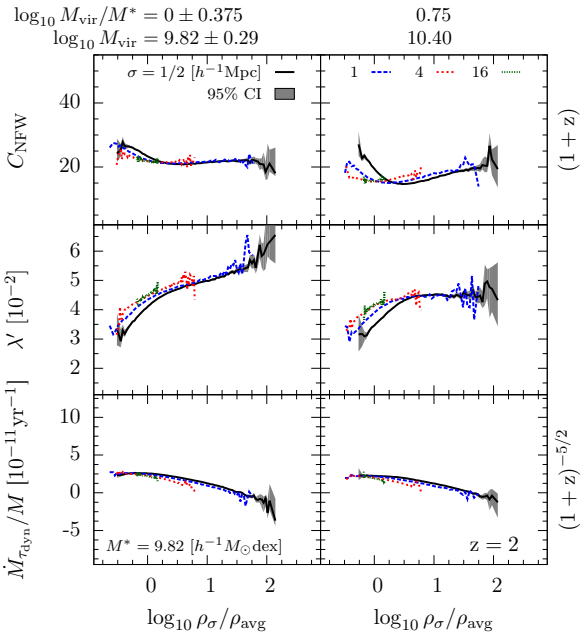

Figure A.11: Same as Fig. A.9, but at redshift $z = 2$.

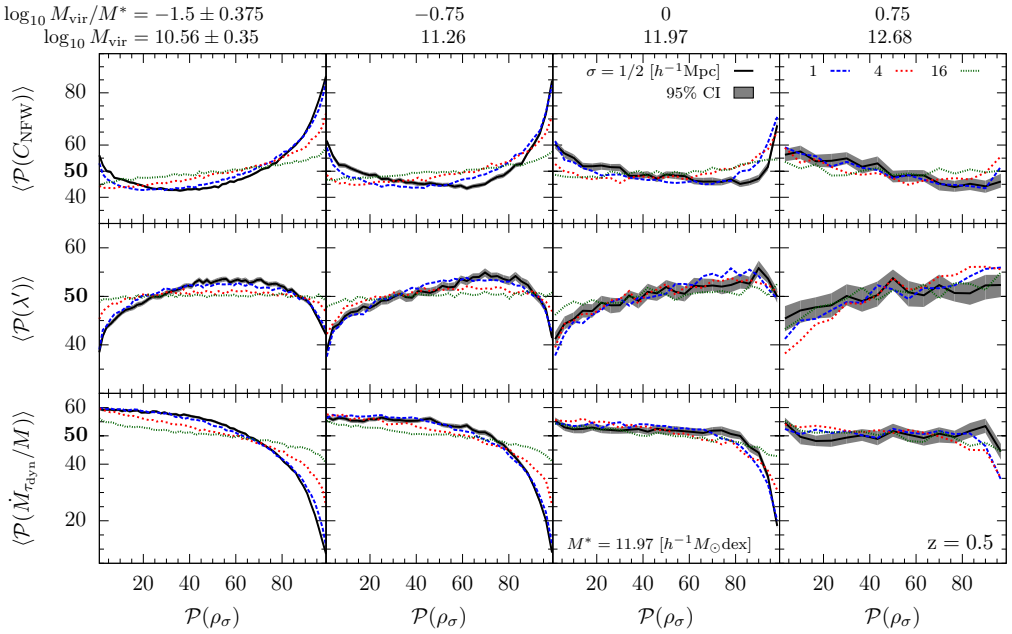

Figure A.12: Same as Fig. 2.6, but at redshift $z = 0.5$. The mass bins are fixed in terms of $\log_{10} M_{\rm vir}/M^*$, where M^* is the characteristic mass for a given redshift (at $z = 0.5$, $M^* = 10^{11.97} h^{-1}{\rm M}_\odot$). Note that λ' refers to $\lambda_{\rm B}$.

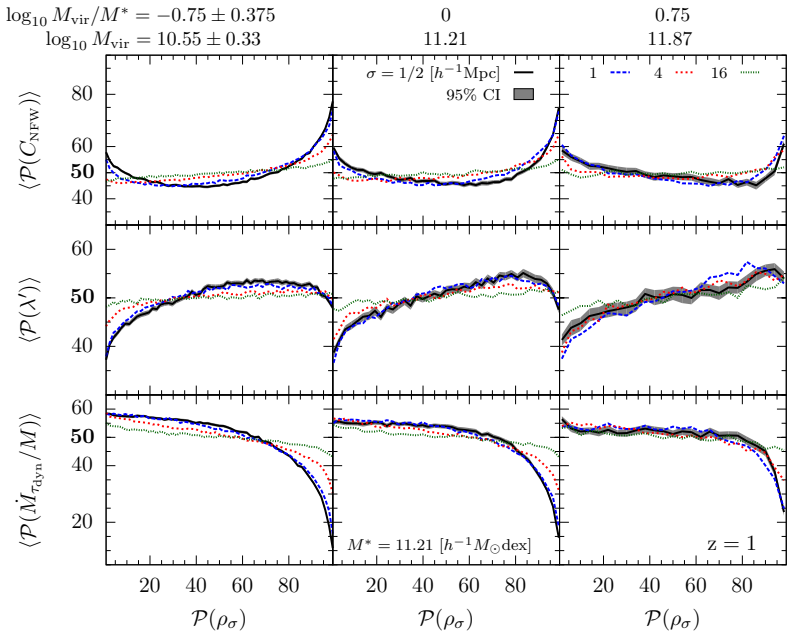

Figure A.13: Same as Fig. A.12, but at redshift $z = 1$.

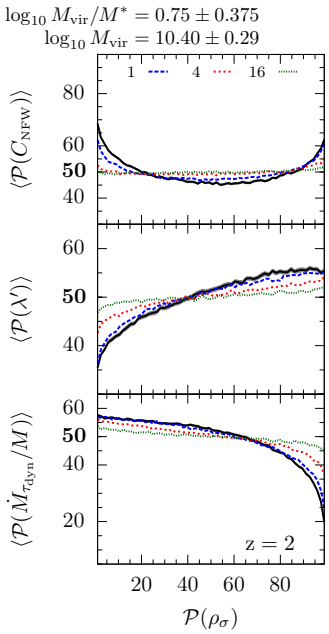

Figure A.14: Same as Fig. A.12, but at redshift $z = 2$.

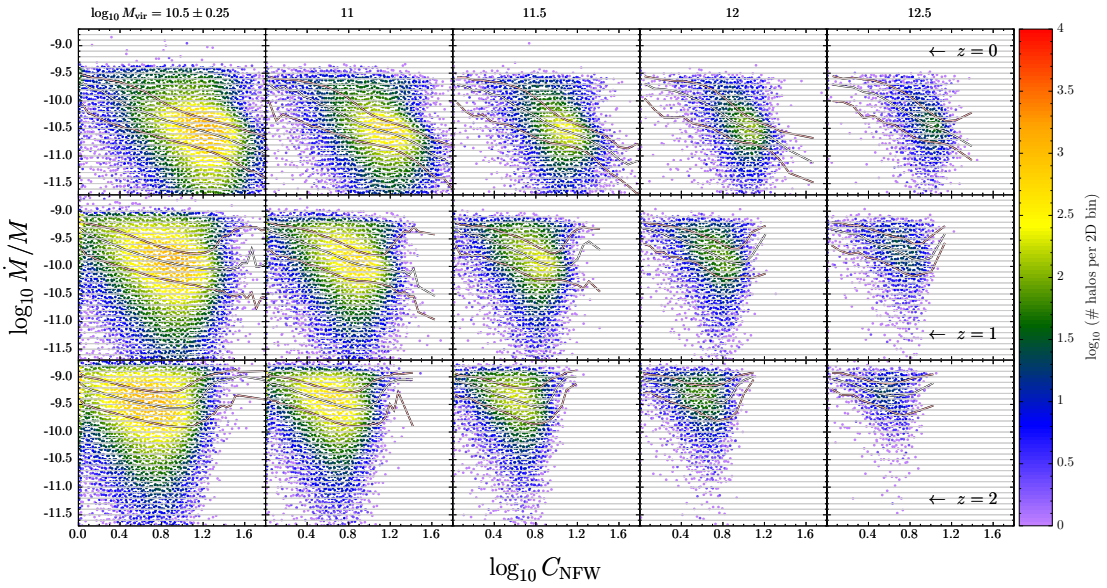

Figure A.15: In each panel, we plot the scatter between $\log_{10} C_{\rm NFW}$ and $\log_{10} \dot{M}/M$ for distinct halos at redshifts $z = 0$ (top row), $z = 1$ (middle row) and $z = 2$ (bottom row), where $\dot{M}$ is the dynamically time averaged mass accretion rate. The median and 20-80th percentile dispersion in the relations are overplotted as solid lines. The panels are divided into 5 mass bins, centered on $\log_{10} M_{\rm vir} = 10.5$, 11, 11.5, 12, and 12.5 $h^{-1}{\rm M}_{\odot}$ (± 0.25) from left to right, respectively. We color the scatter point density according to the colorbar on the right hand side of the figure. Orange regions indicate a scatter point density of > 1000 halos per cell; for cells that contain many halos, we (randomly) select only a few to plot to not overcrowd the figure. Note that because we are plotting the log of the specific mass accretion rate, this figure does not include halos with negative accretion rates. This means that the relations shown here are biased towards slightly higher accretion rates that would be expected for a complete halo sample, especially in regions of high environmental density where negative accretion rates are common. Overall, we see that higher accreting halos have lower NFW concentrations for all halos masses and at all redshifts.

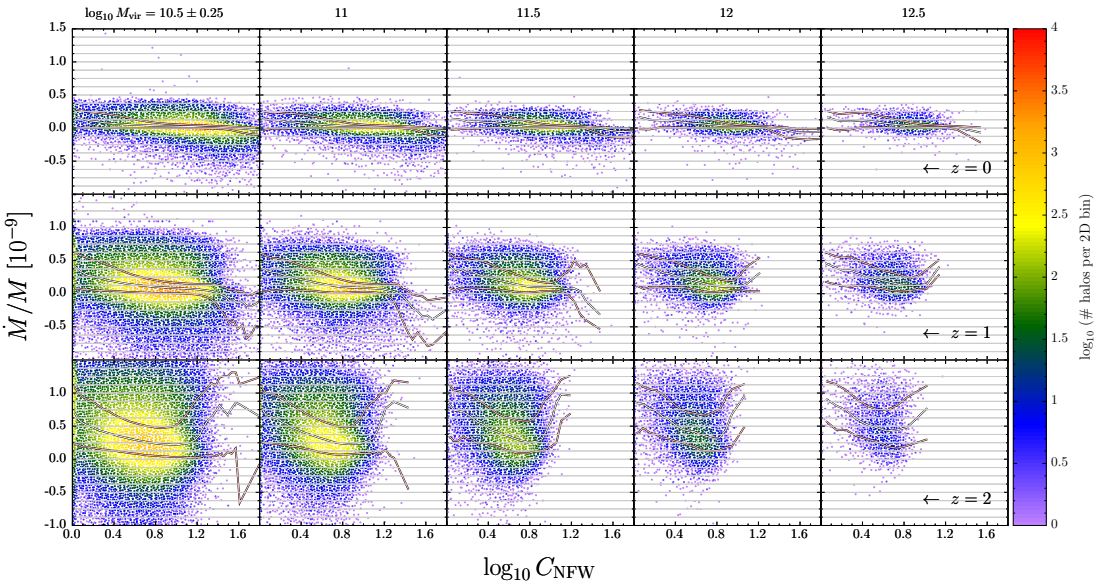

Figure A.16: Same as Fig. A.15, but using linear scaling for specific mass accretion rate. The dispersion in specific accretion rate is much higher at $z = 2$ than at $z = 0$. As a result of the figure scaling, the $z = 2$ relation is more readily interpreted. At $z = 1$ and $z = 2$, we see that halos with low concentrations have slightly higher accretion rates than halos with higher concentrations, though this effect flattens out at higher concentrations. The majority of halos with negative accretion rates have high concentrations at $z = 0$, but approximately median concentrations at $z = 1$ and $z = 2$.

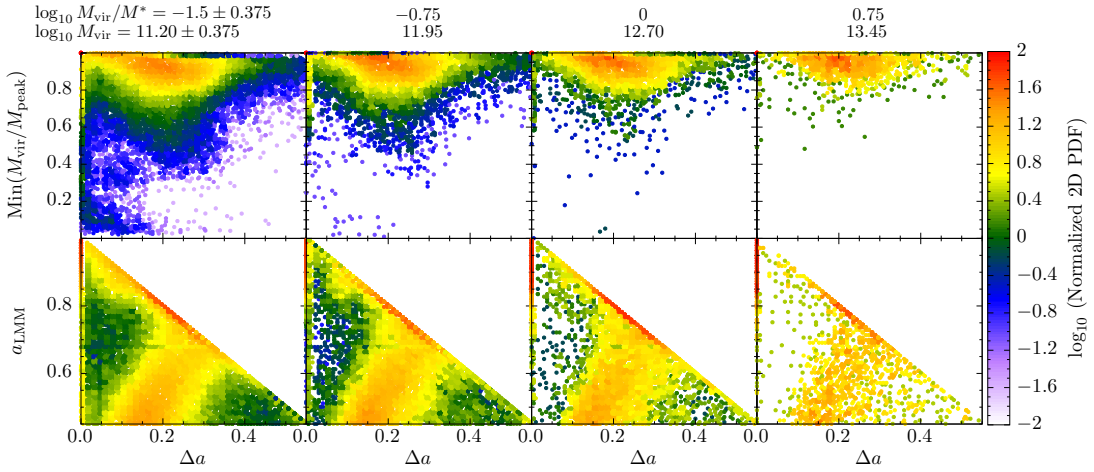

Figure A.17: This figure explains how much time elapses between major mergers and the subsequent mass loss phase that follows. On the top row, we plot the scale factor delay (time delay) between a major merger and the time of maximum mass loss ($\Delta a \equiv a_{\mathrm{Min}(M_{\rm vir}/M_{\rm peak})} - a_{\rm LMM}$) on the horizontal axis against the maximum mass loss fraction ($\mathrm{Min}(M_{\rm vir}/M_{\rm peak})$) on the vertical axis. The bottom row shows the maximum mass loss time delay (Δa) against the scale factor of the last major merger ($a_{\rm LMM}$). We color the scatter point density according to the colorbar on the right hand side of the figure. Orange regions indicate a scatter point density of > 100 halos per cell. The mass bins are determined using $z = 0$ halo masses, and are the same bins used throughout this work. From the bottom row, we see that halos whose last major merger was around $a = 0.5$ experienced maximum mass loss around $a = 0.65$ ($\Delta a = 0.15$), while halos whose last major merger was around $a = 0.7$ experienced maximum mass loss at around $z = 0$ ($\Delta a = 0.3$). From the top row, we see again that the maximum mass loss fraction peaks when Δa is approximately $0.15 - 0.3$ (depending on $a_{\rm LMM}$) and that most halos experience maximum mass loss in the range of $5 - 20\%$ of their peak mass. These trends are independent of halo mass.

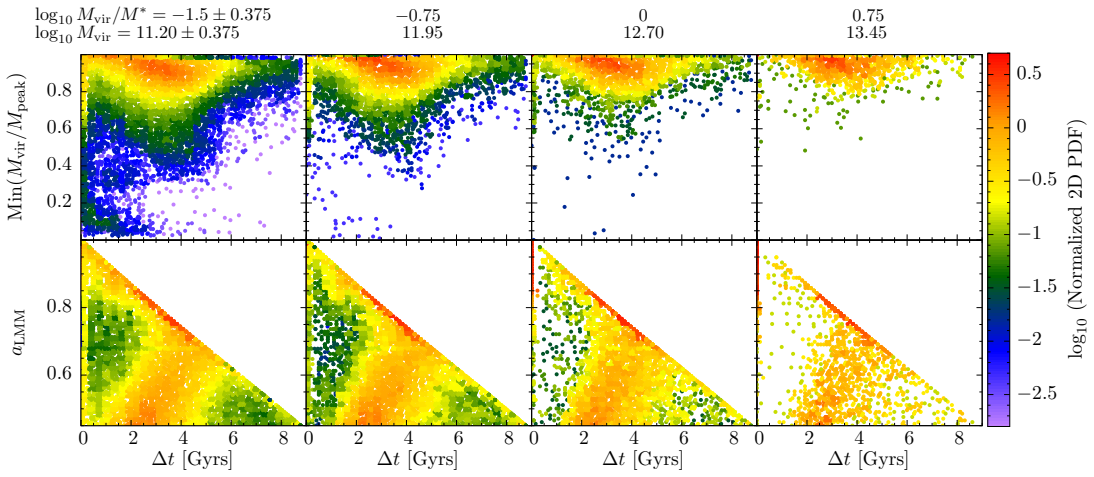

Figure A.18: Same as Fig. A.17, but with time delay Δt in units of Gyrs rather than scale factor.

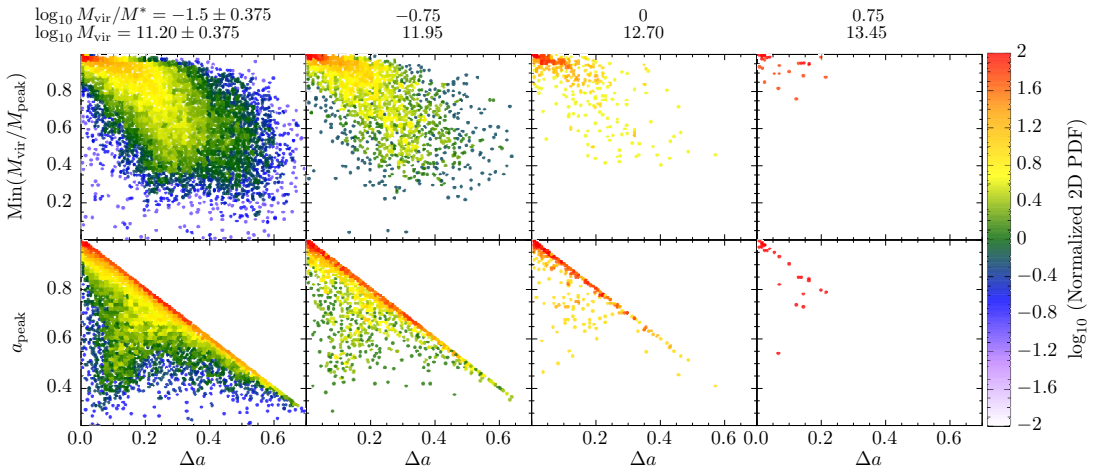

Figure A.19: Same as Fig. A.17 but for halos that recently experienced strong tidal forces (TF > 1) and did not have a recent major merger. This figure illustrates the relationship between tidal force history and the time of maximum mass loss for halos in high density regions. In this case, Δa represents the scale factor delay between when a halo experienced its peak tidal force ($a_{\rm peak}$) and when the halo had its maximum mass loss ($\Delta a \equiv a_{\mathrm{Min}(M_{\rm vir}/M_{\rm peak})} - a_{\rm peak}$). From the top row, we see that the most common scenario is halos that have just reached $\mathrm{TF}_{\rm peak}$ ($a_{\rm peak} = 1.0$) and have experienced no mass loss. Presumably, many of these halos will become subhalos in subsequent timesteps. We see that halos that experienced the longest delay between $a_{\rm peak}$ and the time of maximum mass loss also lost more mass on average. It is likely that these are cases where halos were previously subhalos one or more times but are distinct halos at $z = 0$. The bottom row shows that tidally stripped halos typically have reached their minimum mass at $z = 0$ (i.e., that $1.0 - a_{\rm peak} = \Delta a$). Halos seldom resume positive accretion following strong tidal forces.

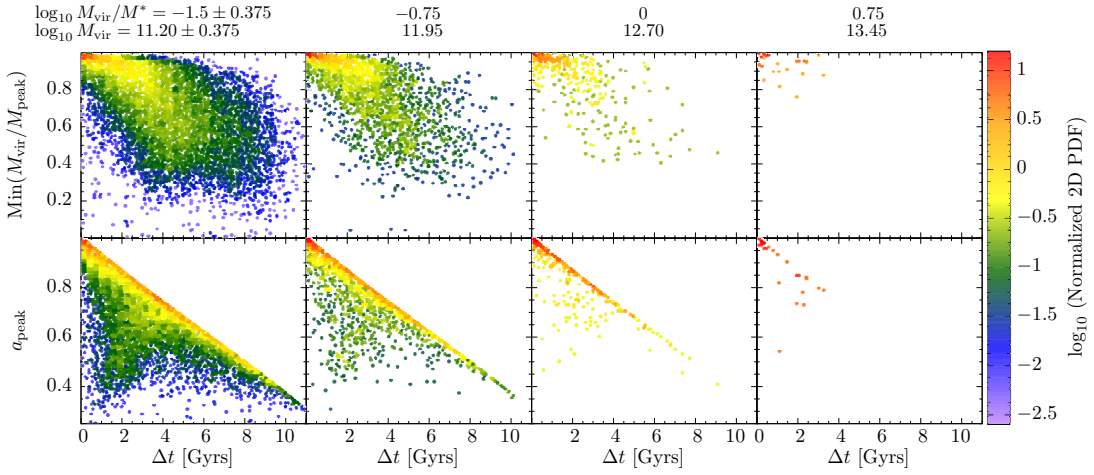

Figure A.20: Same as Fig. A.19, but with time delay Δt in units of Gyrs rather than scale factor.

Bibliography

Allgood B., Flores R. A., Primack J. R., Kravtsov A. V., Wechsler R. H., Faltenbacher A., Bullock J. S., 2006, MNRAS, 367, 1781

Aragon-Calvo M. A., 2016, MNRAS, 455, 438

Avila-Reese V., Colín P., Gottlöber S., Firmani C., Maulbetsch C., 2005, ApJ, 634, 51

Avila-Reese V., Firmani C., Klypin A., Kravtsov A. V., 1999, MNRAS, 310, 527

Bardeen J. M., Bond J. R., Kaiser N., Szalay A. S., 1986, ApJ, 304, 15

Behroozi P. et al., 2015, MNRAS, 454, 3020

Behroozi P. S., Loeb A., Wechsler R. H., 2013, JCAP, 6, 019

Behroozi P. S., Wechsler R. H., Lu Y., Hahn O., Busha M. T., Klypin A., Primack J. R., 2014, ApJ, 787, 156

Behroozi P. S., Wechsler R. H., Wu H.-Y., 2013, ApJ, 762, 109

Behroozi P. S., Wechsler R. H., Wu H.-Y., Busha M. T., Klypin A. A., Primack J. R., 2013a, ApJ, 763, 18

Behroozi P. S., Wechsler R. H., Wu H.-Y., Busha M. T., Klypin A. A., Primack J. R., 2013b, ApJ, 763, 18

Bett P., Eke V., Frenk C. S., Jenkins A., Helly J., Navarro J., 2007, MNRAS, 376, 215

Bett P., Eke V., Frenk C. S., Jenkins A., Okamoto T., 2010, MNRAS, 404, 1137

Blumenthal G. R., Faber S. M., Primack J. R., Rees M. J., 1984, Natur, 311, 517

Borzyszkowski M., Porciani C., Romano-Diaz E., Garaldi E., 2016, ArXiv e-prints

Bryan G. L., Norman M. L., 1998, ApJ, 495, 80

Bullock J. S., Dekel A., Kolatt T. S., Kravtsov A. V., Klypin A. A., Porciani C., Primack J. R., 2001, ApJ, 555, 240

Colombi S., Bernardeau F., Bouchet F. R., Hernquist L., 1997, MNRAS, 287, 241

Colombi S., Davis O., Devriendt J., Prunet S., Silk J., 2011, MNRAS, 414, 2436

Dalal N., White M., Bond J. R., Shirokov A., 2008, ApJ, 687, 12

Davis M., Efstathiou G., Frenk C. S., White S. D. M., 1985, ApJ, 292, 371

de Haan L., Ferreira A., 2006, Extreme Value Theory: An Introduction. Springer

Dekel A., Zolotov A., Tweed D., Cacciato M., Ceverino D., Primack J. R., 2013, MNRAS, 435, 999

Desjacques V., Sheth R. K., 2010, PhysRevD, 81, 023526

Despali G., Giocoli C., Bonamigo M., Limousin M., Tormen G., 2016, ArXiv e-prints

Despali G., Giocoli C., Tormen G., 2014, MNRAS, 443, 3208

D'Onghia E., Navarro J. F., 2007, MNRAS, 380, L58

Fakhouri O., Ma C.-P., 2010, MNRAS, 401, 2245

Faltenbacher A., White S. D. M., 2010, ApJ, 708, 469

Frenk C. S., White S. D. M., 2012, Annalen der Physik, 524, 507

Gao L., Springel V., White S. D. M., 2005, MNRAS, 363, L66

Gao L., White S. D. M., 2007, MNRAS, 377, L5

Goh T. et al., 2019, MNRAS, 483, 2101

Gottlöber S., Klypin A., Kravtsov A. V., 2001, ApJ, 546, 223

Haas M. R., Schaye J., Jeeson-Daniel A., 2012, MNRAS, 419, 2133

Hahn O., Carollo C. M., Porciani C., Dekel A., 2007a, MNRAS, 381, 41

Hahn O., Porciani C., Carollo C. M., Dekel A., 2007b, MNRAS, 375, 489

Hahn O., Porciani C., Dekel A., Carollo C. M., 2009a, MNRAS, 398, 1742

Hahn O., Porciani C., Dekel A., Carollo C. M., 2009b, MNRAS, 398, 1742

Hearin A. P., Behroozi P. S., van den Bosch F. C., 2016, MNRAS, 461, 2135

Hearin A. P., Watson D. F., van den Bosch F. C., 2015, MNRAS, 452, 1958

Jeeson-Daniel A., Dalla Vecchia C., Haas M. R., Schaye J., 2011, MNRAS, 415, L69

Jiang F. et al., 2018, arXiv e-prints

Kaiser N., 1984, ApJ, 284, L9

Klypin A., Yepes G., Gottlöber S., Prada F., Heß S., 2016a, MNRAS, 457, 4340

Klypin A., Yepes G., Gottlöber S., Prada F., Heß S., 2016b, MNRAS, 457, 4340

Klypin A. A., Trujillo-Gomez S., Primack J., 2011, ApJ, 740, 102

Kotz S., Nadarajah S., 2000, Extreme Value Distributions: Theory and Applications. Imperial College Press

Kravtsov A. V., 2013, ApJ, 764, L31

Lee C. T., Primack J. R., Behroozi P., Rodríguez-Puebla A., Hellinger D., Dekel A., 2017, MNRAS, 466, 3834

Lee C. T., Primack J. R., Behroozi P., Rodríguez-Puebla A., Hellinger D., Dekel A., 2018, MNRAS, 481, 4038

Lemson G., Kauffmann G., 1999, MNRAS, 302, 111

Ludlow A. D. et al., 2013, MNRAS, 432, 1103

Ludlow A. D., Navarro J. F., Li M., Angulo R. E., Boylan-Kolchin M., Bett P. E., 2012a, MNRAS, 427, 1322

Ludlow A. D., Navarro J. F., Li M., Angulo R. E., Boylan-Kolchin M., Bett P. E., 2012b, MNRAS, 427, 1322

Ludlow A. D., Porciani C., 2011, MNRAS, 413, 1961

Macciò A. V., Dutton A. A., van den Bosch F. C., Moore B., Potter D., Stadel J., 2007, MNRAS, 378, 55

Maulbetsch C., Avila-Reese V., Colín P., Gottlöber S., Khalatyan A., Steinmetz M., 2007, ApJ, 654, 53

McNaught-Roberts T. et al., 2014, MNRAS, 445, 2125

Mo H. J., White S. D. M., 1996, MNRAS, 282, 347

More S., Diemer B., Kravtsov A. V., 2015, ApJ, 810, 36

Muldrew S. I. et al., 2012, MNRAS, 419, 2670

Navarro J. F., Frenk C. S., White S. D. M., 1996, ApJ, 462, 563

Paranjape A., Hahn O., Sheth R. K., 2018, MNRAS, 476, 3631

Peacock J. A., Heavens A. F., 1985, MNRAS, 217, 805

Peebles P. J. E., 1969a, ApJ, 155, 393

Peebles P. J. E., 1969b, ApJ, 155, 393

Planck Collaboration et al., 2014a, A&A, 571, A16

Planck Collaboration et al., 2014b, A&A, 571, A16

Planck Collaboration et al., 2015, ArXiv e-prints

Planck Collaboration et al., 2016, A&A, 594, A13

Porciani C., Dekel A., Hoffman Y., 2002, MNRAS, 332, 325

Primack J. R., 2012, Annalen der Physik, 524, 535

Rodriguez-Puebla A., Behroozi P., Primack J., Klypin A., Lee C., Hellinger D., 2016, ArXiv e-prints

Rodríguez-Puebla A., Behroozi P., Primack J., Klypin A., Lee C., Hellinger D., 2016, MNRAS, 462, 893

Rodríguez-Puebla A., Primack J. R., Avila-Reese V., Faber S. M., 2017, MNRAS, 470, 651

Sheth R. K., 1998, MNRAS, 300, 1057

Sheth R. K., Tormen G., 2004, MNRAS, 350, 1385

Skibba R. A., Macciò A. V., 2011, MNRAS, 416, 2388

Somerville R. S. et al., 2018, MNRAS, 473, 2714

Springel V. et al., 2005, Natur, 435, 629

Sutter P. M., Lavaux G., Wandelt B. D., Weinberg D. H., 2012, ApJ, 761, 44

Tuan A., 2016, Studying the Dependence of Dark Matter Halo Density Distribution on Environment. `http://physics.ucsc.edu/~joel/AustinTuan-SiemensPaper-26Sept2016-Studying%20the%20Dependence%20of%20Dark%20Matter%20Halo%20Density%20Profiles%20on%20Environment.pdf`, [Online; accessed 12-March-2019]

Tuan A., Zhu J., 2015, Understanding the Formation and Evolution of Stripped Dark Matter Halos. http://physics.ucsc.edu/~joel/AustinTuan&JessicaZhu-SiemensPaper-22Sept2015.pdf, [Online; accessed 12-March-2019]

Valageas P., Munshi D., 2004, MNRAS, 354, 1146

van den Bosch F. C., 2017, MNRAS, 468, 885

Vera-Ciro C. A., Sales L. V., Helmi A., Frenk C. S., Navarro J. F., Springel V., Vogelsberger M., White S. D. M., 2011, MNRAS, 416, 1377

Vitvitska M., Klypin A. A., Kravtsov A. V., Wechsler R. H., Primack J. R., Bullock J. S., 2002, ApJ, 581, 799

Wang H., Mo H. J., Jing Y. P., Yang X., Wang Y., 2011a, MNRAS, 413, 1973

Wang H., Mo H. J., Jing Y. P., Yang X., Wang Y., 2011b, MNRAS, 413, 1973

Wang H. Y., Mo H. J., Jing Y. P., 2007, MNRAS, 375, 633

Wechsler R. H., Bullock J. S., Primack J. R., Kravtsov A. V., Dekel A., 2002a, ApJ, 568, 52

Wechsler R. H., Bullock J. S., Primack J. R., Kravtsov A. V., Dekel A., 2002b, ApJ, 568, 52

Wechsler R. H., Zentner A. R., Bullock J. S., Kravtsov A. V., Allgood B., 2006, ApJ, 652, 71

White S. D. M., 1984, ApJ, 286, 38

Wong A. W. C., Taylor J. E., 2012, ApJ, 757, 102

Wu P., Zhang S., 2017, ArXiv e-prints